

POLITECNICO DI TORINO

Master's degree in Mechatronic Engineering



Master's Thesis

Development of prognostic algorithm for electro-hydraulic flight controls

Supervisors

Prof. Paolo Maggiore

Ing. Matteo Davide Lorenzo Dalla Vedova

Ing. Pier Carlo Berri

Candidate

Simone Santaera

April 2021

SUMMARY

1	Overview.....	6
2	Servo mechanism for flight control	8
2.1	Hydro-mechanical actuators	9
2.2	Electro-mechanical actuators (EMA)	10
2.3	Electro-hydrostatic actuators (EHA).....	11
3	Servo-valve for position command.....	13
3.1	Flapper-nozzle valve.....	13
3.2	Technical characteristics of valves and non-linearities.....	16
3.2.1	Lapp Condition	18
3.2.2	Threshold	19
3.2.3	Magnetic hysteresis.....	19
3.2.4	Friction.....	21
3.2.5	Backlash.....	26
3.2.6	Offset valve.....	26
4	Simulink model.....	28
4.1	Reference model	29
4.1.1	Hysteresis, offset and interferences in the torque motor.....	31
4.1.2	Electro mechanical model of the servovalve	33
4.1.3	Fluid dynamic model	39
4.1.4	Mechanical model of the jack	48
4.2	Monitoring model	49
5	Development of monitoring fluid-dynamic model	52
5.1	Simple linearized fluid-dynamic model.....	52
5.2	Second linearized model.....	54
5.3	Developed fluid-dynamic model.....	58
6	Fault analysis	68
6.1	Demagnetization of the torque motor	68
6.1.1	Response to a step input signal	68
6.1.2	Response to a ramp input signal	72
6.1.3	Response to a sine input signal	75
6.1.4	Prognostic parameter for <i>KGM</i> failure.....	78
6.2	Increasing static friction on the jack	78

6.2.1	Response to a step input signal	78
6.2.2	Response to a ramp input signal	82
6.2.3	Response to a sine input signal	85
6.2.4	Prognostic parameter for <i>KGM</i> failure.....	88
6.3	Fault combination analysis	88
7	Optimization algorithms	92
7.1	Genetic algorithm	93
7.2	Prognostic analysis through genetic algorithm.....	97
8	Conclusions and future works.....	114

1 OVERVIEW

The aim of this thesis is to develop an efficient fluid-dynamic model of an electro-hydrostatic actuator (EHA). Successively, in the second part, the system will be subjected to two different faults (demagnetization of the torque motor, increment of the static friction on the jack) and it will develop an algorithm that can autonomously detect these failures and predict the remaining useful life of the components.

This is what is called Prognostic and Health Management (PHM). Nowadays, with the increasing complexity of the aircraft, this discipline is becoming important and important: companies, in fact, can be more competitive using the components for all the useful life, until the component will not perform its function anymore.

In this way, scheduling of maintenances can be optimized without compromising the reliability of the components. With the model-based approach, used in the models of this thesis, it is possible to identify location, entity and mode of each failure; in particular, two different models of the same system have been used: the first one, more complicated and more reliable, has been used as reference for the second one, approximated respect to the previous one and less demanding in terms of computational effort, used for the prognostic purpose.

The first step of this thesis has been the development of the fluid-dynamic model of the approximated one: reproduction of the characteristic curves of the servovalve was not sufficient to have the same behaviour in both models, since the first one has a time-dependant response; for this reason, the model has been completed with the same time constant implementation.

After the validation of the new fluid-dynamic model, the successive step has been the identification of parameters that can clearly show the presence of each fault. In both models, in fact, constants of damage are present, within the range from 0 to 1, where 0 corresponds to nominal condition and 1 to totally compromised component (for the increasing friction on the jack only the value of the static friction has been changed). In the studied cases, the physical quantities used for the identification are the current absorbed by torque motor and the differential pressure across the chamber of the jack.

Finally, these quantities have been used for the prognostic algorithm: the first model, more precise, have been used as a reference for the optimization algorithm that minimizes the objective function, calculated from these quantities, making the response of the simplified model match the first. The algorithm, through iterations, simulate different entities of faults, until the reference is matched: once its task has been completed, it returns the constants of damage and can esteem the state of health of the system.

2 SERVO MECHANISM FOR FLIGHT CONTROL

Movable command surfaces are necessary to grant the pilot in the cockpit to control and manoeuvre the aircraft: changing the external shape of wing surfaces, aerodynamic resultant forces and moments on the aircraft are modified.

There are two different types of flight commands: primary and secondary.

Primary commands are actuated continuously during the flight and they must have three fundamental characteristics: they must be instinctive, the aircraft must move on the same direction of the commands, proportional and reversible, so that a movement of the control bar corresponds to a precise deflection of the mobile surfaces and vice versa and finally sensitive, the pilot must have the sensation of resistance and stress of the mobile surfaces, as function of amplitude of the deflection and velocity of the aircraft. They comprehend ailerons, rudder and elevators.

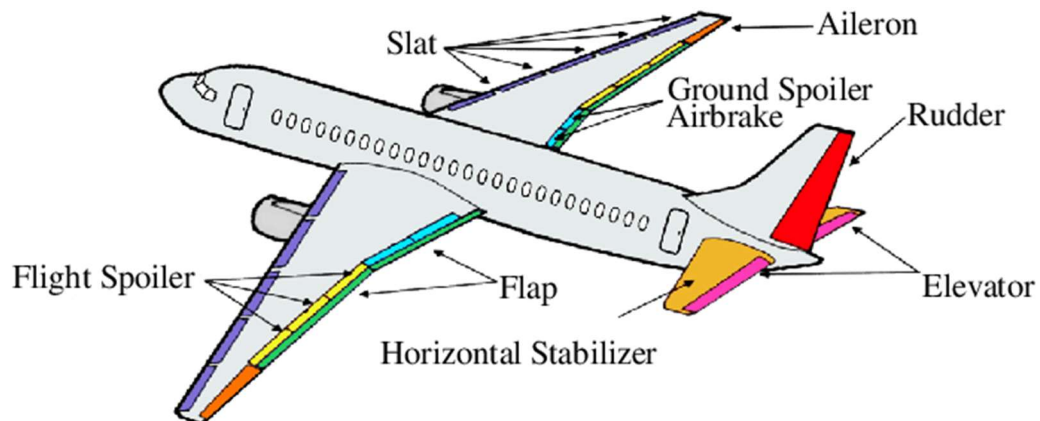


Figure 2.1: Primary and secondary flight commands.

On the other hand, leading edge extensions (slats), trailing edge extensions (flaps), tail plane and air brakes (spoilers) are considered secondary commands.

Secondary commands, in contrast to the primary ones, have a discrete positioning and are modified by the pilot only during certain flight phases, such as in the rolling phase, take-off or landing. Moreover, they must be irreversible and, for their limited use, have lower performances both in terms of magnitude and accuracy of actuation.

The actuation system that permits to deflect the mobile surfaces is called *flight control actuation system*: in a great part of common commercial aircrafts, it is implemented with hydraulic actuators, thanks to their robustness, security and reliability. They are commanded by the computer that translates the analogical signal coming from the pilot to a digital one. However, these actuators have some disadvantages, as the high weight and complexity: because of this, localization and maintenance of a possible fault in the system is very difficult.

With the increasing complexity of modern systems, it is more and more difficult to reduce weight of components due to the necessary redundancies to satisfy the safety requirements.

A possible solution is the use of servo electro-hydrostatic actuators (EHA): in these mechanisms, there is a great compaction of the components with a hydraulic circuit with lower dimensions respect to a centralized one. They convert electric energy into hydraulic one thanks to a fixed displacement pump actuated from an electric motor, a servo-valve and a hydraulic actuator. Not needing a hydraulic supply permits to save space and weight.

Nowadays, another solution has been developed, the electro-mechanical actuators (EMA) that are rising and competing with the previous ones in terms of reliability and robustness.

In the following paragraphs, the main characteristics of traditional hydro-mechanical actuators, EHA and EMA will be examined.

2.1 HYDRO-MECHANICAL ACTUATORS

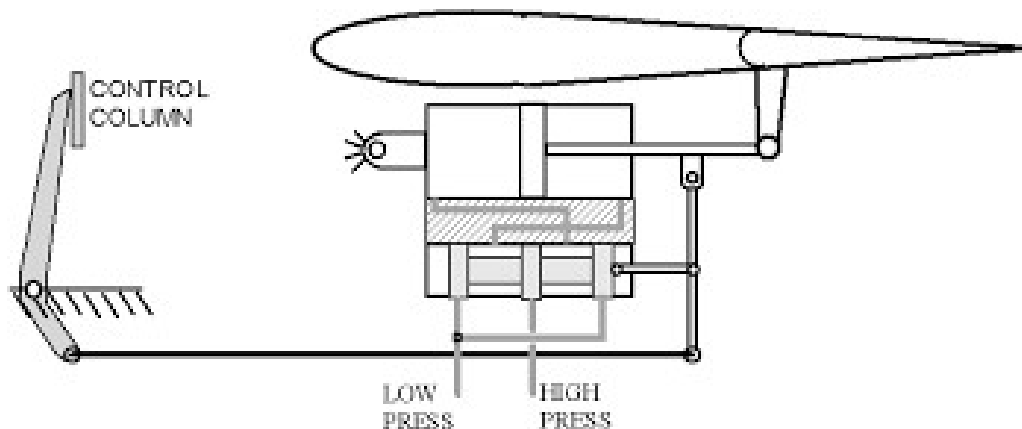


Figure 2.2: Hydro-mechanical actuator scheme.

Hydro-mechanical actuators were the most used actuation system. They are composed of the control element, amplification of the command (valve) and the actuator.

The pilot's input is transmitted to the valve by means of a cinematic chain, connected to a three-centres lever: one lever is fixed to the spool of the valve and permits it to move, while the second one is connected to the control surface and represents the mechanical feedback. In this way, the valve is commanded with the geometrical difference between commanded position and surface position, to reach a stable displacement. The valve, once commanded, supply one chamber of the actuator and discharge the other.

2.2 ELECTRO-MECHANICAL ACTUATORS (EMA)

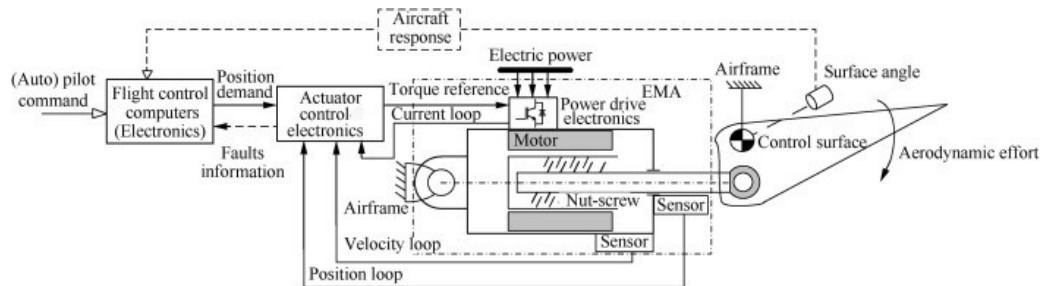


Figure 2.3: Electro-mechanical actuator control scheme (Maré & Fu, 2017, p. 49).

EMA transforms electrical power into mechanical one: it is composed of an electrical motor, a gear box, to reduce RPM and increasing the torque available and a cinematic chain to convert the rotatory movement into a linear one (usually a ball screw to reduce friction).

This is an example of all-electric system and probably will take place on all the aircrafts in the future; however, there is still a great problem with this kind of actuation: if a single grip occurs in the ball screw, all the system can not move anymore, and the control surface remains blocked. This is the main reason why EMA are used now only for secondary commands.

2.3 ELECTRO-HYDROSTATIC ACTUATORS (EHA)

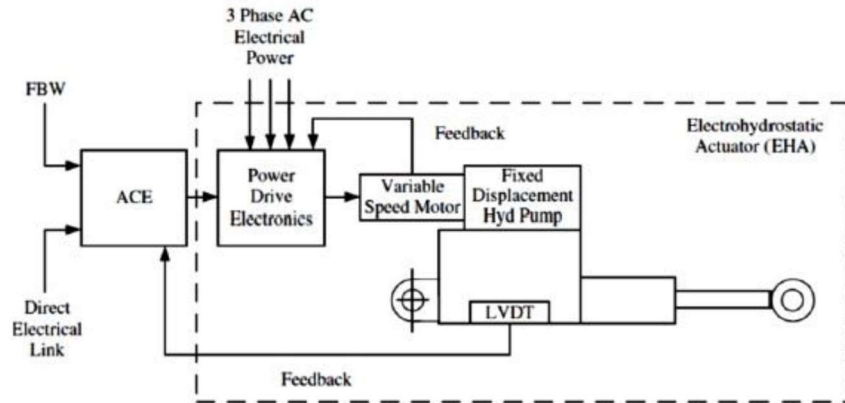


Figure 2.4: Electro-hydrostatic actuator control scheme (Borghetto, 2016, p. 13).

This is the actuator studied in this thesis. In this kind of actuators, the pump is positioned near the actuator and is driven by a brushless motor. There can be two different types of pump: a fixed displacement pump, where the regulation is made by controlling the speed of the motor and a variable step displacement pump, where the regulation depends on the plate of the pump. Thanks to the proximity of the pump to the actuator, weight can be saved, avoiding heavy hydraulic lines. Another quality of this actuator is that the pilot command is transmitted through fly-by-wire lines, avoiding friction losses or linkage flexibility, characteristic of reversible control lines. The feedback signal is obtained through a LVDT (*linear variable differential transformer*) or a RVDT (*rotatory variable differential transformer*), that give information about instantaneous position of the jack to the ACE (*actuator control electronics*). In this way the position error is given the PDE (*power drive electronics*) that regulates the motor angular velocity.

3 SERVO-VALVE FOR POSITION COMMAND

The aim of a servo-valve is to regulate the flow rate of the fluid entering in the actuator. In this way, it is possible to control the position of the actuator and to equilibrate possible forces generated from the aerodynamic hinge moment.

Servo-valves are widely used in aeronautical sector, since the second half of 20th century, both for primary and secondary commands.

To accomplish the actuation, an electric input signal is sent to the torque motor of the servo-valve from the control unit, implemented in this thesis as a PID controller. It uses the error between the commanded position and the instantaneous position of the jack, derived from the closed loop structure of the system, to nullify the position error, leading to the commanded position.

In the following paragraph the flapper-nozzle valve, used in this thesis, will be presented.

3.1 FLAPPER-NOZZLE VALVE

The flapper-nozzle valve is composed of two stages: the first stage consists in an electric torque motor, a flapper and two nozzles that connect the two stages, while the second one comprehends the sleeve, where the spool can move to close or open the four different passageways.

Once the valve is commanded, the spool can move, dependently from the differential pressure caused by the nozzles, and, according to the design of the sleeve, it opens and closes two different passageways, one to supply a chamber of the jack and one to discharge the other one. Feedback between the two stages is represented from the feedback-spring.

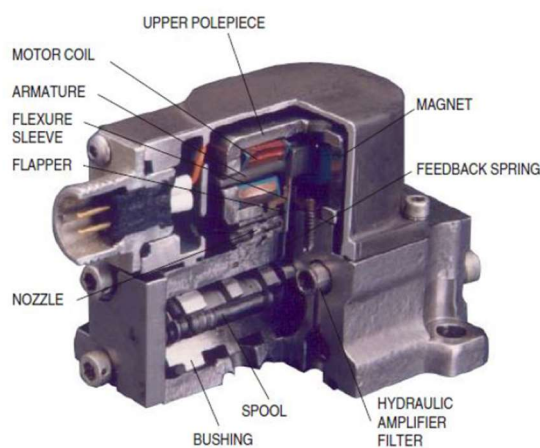


Figure 3.1: Section of a flapper-nozzle valve (Riva, 2019, p. 17).

More details are explained below.

In the torque-motor, the stator is constituted by an upper and a lower yoke, on which a permanent magnet is fixed respectively; the rotor, instead, is formed by an armature with two coils, whose middle position corresponds to null current. The permanent magnets and the coils generate magnetomotive forces between the four airgaps. In the middle of the armature the upper part of a flapper is fixed, while its lower part is positioned between two nozzles equally spaced, so that a rotation of the rotor involves a rotation of the flapper that obstructs one of the nozzles. This rotation is contrasted by the hinge spring and the bending of the feedback spring, while the armature-flapper assembly is supported by a flexure tube, that prevents hydraulic fluid filters in the torque motor.

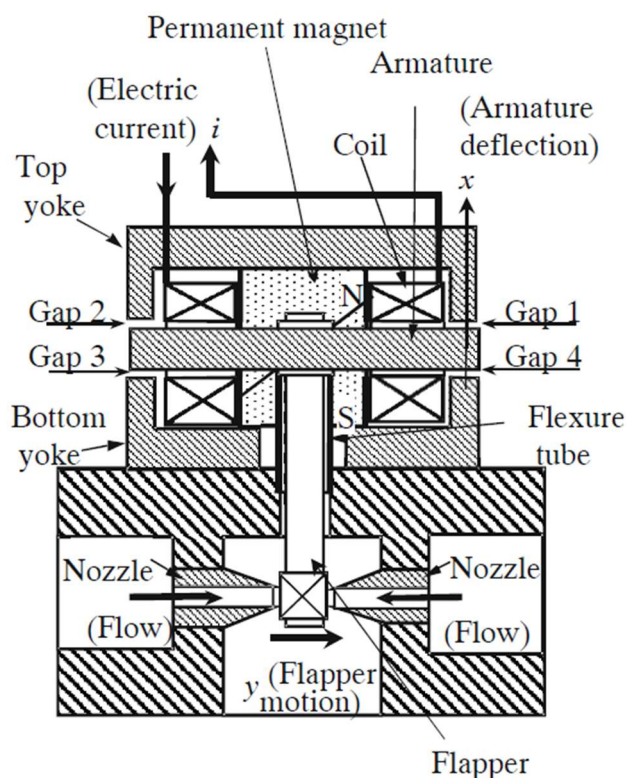


Figure 3.2: Scheme of the torque motor and the first stage of the flapper-nozzle valve (Urata, 2004).

A movement of the flapper on the right or left side, leads to a partial occlusion of one of the nozzles, in this way the fluid from a nozzle will be throttled while the other will be unconstrained. The partial occlusion of one nozzle will cause an increase of the pressure that is reported in the chamber of the spool: a differential pressure on the two surfaces of the spool will make it move in one direction. In the movement of the spool respect to the null position, two passageways will be opened, one supplying a chamber of the actuator and the other will be connected to the tank. The hydrostatic force caused

by the differential pressure is not the only force acting on the spool, but it is also subjected to the feedback spring, as shown in Figure 3.3.

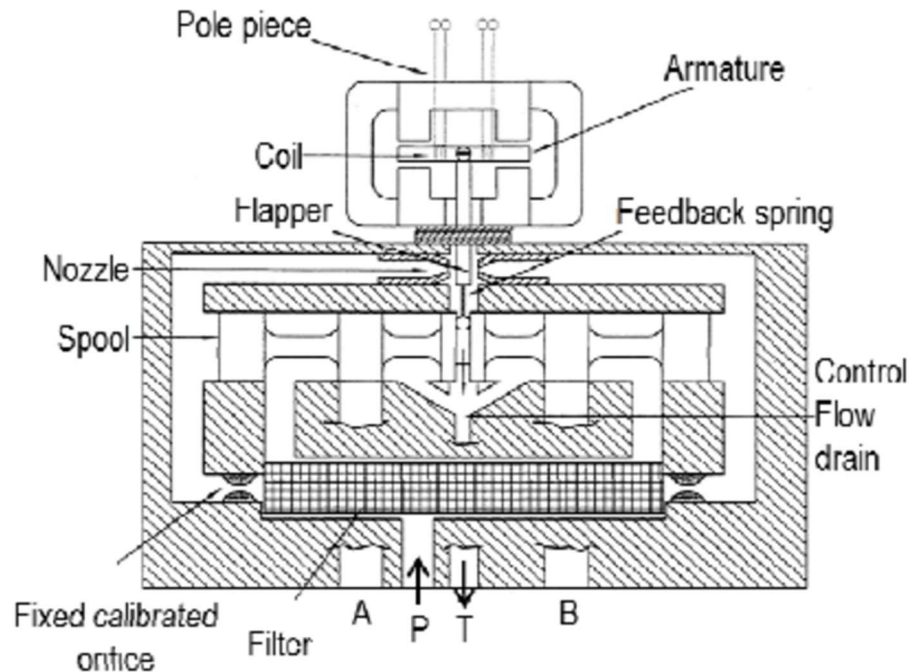


Figure 3.3: Scheme of the first and second stage of the flapper-nozzle valve (Riva, 2019, p. 23).

In fact, the feedback spring is connected between the spool and the flapper and it acts a force to nullify the position error between them. This is a very important contribution to the stability of the system: if the valve is commanded, for example, with a step signal input, the flapper will occlude one of the nozzles causing a differential pressure on the spool chamber; once the jack reaches the new commanded position, the error tends to zero, thanks to the feedback spring that applies a force to report the spool in the null position. This corresponds to the unique position with null error. If the feedback spring were not acting on the spool, the jack would oscillate around the equilibrium position, leading to a limit cycle.

It is important to avoid fluid contamination: the presence of small metal parts can compromise the correct valve functioning. These parts can reach the nozzles and they can be damaged due to the supersonic velocities of the fluid, compromising the null position; they can also reach the ball at the end of the feedback spring and the spool, reducing the precision of the valve. For these reasons, a filter is placed after the supply and return passageways.

This type of valve is the best in commerce thanks to its reliability and dynamic performance in terms of reaction velocity.

3.2 TECHNICAL CHARACTERISTICS OF VALVES AND NON-LINEARITIES

As described before, the aim of valves and servovalves is to control the fluid that supplies the chambers of the actuator: the control is applied through the position of the spool that close or open the different passageways. In general, both pressures and flow rates that supply the actuator depends on external conditions (load and pressures of supply and return): a useful way to describe all these aspects is with the characteristic curves of the valve.

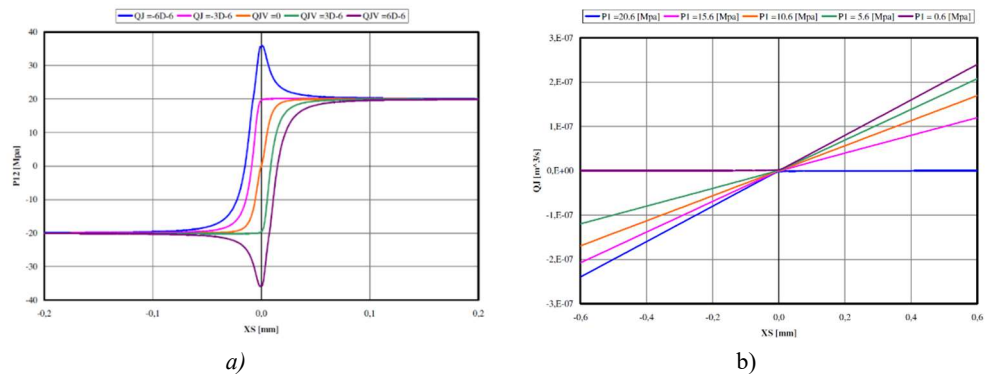


Figure 3.4: Characteristic curves of a valve, pressure-displacement (a), flow rate-displacement (b). (Dalla Vedova, 2007, p. 84-85).

In Figure 3.4 a) the characteristic curves pressure $P12$ -spool position XS are shown: given a fixed value of flow rate QJ (in this example equal to $-6 \text{ m}^3/\text{s}$, $-3 \text{ m}^3/\text{s}$, $0 \text{ m}^3/\text{s}$, $+3 \text{ m}^3/\text{s}$, $+6 \text{ m}^3/\text{s}$), the correspondence between the input XS and the output $P12$ is explained (controlled pressure is function also of the geometric characteristics of the valve, supply and return pressures). It is interesting to observe that, for great values of spool displacement XS , the pressure $P12$ is almost equal to the supply pressure, while for small values of XS the pressure can assume values greater than the supply pressure: this is the typical case of rapid closure of the spool, where the fluid still has velocity while the passageway is closed, leading to the water hammer.

In Figure 3.4 b) the characteristic curves flow rate QJ -spool position XS are shown: given a fixed value of pressure PI (equal to 0.6 MPa, 5.6 MPa, 10.6 MPa, 15.6 MPa, 20.6 MPa), the correspondence between the input XS and the output QJ is explained. In this case, two different horizontal segments can be observed: the first represents the flow rate with a $PI=0.6$ MPa, while the second represents the flow rate with $PI=20.6$ MPa; these are the case when the pressure PI is equal to the return pressure in the first case and to the supply pressure in the second one, leading to null flow rate because no differential pressure is present.

It can be convenient to adopt some simplifications: since this study is focused on proximity of the null spool position, it is possible to apply the superposition effect on

XS , considering two different contributions on the pressure and flow rate. These simplifications are adopted considering the flow rate gain GQ and the pressure gain GP . The flow rate gain is defined as the slope of the curve $QJ-XS$ at null values of pressure $P12$, while the pressure gain is defined as the slope of the curve $P12-XS$ at null value of flow rate QJ .

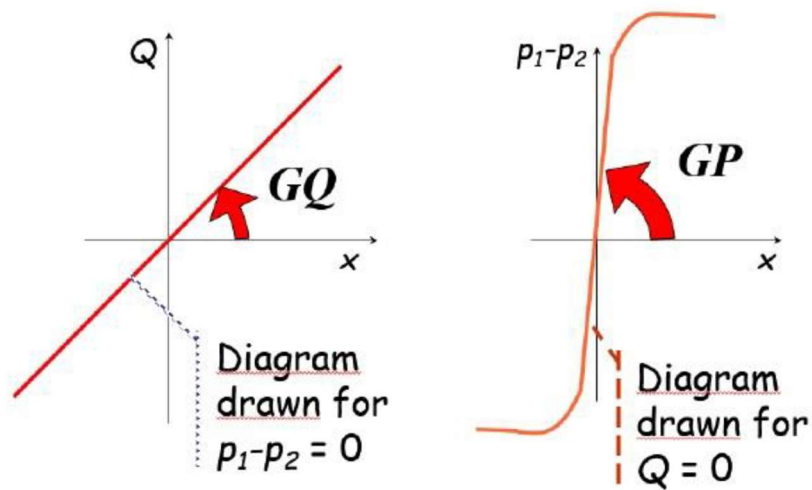


Figure 3.5: Flow rate and pressure gains definition (Borghetto, 2016, p. 20).

This can be a powerful method to understand the performance of a valve in a preliminary phase, but it could be necessary to study other aspects of the valve. In the paragraphs below are described the main.

3.2.1 Lapp Condition

Three different constructive choices can be done in a valve about the lapp condition: null lapp, overlapping and underlapping.

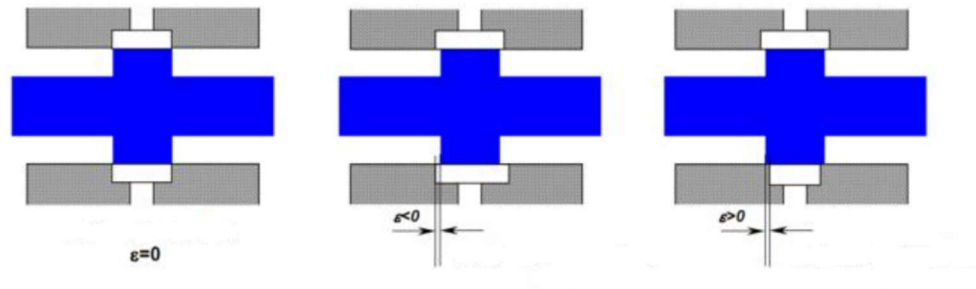


Figure 3.6: Different lapp conditions in a valve (Borghetto, 2016, p. 21).

When the spool has the same dimension of the passageway, it is called zero-lapped: in this case there is only one position of the spool that closes completely the passageway, while a displacement leads to an immediate response of the valve in terms of pressure and flow rate. It is usually used to not create non-linearities in the null position neighbourhood, in this way the pressure and flow rates gain are almost constant in this interval.

An overlapped valve is a condition where the spool has a width excess respect to the passageway: it is usually used to compensate the static leakage due to clearance; moreover, it creates a dead zone where an axial displacement of the spool does not create any flow rate.

An underlapped valve, instead, is a condition where the spool is slightly smaller than the passageway, so even at null position, the passageway is not completely closed. It is usually used to prevent water hammer due to rapid closure of the valve. In this case, even in null position, the valve has a response in terms of pressure and flow rate.

The responses to an input of all three conditions described above are shown in the figure below:

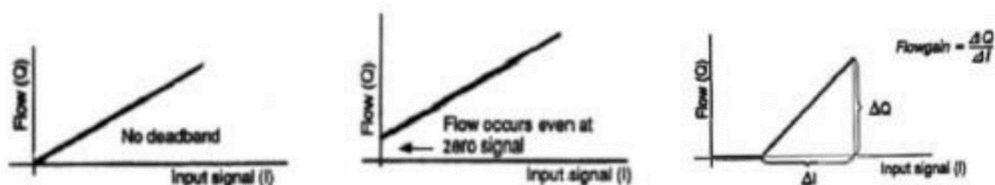


Figure 3.7: Schemes of the response of the three lapp conditions (Borghetto, 2016, p. 21).

3.2.2 Threshold

Threshold is defined as the minimal input current required by the valve to vary the fluid flow rate when a directional inversion is commanded; it can be seen also as the minimal variation of current that leads to a change in the response of the valve. It indicates how much a valve is sensible to a variation of the input current.

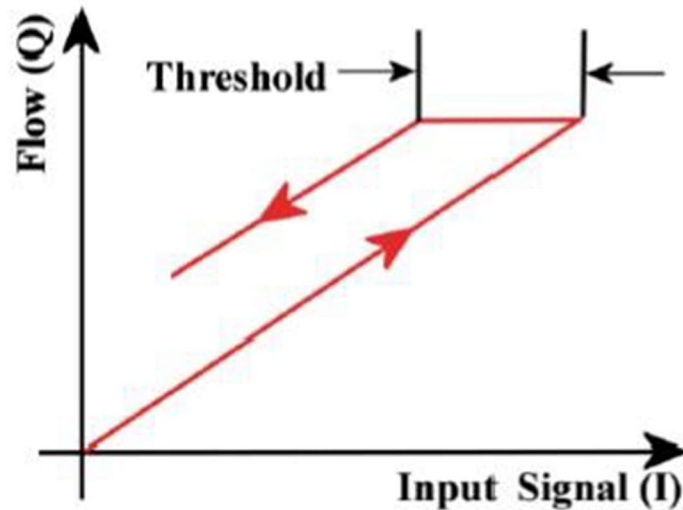


Figure 3.8: Graphical interpretation of threshold (Borghetto, 2016, p. 22).

3.2.3 Magnetic hysteresis

Magnetic hysteresis is an important source of non-linearities and it is defined as the characteristic of a system to react, not only to instantaneous values of input, but also to time history of states. It is typical of magnetic materials and, obviously, of all their applications (transformers, electric motors and so on). In the graph below, typical response of a system with hysteresis is shown:

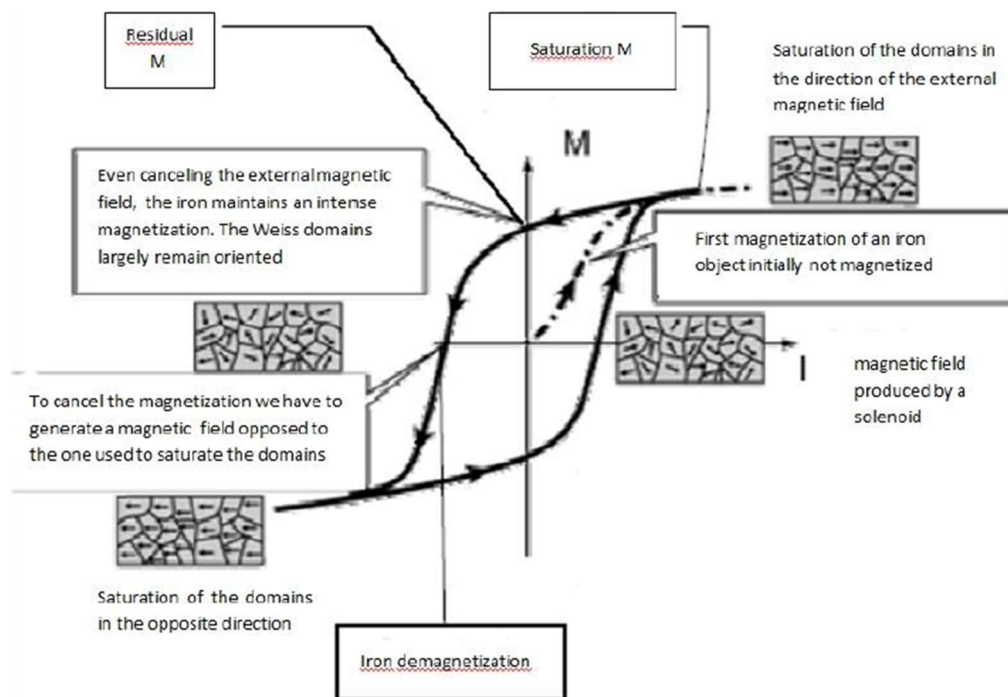


Figure 3.9: Typical hysteresis scheme of electric motors (Borghetto, 2016, p.30).

Initially, when the system is not magnetized, the magnetization follows the first curve: in this case, increasing the current also the magnetization increases, but not in a direct proportionally way. Over a certain value of the current I , the magnetization B will reach a saturation value B_{sat} : this is due to the fact that in the first magnetization curve, the Weiss domains of the material gradually orient themselves to the external magnetic field; this leads to an increase of the magnetization until they are all oriented in the same direction and reaching the saturation. Then, if the current is decreased to 0, it can be noticed that the curve is different from the first: in particular, B will not be equal to 0, but it will assume a positive value; in this phase some of the Weiss domains will maintain the previous orientation, leading to a residual magnetization of the material. To demagnetize the material, a current of opposite sign must be applied and, if the current is applied for more time, the material will be magnetized in the same direction, reaching a new value of saturation, opposite to the first. Finally, decreasing the current to 0 and increasing it in the opposite direction, the curve will be closed, as represented in Figure 3.9.

Hysteresis diagrams can be quite different from the presented one, dependently from the analysed material: hard ferromagnetic materials usually have a higher residual magnetization respect to the soft one and for this reason, they have different applications. However, all the ferromagnetic materials can lose their magnetization due to the natural demagnetization in time (ductile iron case) or heating the material over its Curie temperature (recovery of permanent magnets case).

In the system analysed in this thesis, magnetic hysteresis affects the torque motor of the first stage of the servovalve, where, even if the current is no more applied, the magnetic field continues to attract the armature.

3.2.4 Friction

Friction is a crucial point in the study of the system, since it influences the whole system: it is a strong non-linear phenomenon that limits the position accuracy needed in the aeronautical sector.

Friction is a force that is present between two surfaces that are in contact, opposing to their relative motion. If the surfaces have not relative velocity, static friction is present, in the other cases, there will be dynamic friction. There are three different types of friction:

- Sliding friction, it is the case of two surfaces slipping.
- Rolling friction, it is involved when a body roll on a surface.
- Viscous friction, it is present when a body or a fluid layer has a relative velocity respect to the layer below.

Considering only the static and dynamic friction, their expressions are:

$$F_s = \mu_s \cdot N$$

$$F_d = \mu_d \cdot N$$

where μ_s and μ_d are respectively the dimensionless static and dynamic friction coefficients, depending by the materials on contact and N the normal reaction of the ground to the body. If a body in contact with a not lubricated surface is considered, applying a driving force, the friction force will have the sequent behaviour:

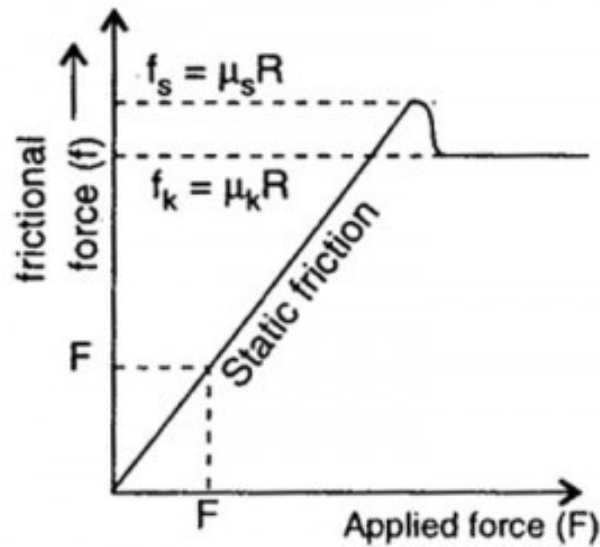


Figure 3.10: Friction force behaviour.

As it can be seen from Figure 3.10, when a force smaller than the friction is applied, the body is still in quiet, but, as soon as it reaches the maximum value of the static friction, the body will move and the friction will decrease to an almost constant value, equal to the dynamic friction. In this case, to have a good friction model, four different situations must be discriminated:

- Body in quiet that remains in quiet,
- Body that starts moving,
- Body in motion that continue to be in motion,
- Body in motion that stops.

One of the first friction models is the Coulomb model: neglecting the local dynamic phenomena, it grants a good global representation of the friction and it can be described by the sequent equations:

$$FF = \begin{cases} F_{att} & \text{if } v = 0 \wedge |F_{att}| \leq FSJ \\ FSJ \cdot \text{sign}(F_{att}) & \text{if } v = 0 \wedge |F_{att}| > FSJ \\ FDJ \cdot \text{sign}(v) & \text{if } v \neq 0 \end{cases}$$

Every situation identified before are visible in this mathematical description.

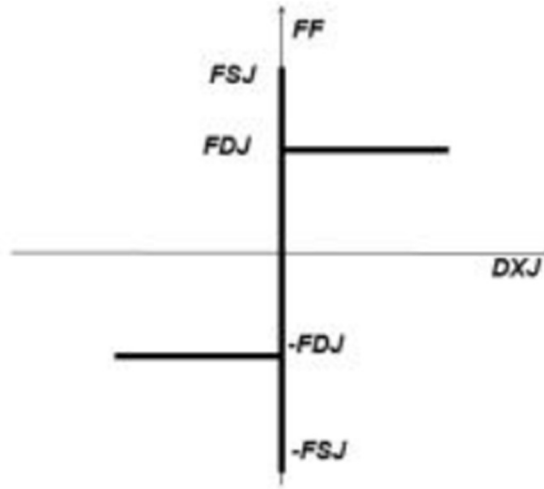


Figure 3.11: Graphical description of the Coulomb friction model (Borghetto, 2016, p. 26).

As convention, the friction force FF is positive when it is opposite to a positive velocity.

However, this model is not suitable for numerical simulations, because of the discontinuity in $v=0$: integrating the acceleration in the two different cases, two different velocities values of opposite sign are obtained; in this way, the model can not recognize when the speed reaches the null value, so it can not verify the possible arrest of the body. This verification can not be neglected as, if the body is in quiet, the resultant active force can be smaller than the static friction. These limits bring to the development of new friction models: in this thesis two different models will be analysed, Karnopp and Borello.

Karnopp model compensates the discontinuity of the friction force in correspondence of null velocity, introducing a dead band centred in the origin. Through this dead band, it is possible to distinguish the cinematic differences between static and dynamic friction, in particular the static friction can equilibrate the external forces applied, maintaining the null value of acceleration and so, avoiding the start.

The mathematical formulation of the model is shown below:

$$FF = \begin{cases} \min(\max(-FSJ, F), FSJ) & \text{if } |v| \leq \varepsilon \\ v = 0 & \text{if } |v| \leq \varepsilon \\ FDJ \cdot \text{sign}(v) & \text{if } |v| > \varepsilon \end{cases}$$

where F is the driving force and ε is a small enough value of the velocity under which the velocity is considered equal to 0. It is very important to choose the right value of ε :

if it is chosen too high the simulation results will be very far from the real data, emphasizing the Karnopp model limits, while, on the other hand, if it is chosen too small, the model can not discriminate the static from the dynamic state. In other words, a value of ε too high brings the calculations to a limit cycle, while a value too small leads to numerical instability.

A graphical representation of the Karnopp friction model is shown below:

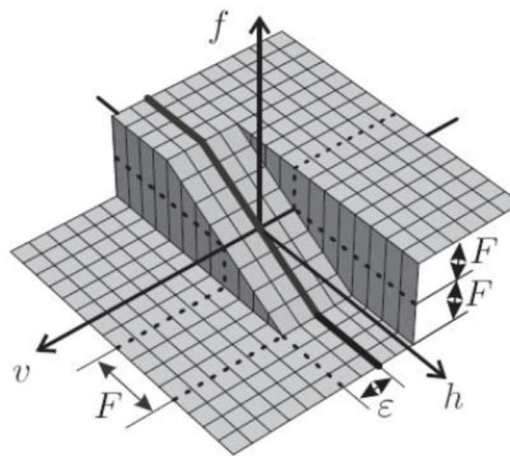


Figure 3.12: Graphical representation of the Karnopp model (Borghetto, 2016, p. 27).

From the equations explained previously, the sequent Simulink model has been obtained:

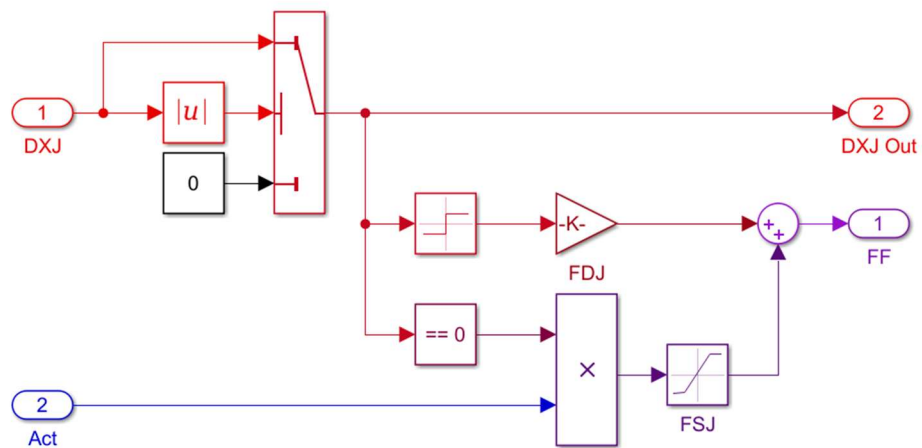


Figure 3.13: Simulink Karnopp model.

A new model of friction has been developed by professor of Politecnico di Torino Borello, overcoming the limits of the Karnopp model: it can, in fact, correctly distinguish the static condition from the adherence one, discriminating the four cinematic situations described at the beginning of this paragraph.

Below, the mathematical and graphical representation of this model are reported:

$$FF = \begin{cases} F_{att} & \text{if } v = 0 \wedge |F_{att}| \leq FSJ \\ FSJ \cdot \text{sign}(F_{att}) & \text{if } v = 0 \wedge |F_{att}| > FSJ \\ FDJ \cdot \text{sign}(v) & \text{if } v \neq 0 \end{cases}$$

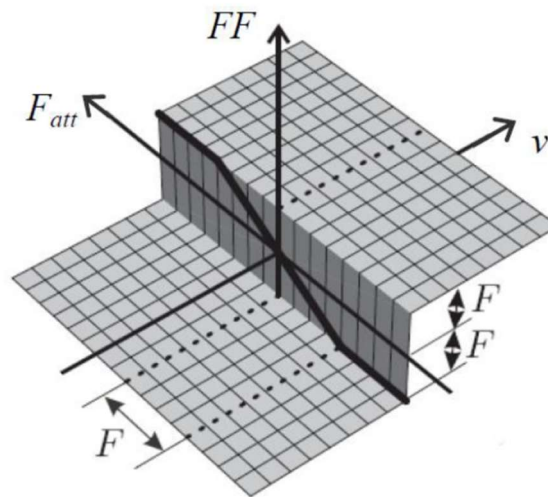


Figure 3.14: Graphical representation of Borello friction model (Borghetto, 2016, p. 28).

Despite to the Karnopp model, this one does not need a dead band, in fact, if a change of sign in the velocity is detected in an integration interval, the algorithm resets the velocity, arresting the system; if an external force is present and the body would not arrest, at the following integration step a decompensation is created between the forces, enabling the system to move again. These characteristics do not only make the model more performing respect to the others in literature, but it is also easy developable on Simulink, obtaining the sequent scheme:

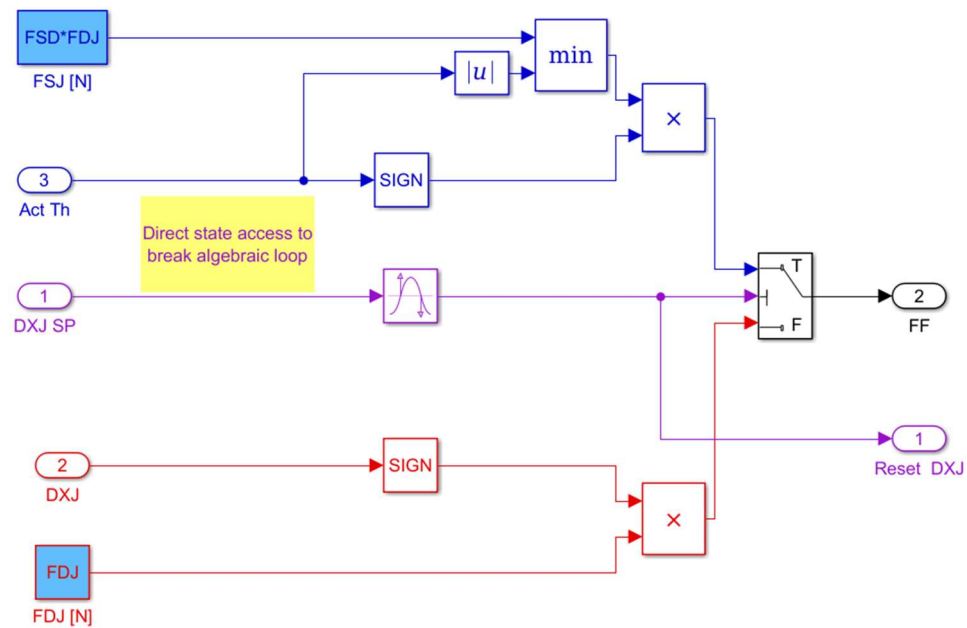


Figure 3.15: Simulink of Borello friction model.

3.2.5 Backlash

Backlash is a clearance between two coupled mechanical components that allows their relative movement. It can be defined as the maximum distance or angle through which a mechanical component can move without transmitting any appreciating force or couple to the next component. Due to this, a time delay can be present in the system respect to an inversion of the input, in fact it is one of the most important factors that influences the system performances. It is an inevitable consequence of the mechanical processing of the component manufacturing, because every process leads to tolerances in the dimensions. Usually, it is also present to permit the coupling of two or more components or to compensate the thermal expansion of materials. Moreover, during the life of the component, backlash can increase because of continuous contact with other components, leading to a further deterioration of the system performances and to a decreasing precision in the relative positioning of components.

3.2.6 Offset valve

The offset usually indicates an error respect to a reference value. About the servovalve, it can affect the electric motor, even when it is not active. In fact, even if the motor is deenergized, a minimal input current can be present. This current can partially energize the torque motor and it can open partially the passageways of the servovalve, actuating the jack even if no input is present.

4 SIMULINK MODEL

Traditionally, projects of aeronautical components were developed separately from the others to have just an estimation of their performances. Real interactions between components were validated successively through ground tests or flying tests: in this way, any error in the project phase was very expensive in terms of time and costs.

Nowadays, aeronautical sector, as the automotive one and many others, needs instruments to prove new solutions or to improve applications of already existing components, without creating and testing any prototype; in this case, modern computers, that are becoming powerful and powerful, can give an important support to the design, simulating the interested behaviour of a system.

In the new approach to design, all problems are solved before the flying testing, through numerical simulations. In this way, development of new models, more accurate, are essential to predict interactions and dynamic of systems. Moreover, models are very important in diagnostic and prognostic fields: through the model-based approach, it is possible to estimate useful life of a component, for example, comparing its time response, coming from a sensor, with the one coming from models. If the responses difference exceeds a security threshold, a fault signal is sent to the pilot during the flight; once landed, the same fault signal can be sent to the maintenance that can identify both location and entity of the fault and, eventually, substitute the damaged component preventively. In this way, useful lifetime of components is completely used, without replacing the whole mechanical assembly, saving both time and economic costs.

To develop a satisfying model, several steps are needed:

- 1) Mathematical modelling of the physic system.
In this first phase, all the aspects, peculiar characteristics and components of the system are identified: it could be necessary to describe how a mass react to a force (application of the dynamic laws), the energy of the system, the heat transfer or electro-magnetic interaction (application of Maxwell's laws). Because of high complexity of certain systems, it could be useful to apply some simplification or approximation in the model without losing its validity. In other words, it is necessary to find a compromise between complexity and usefulness.
- 2) Formulation of the equations.
Once the mathematical model has been developed, it is necessary to apply all the laws that govern the analysed phenomenon, also introducing the material and geometrical characteristics of the system: the result will be a set of independent differential equations that describe the system in all its main aspects (dynamic, cinematic, thermal, chemical and so on).
- 3) Resolution of the equations.
In aeronautical field, mathematical problems are usually defined in time or frequency domain: it is almost impossible to analytically solve a set of non-linear differential equations, so a numerical integration must be adopted to evaluate the dynamic response of the system. Two important aspects must be chosen carefully: the first one is the order of the resolution numerical method

(ODE), where a higher order can lead to more accurate simulation results but with higher computational effort; the second one is the time interval chosen as integration time, that must be smaller than the smallest time constant of the system, other ways it can lead to numerical instability.

4) Physical interpretation of the obtained data.

To make a model valid, its results must be compared with the experimental data and, if any inconsistency is present, it must be reviewed. In other words, models can save time and money, but they cannot substitute experimental tests.

In this thesis, two different models of the same EHA are present: the first, called High-Fidelity, is developed by Ing. Dalla Vedova, it has a high level of accuracy and it is used as a reference for the second one, called Low-Fidelity, it uses some approximations, but it is quicker and less demanding in terms of calculation effort and for this reason it is used in the optimization algorithms (explained in the next chapter).

Both models analysed in this thesis are developed on MATLAB-Simulink 2016b release.

4.1 REFERENCE MODEL

In this paragraph the whole High-Fidelity system and its functioning will be described.

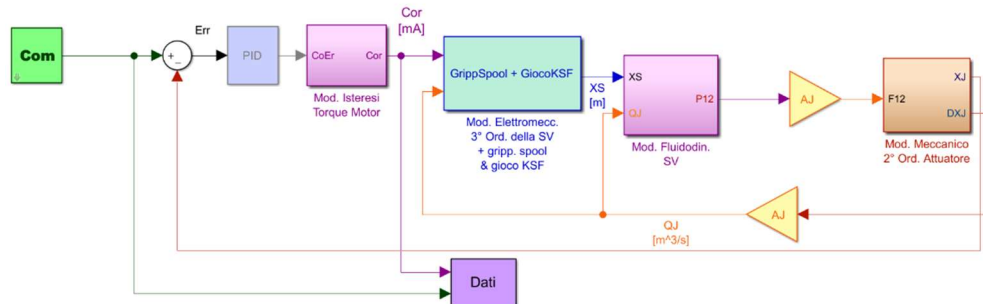


Figure 4.1: Simulink representation of the High-Fidelity model.

The system is represented as a closed loop system, where the variable XJ (instantaneous position of the jack) is feedbacked to compute the error signal that entries in the PID controller.

The first block is the command block: it is possible to provide different reference signals in time domain to the system; five different inputs can be provided: three standard signals (step, ramp and sine wave) and two custom signals (chirp signal, a sine wave with variable frequency in time, and Com signal composed of different subsequent step signals with variable amplitude).

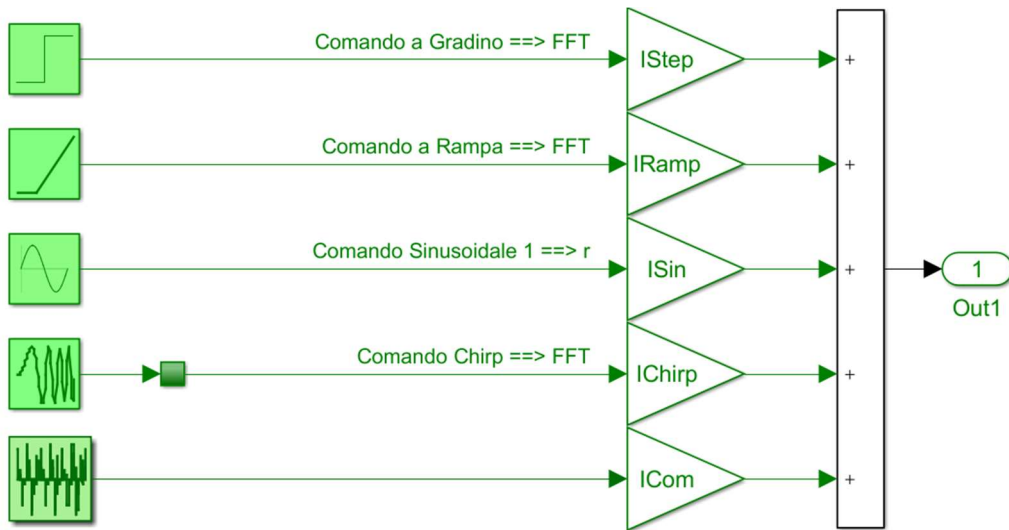


Figure 4.2: Sub-system of the input block.

The error between the instantaneous position of the jack and the selected command is elaborated from a PID controller: its aim is to stabilize the dynamic response of the system. The PID controller is composed by three parallel contribution: integrational gain (*GAI*), proportional gain (*GAP*) and derivative gain (*GAD*).

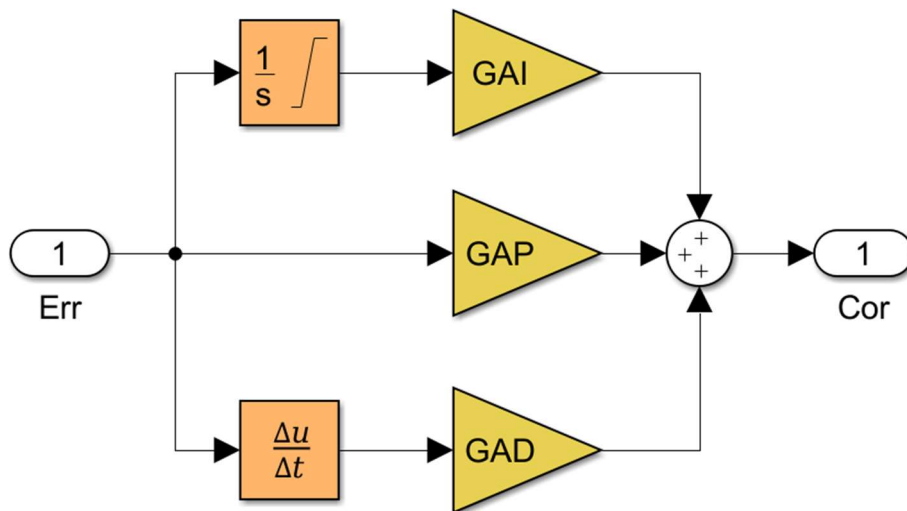


Figure 4.3: Scheme of the PID controller.

In this case, only the proportional gain has a non-null value, so the PID controller is used only as a proportional controller, thanks to the already granted stability of the system.

Then, the error signal feeds the hysteresis block of the torque motor: this block permits to introduce both an offset on the current input and a disturbance due to external factors.

The output of the hysteresis block represents the actual current that supplies the valve. The flapper-nozzles servovalve is represented as a third order system and it is composed of other two sub-blocks: a second order dynamic system for the first stage and a first order dynamic system for the second. Also, the flow rate QJ is feeded back to the second stage to calculate the flow force acting on flappers.

The output XS is the spool position, but, as it can be observed in Figure 4.1, also the flow rate is feeded back from the output of the whole system: these are two important physical quantities, since the first, with the pressures $P1$ and $P2$, is used to calculate the flow rate through each opening width, while the second one is used with $Q1$ and $Q2$ to calculate the differential pressure $P12$.

Then, the differential pressure $P12$ is multiplied by the jack's surface area to obtain the force supplying the actuator and it enters in the last block, the second order mechanical model of the actuator. Through the second principle of the dynamic, the position and the velocity of the jack are calculated, considering also external and aerodynamic forces, friction and displacement limits.

4.1.1 Hysteresis, offset and interferences in the torque motor

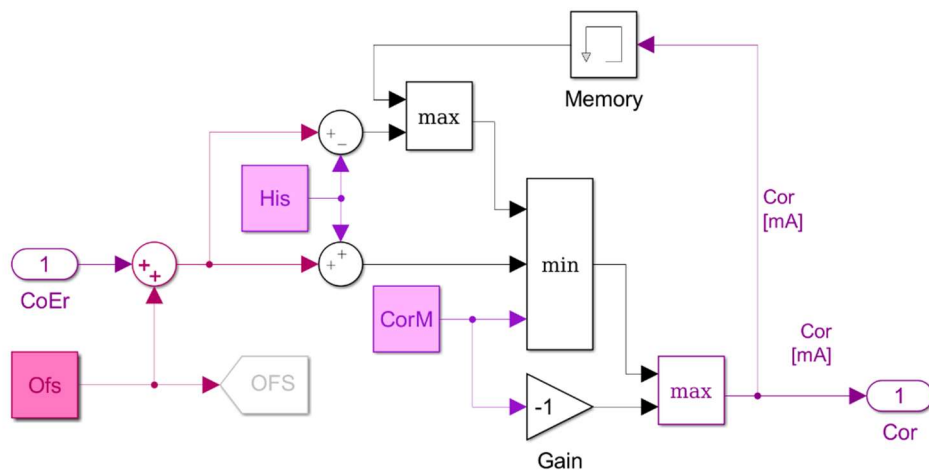


Figure 4.4: Torque motor hysteresis model.

This block's aim is to represent disturbances and non-linearity of the current entering in the model of the torque motor. It receives as input the control signal $CoEr$, given by the controller. This signal is algebraically summed with the values of His and Ofs . If the signal is rising it will be decreased of the value His , while if it is falling it will be increased of His , to represent the hysteresis of the motor. The block Ofs , instead (shown in Figure 4.5), permits to impose an offset value of the current due to a bad setting of neutral command, but it is also possible to introduce an external source of interferences: this source is represented as a Band-Limited White Noise block, whose contribute is a random signal with constant power spectral density. At the end, the resulting current will be saturated, if necessary, to the maximum or minimum values $CorM$ and $-CorM$, the current limits that can feed the servovalve.

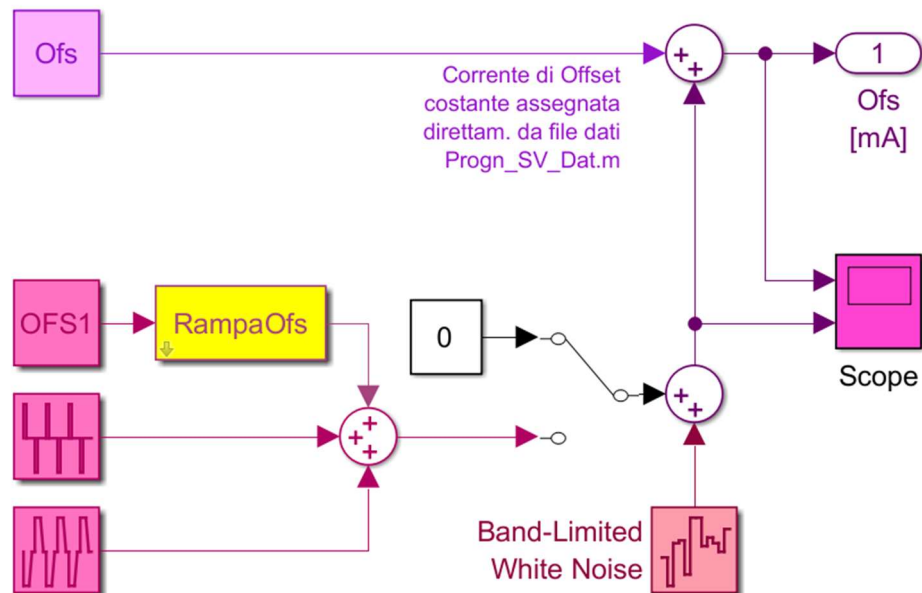


Figure 4.4: Different types of offset current model.

4.1.2 Electromechanical model of the servovalve

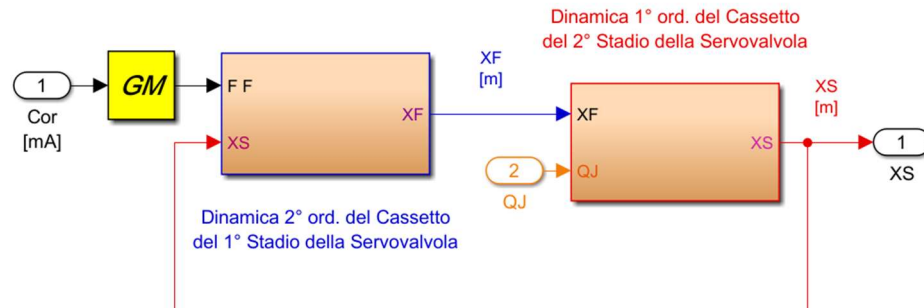


Figure 4.5: Third order electromechanical model of the servovalve.

This block represents the third order electromechanical model of the servovalve: it is composed by two sub-blocks describing the dynamic behaviour of the first and the second stage of the servovalve, respectively. As it can be seen in Figure 4.6, the signal *Cor* is sent to the block *GM*: it computes the gain of the torque motor (in (Nm/mA)/m).

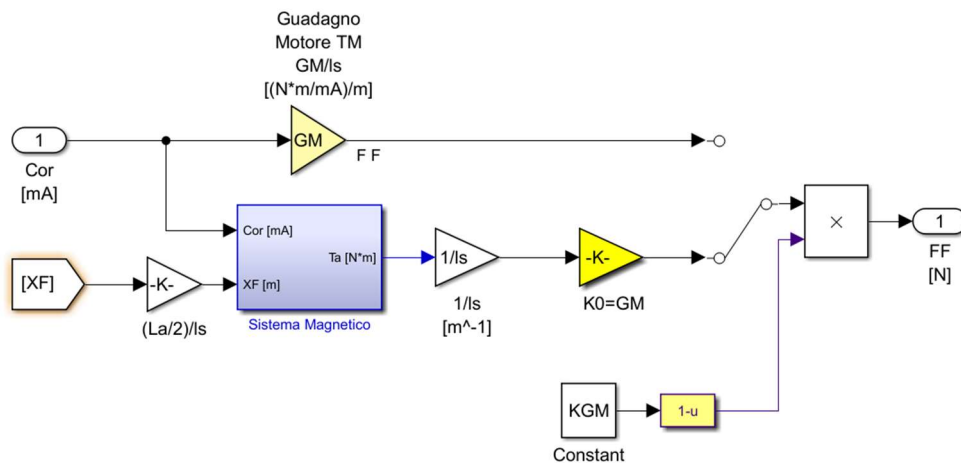


Figure 4.6: Calculation of the gain *GM*.

Two different values of *GM* can be used: the first one is the fixed value already calculated, the second one considers the structure, the configuration and the magnetic circuits of the motor, accordingly to the sequent picture.

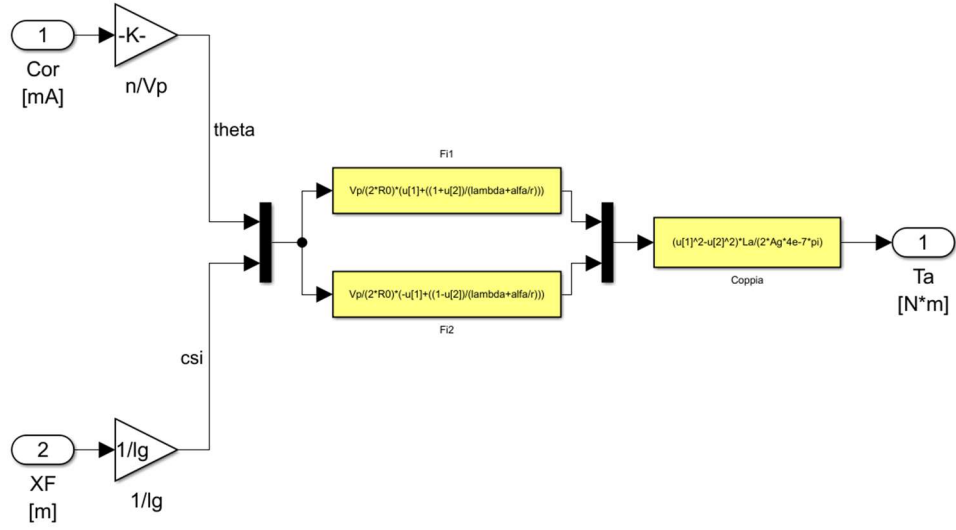


Figure 4.7: Magnet circuit of the torque motor.

In the second branch of the calculation, there are two inputs: Cor , the value of the current from the previous block, and XF , the position of the flapper feedbacked from the second order dynamical model of the first stage. At first, XF is multiplied for the gain $(La/2)/ls$, where La is the total length of the anchor and ls represents the arm of the spool: in this way the rotation of the armature is calculated and, multiplied by $La/2$, the vertical displacement of the armature is obtained. These two values are used to calculate the magnet flux in all the airgaps:

$$\Phi_1 = \frac{V_p}{2R_0} \frac{1 - \frac{XF}{lg}}{\lambda + \alpha * r} + \frac{Cor * n}{2R_0}$$

$$\Phi_2 = \frac{V_p}{2R_0} \frac{1 + \frac{XF}{lg}}{\lambda + \alpha * r} - \frac{Cor * n}{2R_0}$$

Where:

n = number of winding in the armature;

R_0 = reluctance of the airgap in null current condition;

V_p = residual magnetic induction;

lg = total length of the air-gap;

λ, α, r = correction factors that consider the edge effects of the magnetic flux in the extremity of the armature.

As it can be seen by the formulas above, there are two contributions in the magnetic flux: the first term represents the magnetic flux given by the permanent magnets of the yokes through air gaps with reluctance $R = \frac{2R_0}{1 \pm \frac{XF}{lg}}$, while the second term with opposite sign represents the contribution to the flux created by the current in the coils.

Once fluxes through airgaps are calculated, the total torque can be obtained from the formula:

$$T = \frac{(\Phi_1^2 - \Phi_2^2) * La}{2 Ag \mu_0}$$

Where

La = length of the anchor;

Ag = section of the air-gap;

μ_0 = magnetic permeability in vacuum.

To find the value of the force applied to the centre of the flapper, the torque is finally divided by the length of the anchor; moreover, to obtain a stable model, another gain, constant in time, is added, equal to the value of GM .

To simulate the behaviour of the system in presence of demagnetization of the torque motor, the force is multiplied by $I-KGM$, with KGM in the range from 0 (torque motor in normal condition) and 1 (motor completely demagnetized).

Going on next block, the model of the first stage of the servovalve will be analysed.

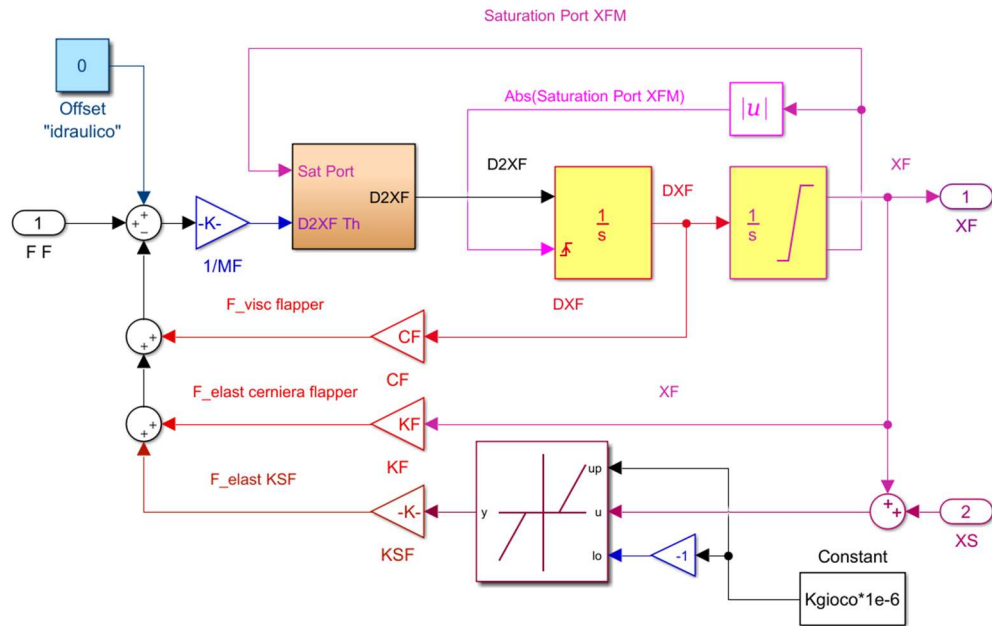


Figure 4.8: Second order dynamical model of the first stage of the servovalve.

The force applied to the flapper enters in the second order dynamic block; this is not the only input used, since also the variable XS , the instantaneous position of the spool, is feedbacked from the second stage dynamic model: this feedback has a physical meaning, because it represents the information carried out by the feedback spring that, proportionally to its bending stiffness, report a force to the flapper. This bending effect is considered by summing, and not subtracting, the spool position to the flapper position due to the opposite reference systems of the two. Multiplying the result for the elastic constant, the resultant force of the feedback spring is obtained; there is also a dead zone dynamic mask to simulate the backlash between the spool and the ball. To simulate the degrading of this backlash another parameter has been introduced: $Kgioco$ can be imposed from the associated data file and it is expressed in micron.

Considering the intermediate closed loop branch of the model, the position of the flapper is used to calculate its elastic return, by multiplying it for the constant KF , the stiffness armature-bolt.

Finally, in the inner closed loop branch, the viscous reaction of the fluid to the flapper displacement is calculated: it is proportional to the velocity of the flapper and the proportionality constant is CF (in N/m/s), obtained from the formula above:

$$CF = 2 * ZF * \sqrt{MF * (KSF + KF)}$$

Where

ZF = dimensionless viscous coefficient;

MF = equivalent mass of the flapper;

KSF = linear term of the translational stiffness of the feedback spring between first and second stage of the servovalve;

KF = stiffness armature-bolt.

These three forces are subtracted to FF , to obtain the net force acting on the flapper. Dividing it for the equivalent mass of the spool MF , its acceleration is calculated; with two successively integrations also the velocity and the position of the spool are obtained. Robustness is given to the model by inserting saturation: if the flapper reaches the limit positions $+XFM$ or $-XFM$, the displacement integrator switches to $+1$ or -1 the saturation port; this value is passed successively to the acceleration reset block, cancelling any acceleration and velocity.

It is also possible to impose a hydraulic offset to shift the working point in another equilibrium condition.

Analysing the second stage of the servovalve, it is represented as a first order dynamic model.

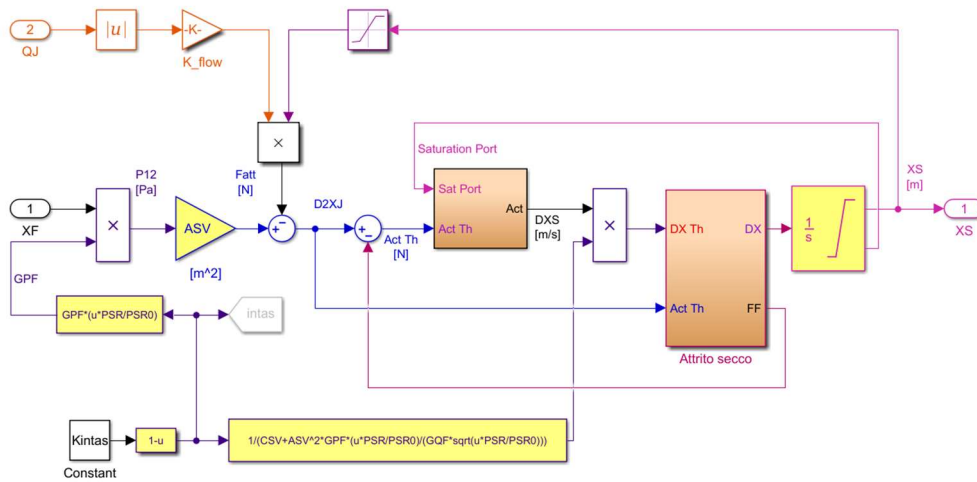


Figure 4.9: First order dynamic model of the second stage of the servovalve.

To simplify the model in the interaction between the flapper and the nozzles, it has been assumed a behaviour of a simple valve, with its own pressure and flow rate gains.

About the dynamical behaviour of the valve, the hydraulic force acting on the spool is given by

$$F_{idr} = (P_1 - P_2) \cdot ASV$$

where ASV is the lateral area on which the differential pressure acts.

Considering all the forces acting on spool, a second order differential equation can be written:

$$M_{SV}\ddot{x}_S + C_S\dot{x}_S + K_{SV}(x_S - x_F) = F_{idr} - F_{frict} - F_{fl}$$

Substituting the expressions of the hydraulic force and the flow force and neglecting the elastic force, the equation below is obtained:

$$M_{SV}\ddot{x}_S + C_S\dot{x}_S = ASV \cdot P_{12} - F_{frict} - K_{flow} \cdot QJ$$

This represents a second order differential equation with a time constant too small: the inertial effects are neglectable with respect to the others and an integration interval smaller than the smallest time constant of the model must be adopted, resulting in a calculation time too long. To make the algorithm faster, the mass of the spool is neglected, degrading the system in a first order system (pressure P12 has been expressed combining the expressions of pressure gain and flow gain and considering $QJ = \dot{x}_S \cdot ASV$):

$$C_S\dot{x}_S = ASV \left(x_F - \frac{\dot{x}_S \cdot ASV}{GQF} \right) GPF - F_{frict} - K_{flow} \cdot QJ$$

and collecting all terms in \dot{x}_S :

$$\dot{x}_S \left(C_S + ASV^2 \frac{GPF}{GQF} \right) = ASV \cdot GPF \cdot x_F - F_{frict} - K_{flow} \cdot QJ$$

The theoretical velocity of the spool is given as input to the Borello's friction model: this block provides as output the friction force, that is feedbacked and subtracted to the theoretical force acting on the flapper, and the actual velocity of the flapper; it is then integrated to obtain the flapper position, also considering the limit positions $+XSM$ and $-XSM$.

The degradation of the filter has an important role in these calculations and a coefficient K_{intas} has been introduced, varying from 0 (filter in nominal conditions) to 1 (filter completely clogged); the quantity $intas = 1 - K_{intas}$ has been used to correct the pressure gain with respect to the nominal conditions through the sequent relation:

$$GPF_{true} = GPF_0 \cdot \left(intas \cdot \frac{PSR}{PSR_0} \right)$$

where:

PSR_0 = nominal differential pressure supply-return;

PSR = actual differential pressure supply-return.

The value *intas* is used also to correct the flow rate gain, according to the relation:

$$GQF_{true} = GQF_0 \cdot \sqrt{\text{intas} \cdot \frac{PSR}{PSR_0}}$$

These two relations allow to consider a variable pressure on the line (in this case constant) by modifying associated data files.

4.1.3 Fluid dynamic model

The presented fluid-dynamic model has been developed by Ing. Dalla Vedova during his PhD research.

In this paragraph the mathematical fluid-dynamic model of a servovalve with proportional control will be presented. With this model it is possible to calculate, having a defined spool position XS , flow rates sent to the actuator based on the pressures it defines, considering all the geometric details of the cross sections and the actual pressure drops through them. The model consider only the fluid-dynamic part and it has general validity, regardless of the way in which the spool is moved, so it can be used to simulate both hydromechanical and electromechanical valves. This fluid-dynamic model is referred to Figure 4.10 in a typical configuration with four ways, supply (S) and return (R):

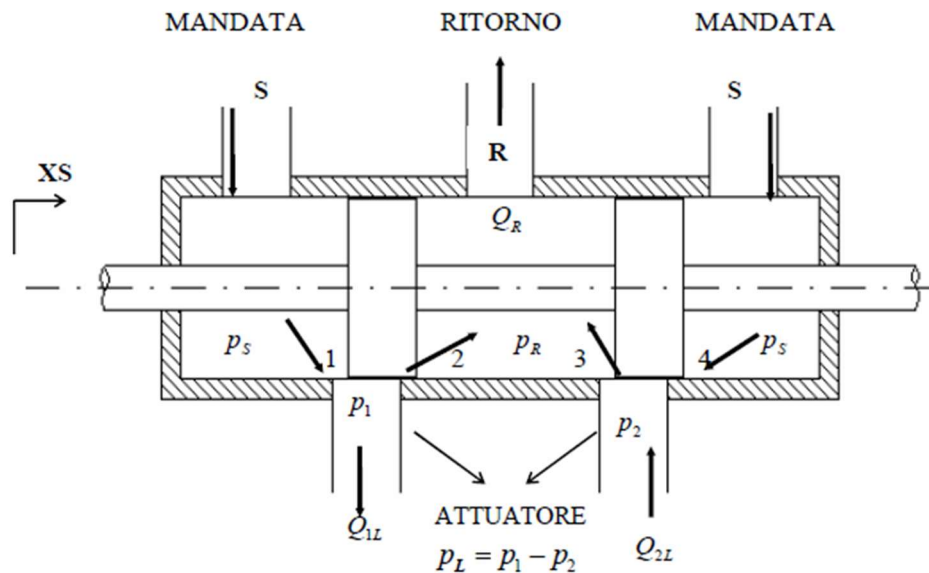


Figure 4.10: 4/3-way directional control valve scheme (Dalla Vedova, 2007, p. 65).

This model calculates the flow through each cross section depending on the position of the spool position, the geometric details of the valve and the differential pressure across them. There are two contributions on the differential pressure drop: the first is linear with the flow rate and expresses the laminar condition of the fluid, while the second, quadratic with the flow rate, expresses the turbulent condition. In the first case the pressure loss is caused by the viscous friction of the fluid and it is present only when the passing section is covered by the spool, while in the second case it is caused by the discharge of kinematic energy through the passing section and always present because it is related to the passing area, greater than zero. The two terms are defined as:

$$\Delta p_{lin} = RL Q$$

$$\Delta p_{quad} = RQ |Q|$$

where RL is the pressure drop linear coefficient and RQ is the pressure drop quadratic coefficient. RQ and RL can be expressed as:

$$RL = \frac{6 \mu l}{\pi r c^3 \left[1 + \frac{3}{2} \left(\frac{e}{c} \right)^2 \right]}$$

$$RQ = \frac{\rho}{2 C_d^2 A^2}$$

where:

μ = dynamical viscosity;

l = length of the covering;

c = radial clearance;

e = eccentricity;

ρ = density of the fluid;

C_d = efflux coefficient;

A = area of the passing section.

Moreover, the circumferential opening $w \cong 2 \pi r$ ($r \gg c$) can be introduced and, expressing the length of the covering with $X0$ (varying with the spool position XS), RL can be expressed as:

$$RL = \frac{12 \mu X0}{w c^3 \left[1 + \frac{3}{2} \left(\frac{e}{c} \right)^2 \right]}$$

In this way, only the covering $X0$ and the area of the passing sections must be calculated.

In the calculation of $X0$, also lapping of the valve must be considered: $OSSV$ represents the lapping in the supply side and $ORSV$ the lapping in the return side. Moreover, this notation is valid also for the flow rate: QIS represents the flow rate from the supply to

chamber 1, $Q1R$ the flow rate from chamber 1 to the return and similarly for $Q2S$ and $Q2R$; $Q1L$ represents the net flow rate entering in chamber 1 and $Q2L$ the net flow rate exiting from chamber 2 (these are assumed always positive as shown in Figure 4.10). In general, every passing section will assume the characteristic of an annular orifice of length $X0$, that is nullified only when the displacement of the spool is opposite to the lapping and greater of it. Lengths of the four passing sections can be expressed as:

$$X01S = OSSV - XS$$

$$X01R = ORSV + XS$$

$$X02S = OSSV + XS$$

$$X02R = ORSV - XS$$

where $X01S$ represents the length of the passageway from supply to chamber 1, $X01R$ from chamber 1 to return, $X02S$ from supply to chamber 2, $X02R$ from chamber 2 to return.

Areas of the passing section, instead, will assume a minimum value of $w \cdot c$ (annulus) when the corresponding lapping is greater than spool displacement XS , but it will grow assuming the value of a truncated cone area:

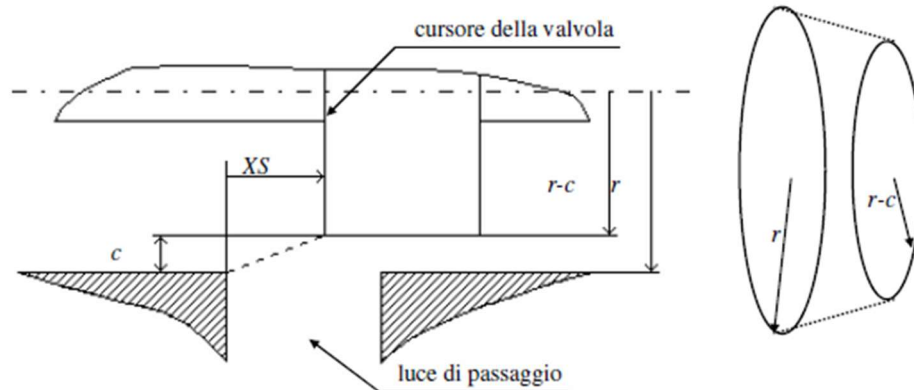


Figure 4.11: Section of passing section of the fluid when $XS > 0$ for zero-lapping valve (Dalla Vedova, 2007, p. 71).

Finally, it is possible to express areas of the passing sections as:

$$A1S = w\sqrt{c^2 + (XS - OSSV)^2}$$

$$A1R = w\sqrt{c^2 + (XS + ORSV)^2}$$

$$A2S = w\sqrt{c^2 + (XS + OSSV)^2}$$

$$A2R = w\sqrt{c^2 + (XS - ORSV)^2}$$

with the limitation to consider these areas equal to $w*c$ when XS is greater than the correspondent lapping.

Now it is possible to express the pressure drops across each passing area as functions of the flow rates as:

$$\Delta p1S = (p_s - p_1) = \Delta p1S_{lin} + \Delta p1S_{quadr} = RL1S Q1S + RQ1S Q1S |Q1S|$$

$$\Delta p1R = (p_1 - p_R) = \Delta p1R_{lin} + \Delta p1R_{quadr} = RL1R Q1R + RQ1R Q1R |Q1R|$$

$$\Delta p2S = (p_s - p_2) = \Delta p2S_{lin} + \Delta p2S_{quadr} = RL2S Q2S + RQ2S Q2S |Q2S|$$

$$\Delta p2R = (p_2 - p_R) = \Delta p2R_{lin} + \Delta p2R_{quadr} = RL2R Q2R + RQ2R Q2R |Q2R|$$

From these equations, it is possible to obtain flow rates through each passing area as:

$$Q1S = \frac{-RL1S + \sqrt{RL1S^2 + 4 RQ1S |p_s - p_1|}}{2 RQ1S} \text{SIGN}(p_s - p_1)$$

$$Q1R = \frac{-RL1R + \sqrt{RL1R^2 + 4 RQ1R |p_1 - p_R|}}{2 RQ1R} \text{SIGN}(p_1 - p_R)$$

$$Q2S = \frac{-RL2S + \sqrt{RL2S^2 + 4 RQ2S |p_s - p_2|}}{2 RQ2S} \text{SIGN}(p_s - p_2)$$

$$Q2R = \frac{-RL2R + \sqrt{RL2R^2 + 4 RQ2R |p_2 - p_R|}}{2 RQ2R} \text{SIGN}(p_2 - p_R)$$

As it can be noticed, only the value of the pressure drop across each passing area influences the value of the flow rate and this explains the presence of the absolute value, while its sign influences only the verse of the flow rate and this explains the multiplicative term $SIGN(\Delta p)$. Once each flow rate is calculated, it is possible to obtain the useful flow rates to the actuator as algebraic sum of the flow rates through the respective passing areas as:

$$Q1L = Q1S - Q1R$$

$$Q2L = Q2R - Q2S$$

The model obtained from this treatment is shown below:

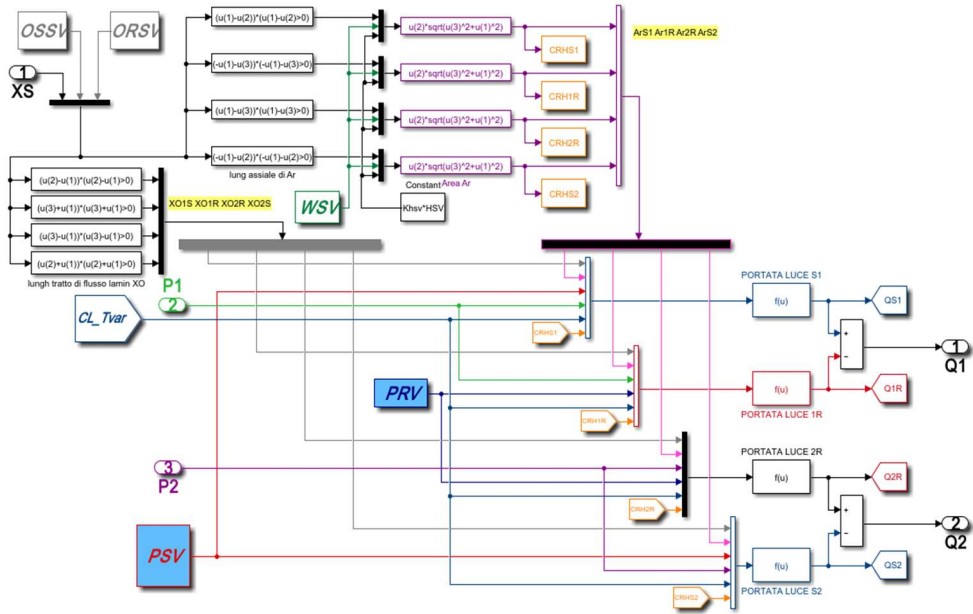


Figure 4.12: Simulink model of the subsystem “Fluid dynamic model”.

Moreover, it has been inserted another coefficient K_{hsv} that multiplies the nominal clearance HSV to simulate its degrading condition in time.

As it can be observed in Figure 4.12, it is present another block called “*CRH + abbreviation of each section name*”: this subsystem permits to calculate the actual value of the efflux coefficient C_d as multiplication of two terms: the first one (C_{d0}), expressed through an empirical relation, is a function of the Reynolds number, which considers the actual values of the fluid density and cinematic viscosity through look-up tables and represents the nominal efflux coefficient, while the second one (C') represents the correction of the first coefficient, calculated from the variable geometry of the passing area. The scheme is reported below:

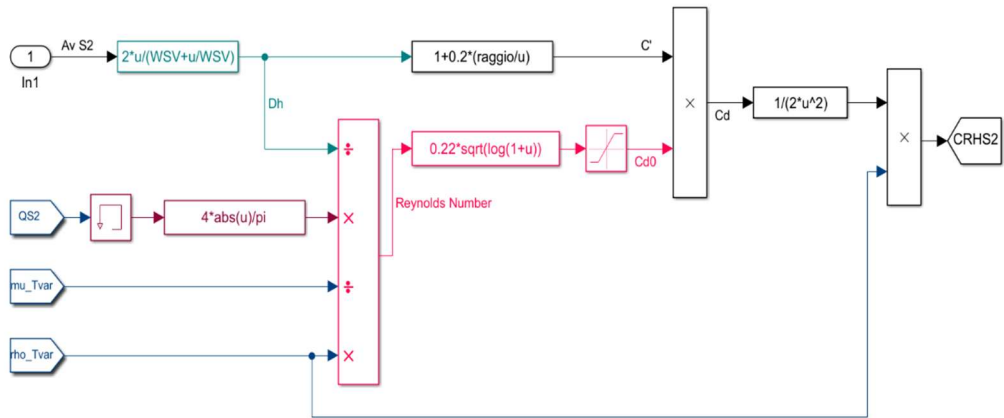


Figure 4.13: Scheme of the subsystem CRH, relative to the passing area S2.

The mathematical model presented above permits to obtain the characteristic curves of the flow rate, trend of the regulated flows as function of the spool position X_S and the pressures P_1 and P_2 , but it is not possible to directly obtain the characteristic curves of pressures (at given flow rate). To solve this problem, a calculation routine has been implemented where, simulating effects of the fluid compressibility in the circuit after the servovalve, it is possible to calculate the temporal derivative of regulated pressures on the two outlet of the valve as functions of the net regulated flow rates: they can be written as:

$$P_1(t + DT) = P_1(t) + [Q_{1L}(t) - Q_M(t)] * \frac{Bet}{Vol} * DT$$

$$P_2(t + DT) = P_2(t) + [Q_M(t) - Q_{2L}(t)] * \frac{Bet}{Vol} * DT$$

where P_1 and P_2 represent the regulated absolute pressures in the outlet valve, Q_{1L} and Q_{2L} the flow rates disposed of by the actuator, DT the sample time, Bet the compressibility coefficient of the fluid, Vol the volume of the two hydraulic capacity and Q_M the total absorbed flow rate from the actuator that can be expressed as function of possible leakage as:

$$Q_M(t) = A_J * DX_J(t) + Clk * [P_1(t) - P_2(t)]$$

Further, these equations have been modified to simulate accurately cavitation phenomena in the fluid that can influence very much the dynamic behaviour of the system as:

$$P1T(t + DT) = P1T(t) + [Q1L(t) - QM(t)] * \frac{Bet}{Vol} * DT$$

$$P1(t + DT) = \text{MAX}[PVap, P1T(t + DT)]$$

$$P2T(t + DT) = P2T(t) + [QM(t) - Q2L(t)] * \frac{Bet}{Vol} * DT$$

$$P2(t + DT) = \text{MAX}[PVap, P2T(t + DT)]$$

$P1T$ and $P2T$ represent two auxiliar terms that permit to consider possible formation of vapor bubbles: it is possible to have memory of eventual negative picks of pressure (even if these picks are fictitious) that highlight vapor bubble formation in the fluid. If this routine were not considered, calculation would lose memory of oil vapor volume, formed in cavitation, that first must come back to the liquid state to let to pressure grow over the value $PVap$. From a physic view of the phenomena, this is equivalent to not consider vapor bubble in the fluid and, after the cavitation condition, the pressure would grow positively, while, with these assumptions, the cavitation effect is progressively reduced, letting the real pressure grow only when the theoretical pressure is greater than $PVap$.

The dynamical system expresses the calculated pressures as functions of the corresponding net flow rates through fluid capacities. It is a first order model so, reducing the capacities, the constant time τ is proportionally reduced: in particular, if the capacities were too small, the model would be unstable because of incompatibility between the constant time τ and the sample time DT .

The derived model of the pipe capacities is shown below:

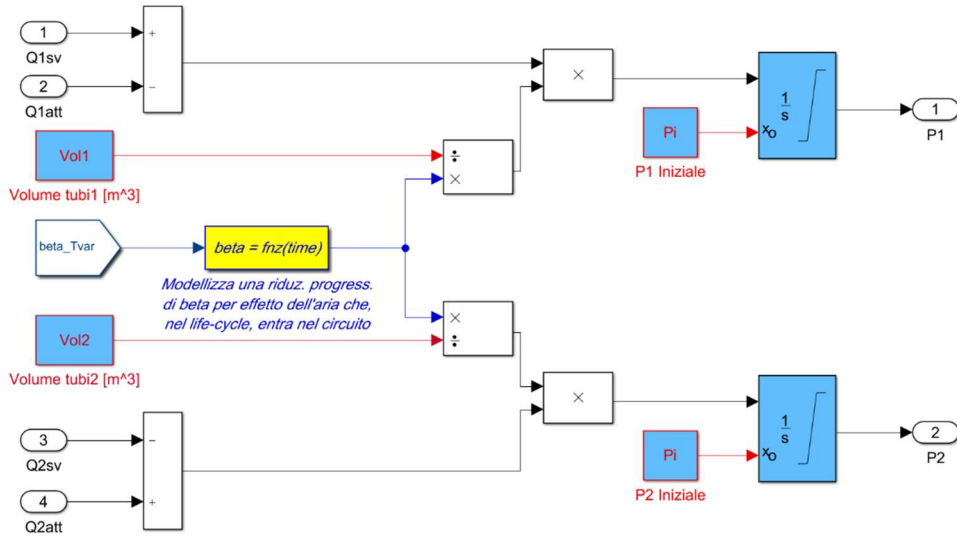


Figure 4.14: Pipe capacity model.

In this way, the complete fluid dynamic model is shown in Figure 4.15:

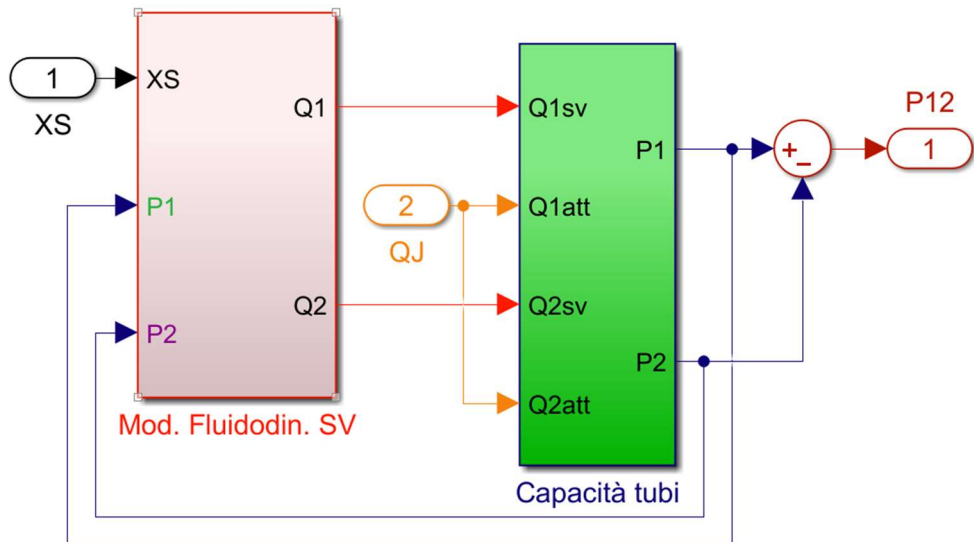


Figure 4.15: Complete fluid dynamic model.

The characteristic curves, used as a reference for the design of the Low-Fidelity fluid-dynamic model, have been obtained from this model. In particular, the characteristic curves $P12-XS$, shown in Figure 4.16, have been obtained simulating, point by point, from the whole fluid-dynamic model, imposing as inputs XS (from -0.6 mm to 0.6 mm) at different values of QJ (equal to -6 m³/s, -3 m³/s, 0 m³/s, 3 m³/s, 6 m³/s); the characteristic curves $QJ-XS$, shown in Figure 4.17, instead, have been obtained from the first part of the fluid-dynamic model, imposing as inputs the same values of XS as before and $P1$ and $P2$ so that, imposing $P1$, their sum is maintained constant and equal to 22 MPa (that is also the sum of the supply and return pressures).

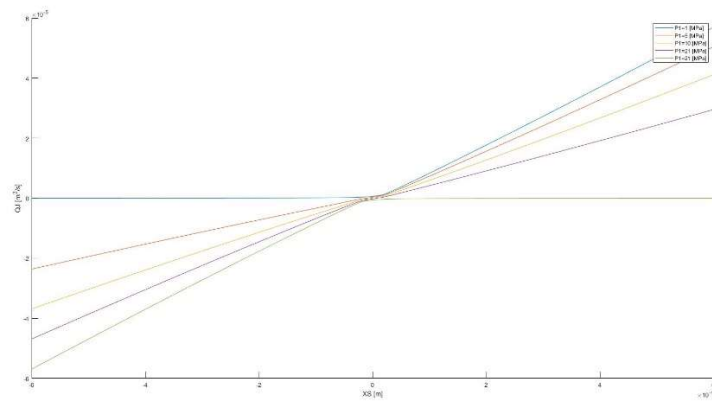


Figure 4.16: Characteristic curves $P12-XS$.

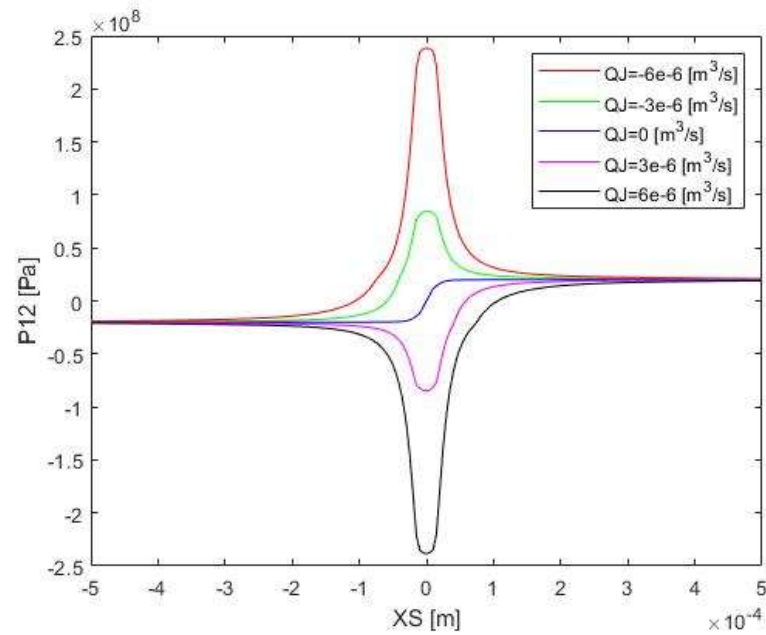


Figure 4.17: Characteristic curves $QJ-XS$.

4.1.4 Mechanical model of the jack

The last block analysed is mechanical model of the jack. The differential pressure $P12$ from the fluid-dynamic model is multiplied by the equivalent jack surface, obtaining the force acting on the jack. This represents the input for the jack's model in Figure 4.18:

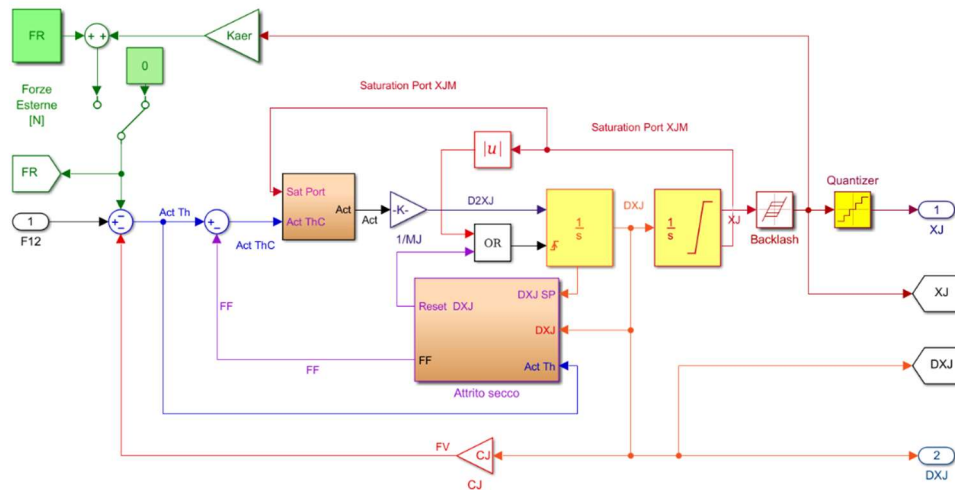


Figure 4.18: Model of the jack.

As it can be seen, the structure is very similar to the model of the first stage of the servovalve. The actual force is calculated subtracting the dissipative forces to the input: the viscous force, obtained multiplying the velocity of the jack by the viscosity coefficient CJ and, through a manual switch, the sum of possible external and aerodynamic forces; this last one is calculated multiplying the position of the jack by the aerodynamic coefficient $Kaer$, that simulates the opposition of aerodynamic to displacement of mobile surfaces. The theoretical net force is then passed to the Borello's friction model, that also receives the velocity of the jack from the integrator and the value of its saturation port: the outputs are the real friction force and the reset value of the first integrator. Again, a saturation block is present, to nullify the velocity of the jack when it reaches upper or lower limit of displacement. Then, the actual net force is divided by the mass of the jack to obtain its acceleration and, through two successive integrations, velocity and displacement of the jack are obtained. Moreover, a backlash block is present after the second integrator in the closed loop; it is used to simulate any possible backlash due to usury in the kinematic chain that joins the jack to mobile surfaces. It has been inserted in the closed loop because it has been assumed the sensor to be installed in the mobile surface and, for this reason, subjected to possible backlash. Finally, a quantizer block is inserted before the output XJ to consider discretization problem due to digital acquisition.

physical phenomena: this is possible due to the fact Simulink can impose concurrently conditions both in time and frequency domain. The transfer function is expressed as:

$$\frac{XF}{T} = \frac{1}{KFm + KSFm} \frac{1}{\frac{1}{SNF^2} s^2 + 2 \frac{ZF}{SNF} s + 1}$$

where the DC gain $\frac{1}{KFm + KSFm}$ represents the equivalent stiffness of the flapper, KFm is the translational stiffness of the spring in the first stage, $KSFm$ the translational stiffness of the feedback spring, SNF the natural frequency of the first stage and ZF its dimensionless dumping factor.

Another important difference is represented from the friction: to differentiate the Low-Fidelity model from the High-Fidelity, Karnopp's friction model is used in the monitor, less accurate but simpler.

The main difference between the models is represented, instead, from the fluid dynamical model that will be analysed in the next chapter, while the mechanical model of the jack is almost identical.

5 DEVELOPMENT OF MONITORING FLUID-DYNAMIC MODEL

Many different fluid-dynamic models have been developed to match the High-Fidelity performances, more accurate respect to the previous. Here, they are presented in order of increasing complexity.

5.1 SIMPLE LINEARIZED FLUID-DYNAMIC MODEL

According to the linearization approach described above, it is possible to assume that, as first approximation, the function $P12(XS)$ for a generic flow rate QJ is obtainable from that curve for null QJ only translating it, in parallel, for a quantity proportional with QJ itself; it is possible to assume the same approach for the function $QJ(XS)$ depending on $P12$.

This means the principle of superposition is valid for XS , seen as sum of two contribution: the first producing differential pressure (XS_p) and the second flow rate (XS_Q).

$$XS = XS_p + XS_Q = \frac{P12}{GP} + \frac{QJ}{GQ}$$

From this equation, it is possible to obtain two other relations to suit model requirements:

$$P12 = GP \left(XS - \frac{QJ}{GQ} \right)$$

$$QJ = GQ \left(XS - \frac{P12}{GP} \right)$$

The first relation is used when the fluid-dynamic model is thought to obtain the differential pressure $P12$ from spool position XS and flow rate QJ (it is a typical case in models that do not consider possible hydraulic capacities between the valve and the actuator); the second one is used when the fluid-dynamic model is thought to obtain flow rates QJ for each value of position spool XS and differential pressure $P12$ (it is a typical case in models that consider hydraulic capacities between the valve and the actuator).

From the first relation, a first linearized model has been deduced for control application or first approximation analysis:

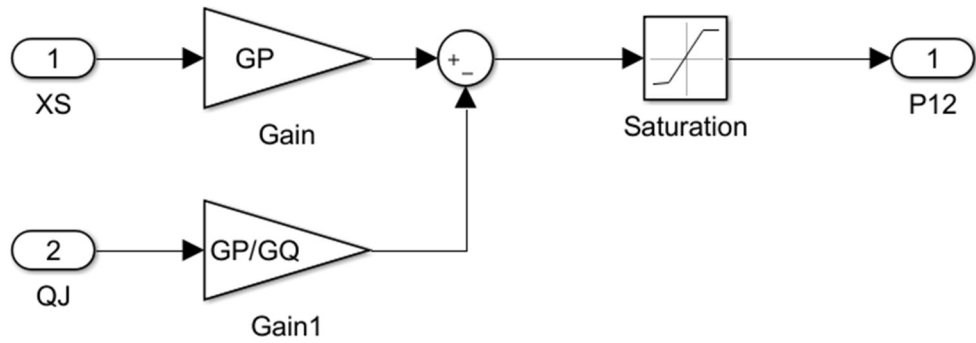


Figure 5.1: Simulink linearized fluid-dynamic model.

As it can be seen in Figure 5.1, a saturation block is present before the output: in this way, the differential pressure $P12$ is limited between the values $+PSR$ and $-PSR$, the supply-return pressure.

In figure 5.2, characteristic curves $P12$ - XS can be observed.

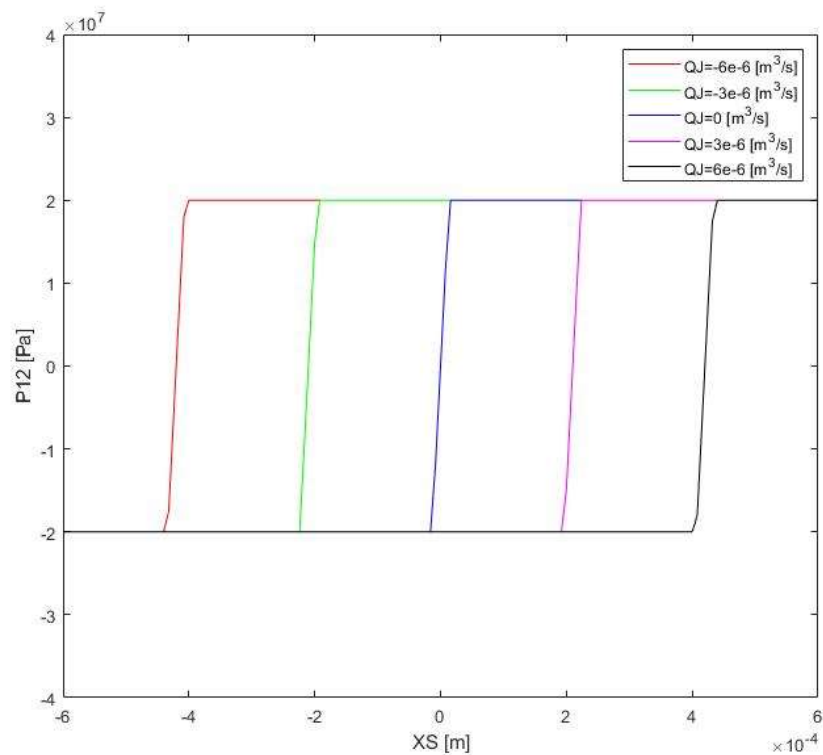


Figure 5.2: Characteristic curves $P12$ - XS of the first linearized model.

5.2 SECOND SIMPLIFIED MODEL

To obtain a more faithful model, able to consider saturation of $P12$ for greater values of XS , the linearized model must be set aside, introducing instead the variable pressure gain GPS .

It is possible to obtain the differential pressure commanded at null flow rate from the spool position XS with the relation:

$$P12P = GP \cdot XS \quad \text{with} \quad -PSR \leq P12P \leq +PSR$$

where PSR is the provided differential pressure supply-return: the maximum values of $P12$ obtained from the simulations are similar to the real and to the High-Fidelity ones. However, an uncompleted consideration of the saturation effect can lead to an underestimation of developed flow rates, so to an underestimation of the actuation velocities. It is possible to calculate the available $P12$ from the commanded differential pressure $P12P$, subtracting the differential pressure $P12Q$, lost because of the flow rate QJ . A modified value of the pressure gain GPS is introduced, related to the corresponding pressure gain GP and variable with the spool position XS , defined as:

$$GPS = \frac{P12P}{XS}$$

In non-saturation condition of the pressure, it will be equal to GP , while in the other case it will be equal to PSR/XS . In this way, considering the main branch and the flow rate feedback branch, it is possible to model quite well the pressure $P12$ peaks at given flow rate QJ , typical of small values of XS and, at the same time, to reduce the pressure drops at greater values of XS . The regulated pressure $P12$ is expressed as:

$$P12 = P12P - \frac{GPS}{GQ} \cdot QJ$$

The main quality of this formulation is the capability to model the pressure $P12$ peaks for small value of XS with great values of flow rate QJ : it is the typical case when a rapid closure of the spool is commanded while the motor is still moving, causing the water hammer.

The differential pressure lost due to the flow rate is:

$$P12Q = QJ \cdot \frac{GPS}{GQ}$$

This is not the only pressure lost, in fact another flow rate does not work due to leakage presence: as first approximation, it can be considered proportional to the pressure $P12$, according to the leakage coefficient Clk :

$$P12Lk = P12 \cdot Clk \cdot \frac{GPS}{GQ}$$

In Figure 5.3 below, the relative block scheme is reported:

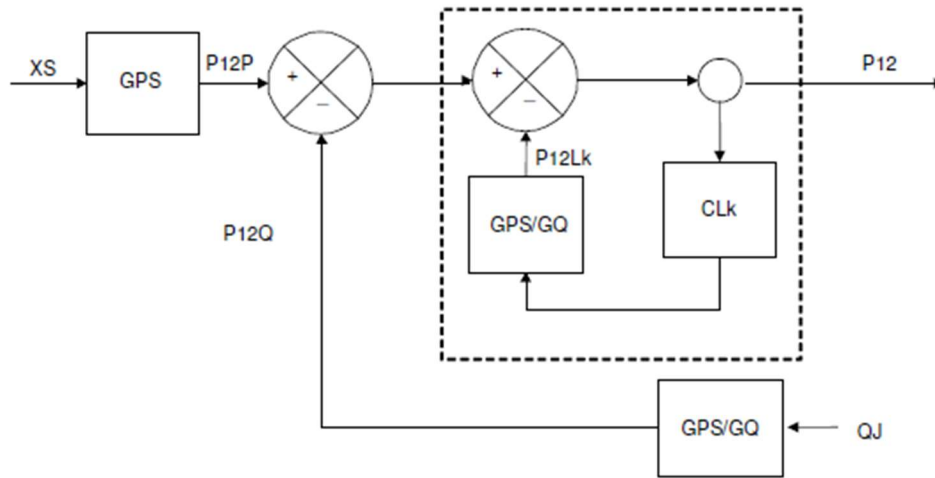


Figure 5.3: Leakage loop representation (Dalla Vedova, 2007, p. 95).

To let simulations work correctly, a suitable integration interval DT must be chosen, smaller than the smallest time constant of the system, but, in this case, if the feedback branch dynamic is instantaneous, the only suitable value for the integration time is the null value (in this way it is not possible to apply numeric integration).

To avoid numerical instability due to the instantaneous dynamic of the leakage loop, it is necessary to analytically solve it, substituting the branch with a single block with equivalent transfer function:

$$\frac{\text{output}}{\text{input}} = \frac{1}{1 + \text{Clk} \cdot \frac{\text{GPS}}{\text{GQ}}}$$

To have a model that can consider possible variations of the supply differential pressure, it is assumed that also the flow rate gain GQ and the pressure gain GP are linearly dependant from the supply-return differential pressure:

Two quantities, invariant with PSR are introduced:

$$XSS = \frac{PSR}{GP}$$

$$GPQ = \frac{GP}{GQ}$$

with XSS saturation position of the spool and GPQ ratio of pressure gain to flow rate gain.

From these, it is possible to obtain:

$$GP = \frac{PSR}{XSS} \quad \text{and} \quad GPS = \frac{PSR}{\text{MAX}(|XS|, XSS)}$$

Now, the relation GPS/GQ is expressed as:

$$\begin{aligned} \frac{GPS}{GQ} &= \frac{PSR}{\text{MAX}(|XS|, XSS)} \cdot \frac{GPQ}{GP} = \frac{PSR}{\text{MAX}(|XS|, XSS)} \cdot GPQ \cdot \frac{XSS}{PSR} \\ &= GPQ \cdot \frac{XSS}{\text{MAX}(|XS|, XSS)} \end{aligned}$$

Finally, considering the block scheme in Figure 4.3, the transfer function below is obtained:

$$P12 = \frac{PSR \cdot XS - GPQ \cdot XSS \cdot QJ}{\text{MAX}(|XS|, XSS) + GPQ \cdot XSS \cdot Clk}$$

From this transfer function, the sequent Simulink scheme is obtained:

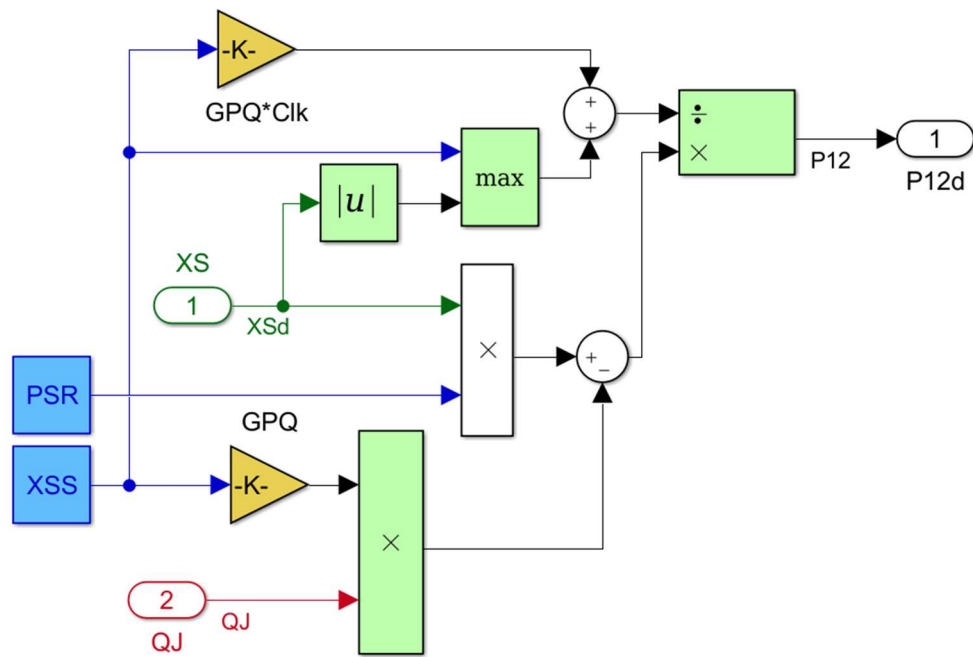


Figure 5.4: Simulink evolved fluid-dynamic model.

Below the associated characteristic curves $P12-XS$ are shown:

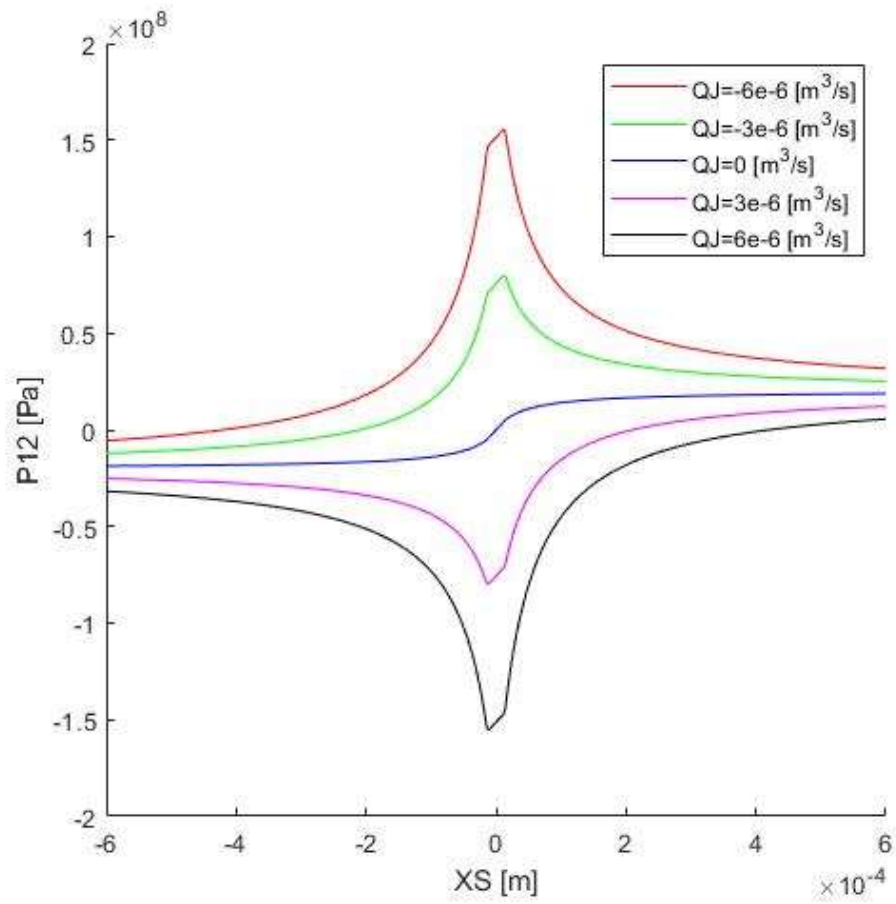


Figure 5.5: Characteristic curves $P12-XS$ of the evolved fluid-dynamic model.

5.3 DEVELOPED FLUID-DYNAMIC MODEL

This new fluid-dynamic model has been developed in collaboration with Ing. Berri.

This new model uses a different definition of the commanded differential pressure: a mathematical function that better remarks the behaviour of the differential pressure at null flow rate is used, expressed as:

$$P_{12P} = PSR \cdot \tanh\left(\frac{XS}{XSS}\right)$$

In this way, the P_{12P} is limited between $-PSR$ and $+PSR$, depending on the spool position XS normalized respect to the saturation position XSS . This normalization is used also in the definition of the variable pressure gain:

$$GPS = GP \cdot \left(\frac{XSS}{XS}\right)^2$$

With this new definition, the pressure lost because of flow rate can be defined as in the previous model:

$$P_{12Q} = QJ \cdot \frac{GPS}{GQ} = QJ \cdot \frac{GP}{GQ} \cdot \left(\frac{XSS}{XS}\right)^2$$

So, the available pressure is obtained as:

$$P_{12} = PSR \cdot \tanh\left(\frac{XS}{XSS}\right) - QJ \cdot \frac{GP}{GQ} \cdot \left(\frac{XSS}{XS}\right)^2$$

Through this new equation, it is possible to model in a better way the P_{12} peaks at small values of XS and greater values QJ . However, not all the flow rate is available in the passageway, in fact a small part is lost due to leakage: taking the previous definition, the pressure lost due to leakage is:

$$P_{12Lk} = P_{12Q} \cdot Clk \cdot \frac{GPS}{GQ} = P_{12Q} \cdot Clk \cdot \frac{GP}{GQ} \cdot \left(\frac{XSS}{XS}\right)^2$$

The resulting control scheme is shown below:

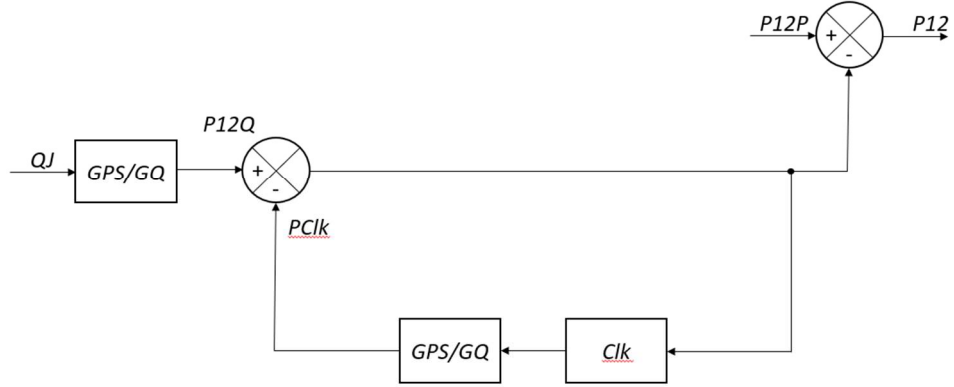


Figure 5.6: Control scheme relative to P12 dissipation.

As in the previous model description, numerical instability must be avoided, analytically solving the leakage closed loop and obtaining, after some mathematical passages, the final transfer function of the model:

$$P12 = PSR \cdot \tanh\left(\frac{XS}{XSS}\right) - QJ \cdot \frac{1}{\left(\frac{XS}{XSS}\right)^2 \frac{GQ}{GP} + Clk}$$

To best fit the High-Fidelity characteristic curves, a quadratic dependence of the flow rate losses with respect to the flow rate itself has been added, calibrating it respect to a fixed value:

$$P12 = PSR \cdot \tanh\left(\frac{XS}{XSS}\right) - QJ \cdot \frac{|QJ|}{4.5 \cdot 10^{-6}} \cdot \frac{1}{\left(\frac{XS}{XSS}\right)^2 \frac{GQ}{GP} + Clk}$$

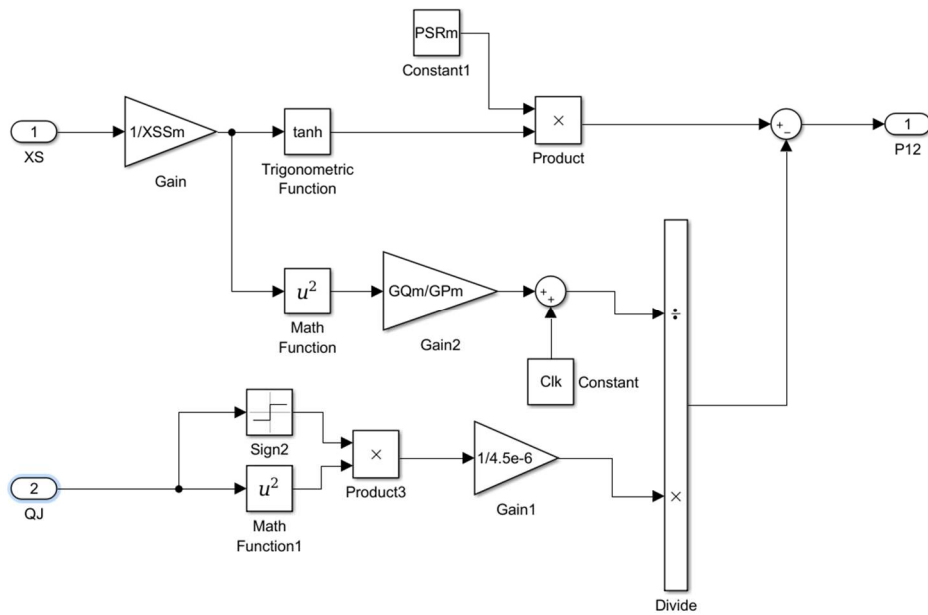


Figure 5.7: Simulink model of the new fluid-dynamic model (first version).

It has been possible to obtain the best fit value of GP from the characteristic curves $P12-XS$ for $QJ=0$, while the best values of Clk and GQ have been obtained by a trial-and-error procedure to find an acceptable compromise between the fit of the characteristic curves $P12-XS$ and $QJ-XS$. In this way, the sequent curves have been obtained:

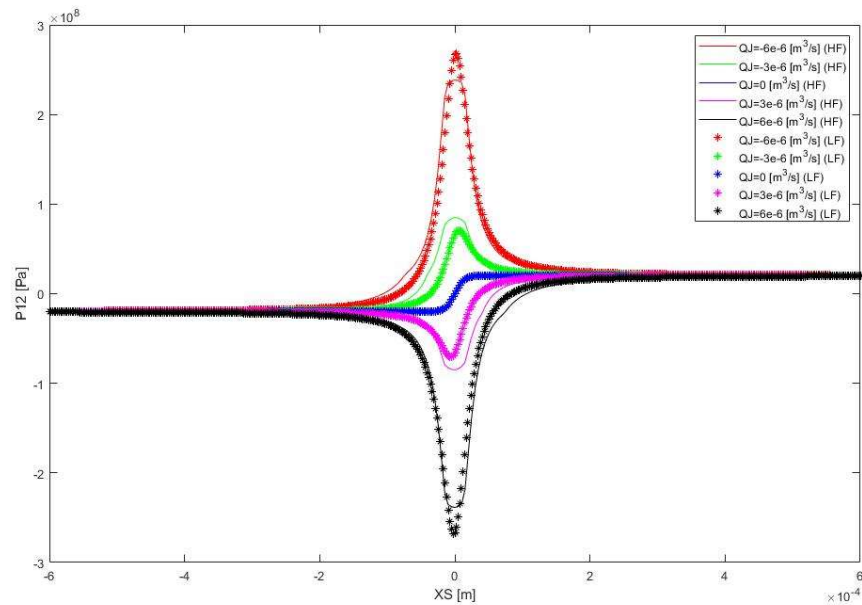


Figure 5.8: Comparison of the High-Fidelity and Low-Fidelity models characteristic curves $P12-XS$.

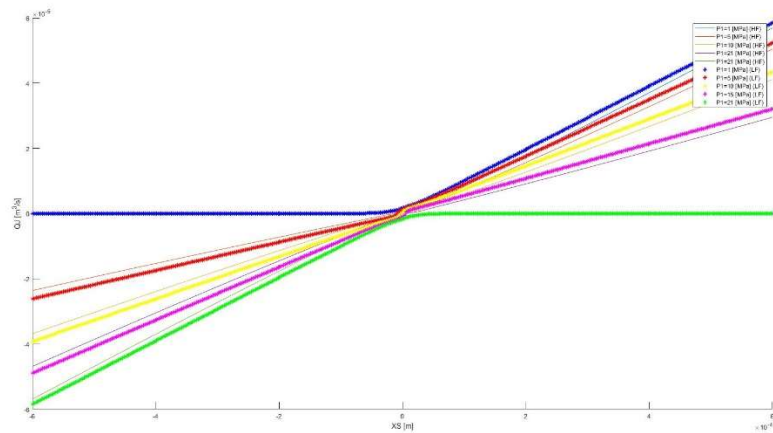


Figure 5.9 Comparison of the High-Fidelity and Low-Fidelity models characteristic curves QJ - XS .

However, even if this model should be able to reproduce more accurately the $PI2$ peaks, it was not possible to find a working point that remarks the time response of the High-Fidelity model in an acceptable way, because of its instant dynamic.

A function that introduces a time dependant behaviour (in this case a first order dynamic response) have been inserted before the output: a map of the time constants, typical of every value of $PI2$ at given XS and QJ , have been obtained from Simulink simulations of the High-Fidelity model for a time sufficient to let all quantities reach the steady state (because of the integrator in the pipe capacity model).

The sequent curves have been obtained, with a tolerance of 5000 Pa due to fast dynamic of the valve at great values of XS .

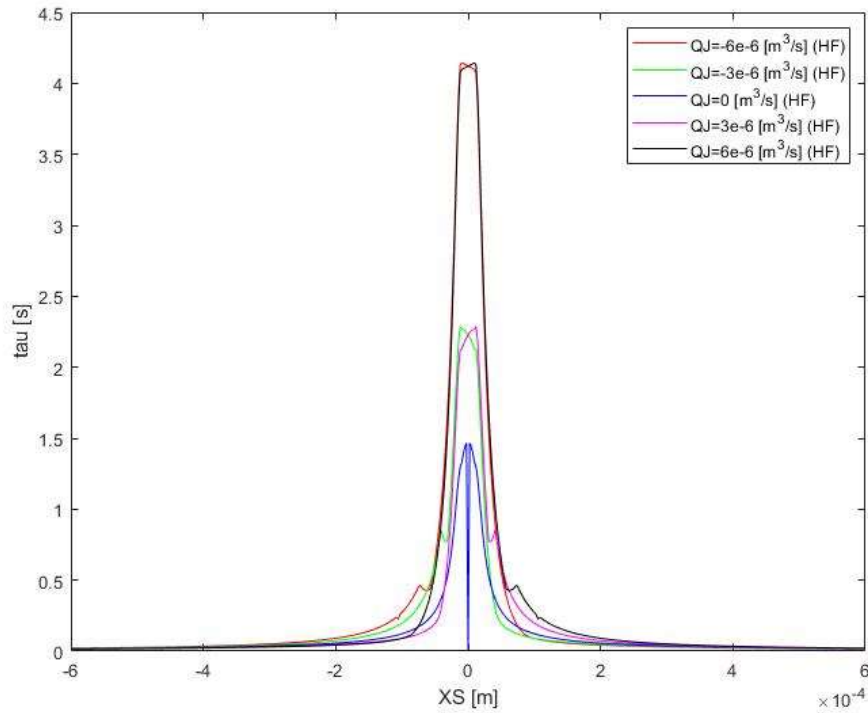


Figure 5.10: Time constants map of the HF model.

As it can be seen, the curves with same absolute value of flow rate are symmetrical respect to the y axis and very similar for higher values of QJ ; decreasing QJ , they are still symmetrical but less similar. Moreover, a descendant peak can be observed at $XS=0$ and $QJ=0$, where the time constant is equal to zero: this is due the fact that, for null value of QJ and XS , the response of the system is also zero. From this map, it can be deduced that two different contributions are present in the dynamic behaviour of the system: the first is related to the spool position XS , that gives this bell-shaped behaviour; the second is given, with some simplifications, from the absolute value of the flow rate QJ and it increases the value of the peak of the bell.

To model the bell-shaped behaviour, a rational function has been adopted, in the form

$$y = \frac{a}{b \cdot \left(\frac{XS}{XSS}\right)^2 + c}$$

with $a=5.6$, $b=1.2$ and $c=4$. The approximated curve is shown in Figure 5.10.

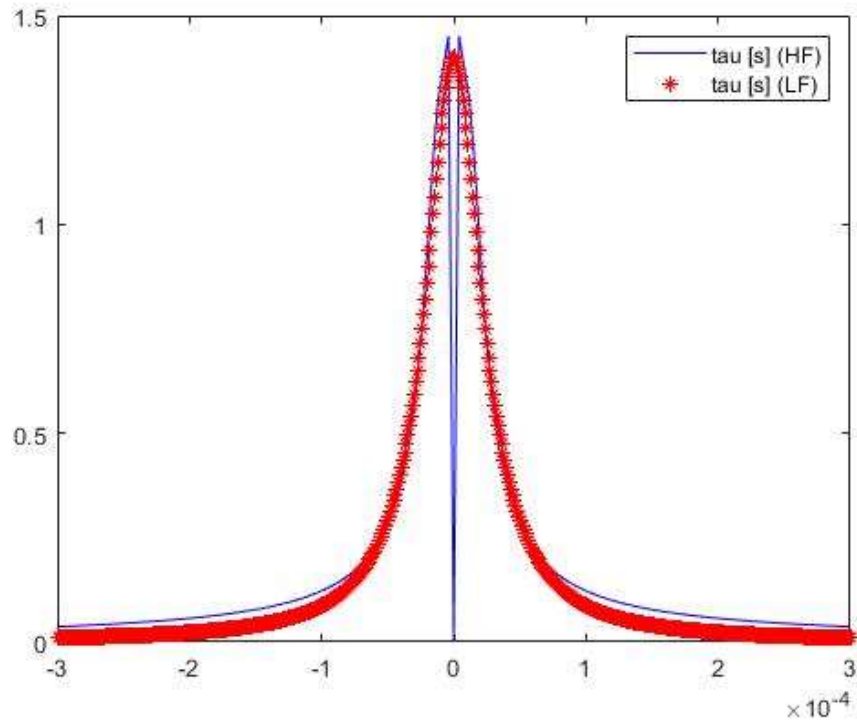


Figure 5.11: Approximation of the bell-shaped behaviour of time constants at $QJ=0$.

If time constants determined by only XS are considered as a reference, the contribution given by the absolute value of QJ can be assumed as a multiplicative factor. For this reason, peaks of the bell at $|QJ| \neq 0$ have been analysed, looking for an approximating polynomial function; in this way, it has been observed that the contribution of QJ has a quite linear behaviour, so it can be approximated as

$$y = a|x| + b ,$$

where $a=0.5/(3 \cdot 10^{-6})$ and $b=1$ have been chosen to best interpolate the bells peaks. Results of interpolation are shown below:

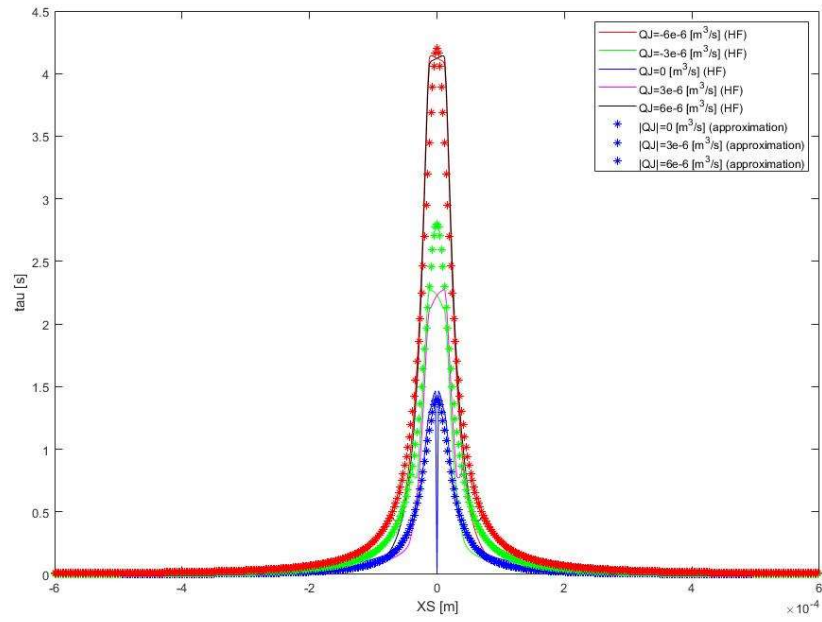


Figure 5.12: Approximation of tau from the High-Fidelity model.

Once the map of the HF time constants has been replicated, a first order dynamic has been introduced in the model before the output. The final fluid-dynamic model is shown in Figure 5.12:

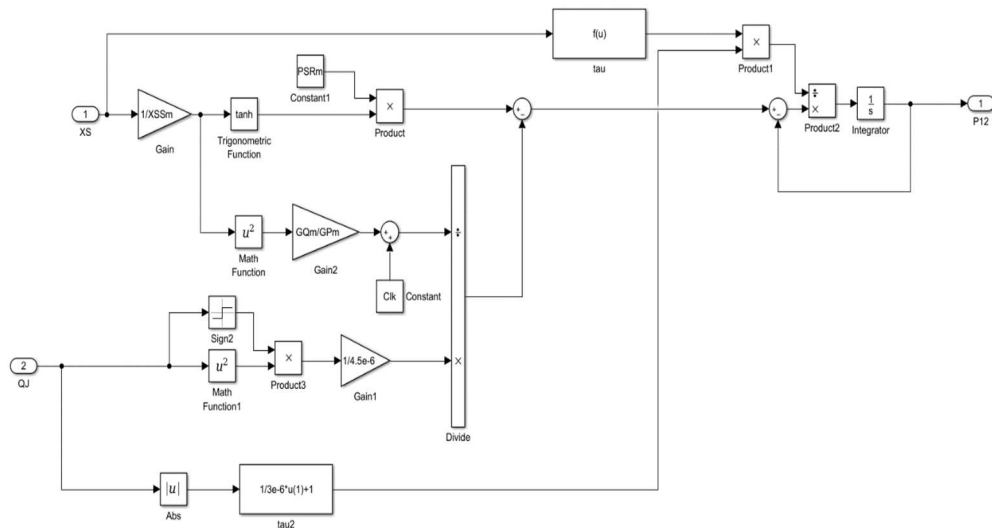


Figure 5.13: New developed fluid-dynamic model.

Due to the complexity of $PI2$ peaks modelling and approximations, it has been impossible to perfectly remark the HF time response for all kind and amplitude of input, but it has been calibrated for great values of flow rate, having almost the same behaviour. Time responses of both models are shown below for 0.1 m step amplitude, 0.1 m/s ramp slope and 0.1 m sine semi-amplitude reference signals.

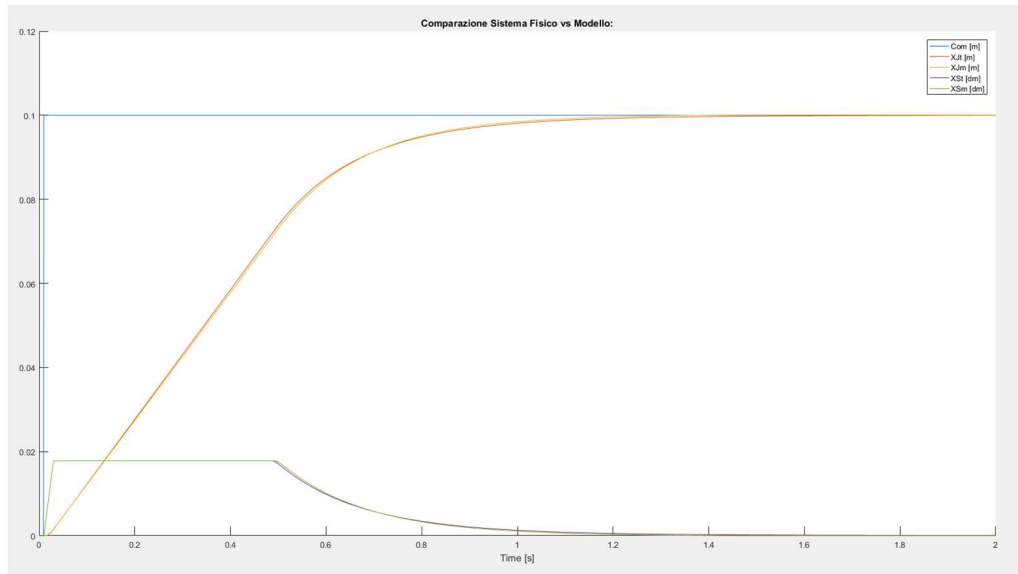


Figure 5.14: Time response of HF and LF models for step with amplitude of 0.1 m.

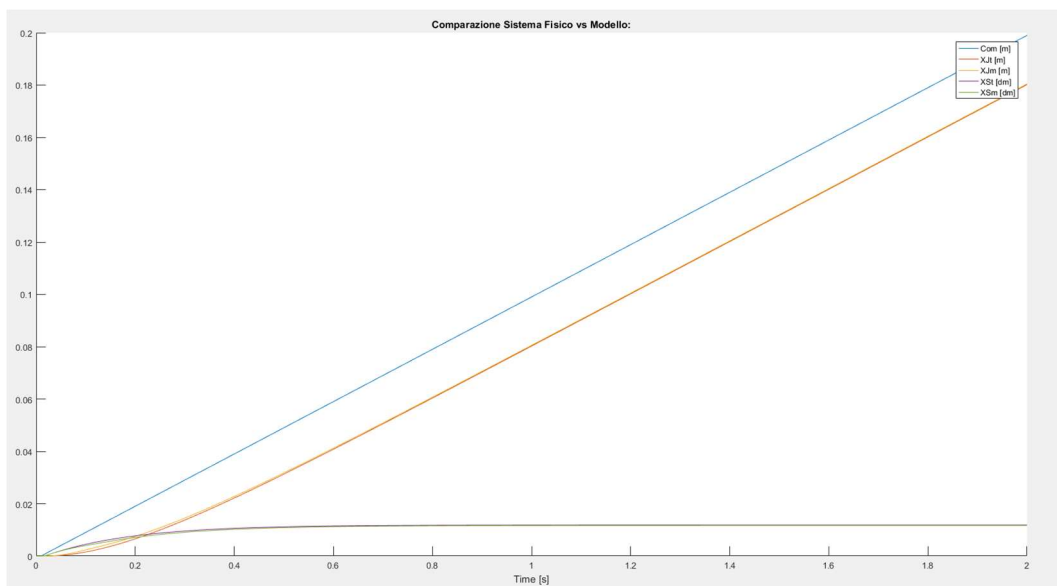


Figure 5.15: Time response of HF and LF models for ramp with slope of 0.1 m/s.

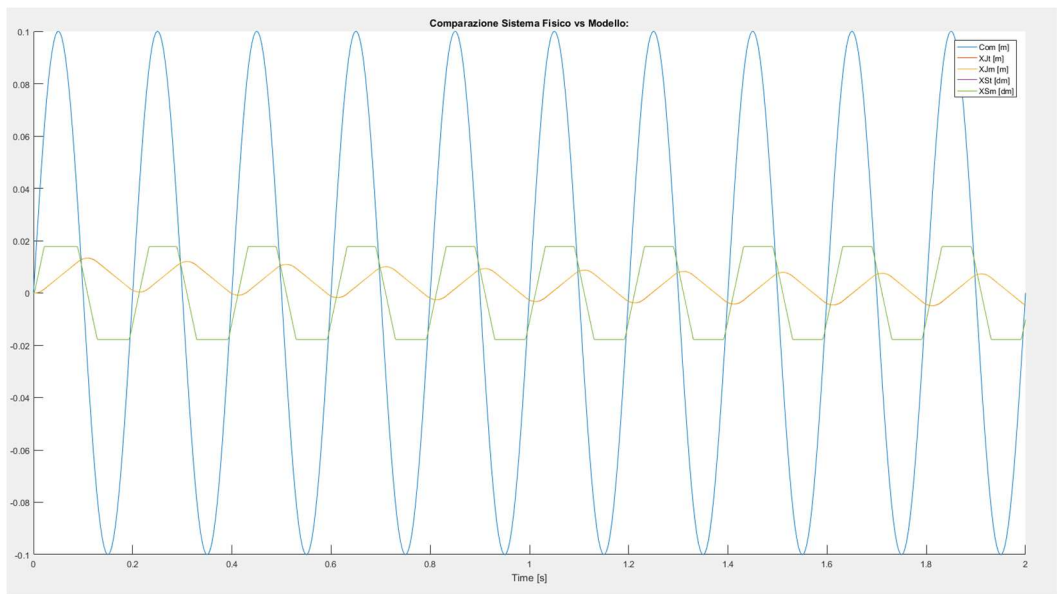


Figure 5.16: Time response of HF and LF models for sine with semi amplitude of 0.1 m.

6 FAULT ANALYSIS

In this chapter, system responses under different conditions will be studied. In the previous chapter, the response of the system in perfect condition is shown, while in presence of different failures it may change, even compromising its performances.

Two different failures will be analysed: demagnetization of the torque motor and increasing static friction on the jack. At first, these failures will be simulated separately with different inputs and, after, characteristic physical quantities that clearly show the presence of each failure will be identified. Finally, both failures will be combined. The difficult part of this analysis is the identification of a quantity that unequivocally shows the failure because different failures can influence the same aspect of the dynamic response.

Each failure will be analysed for reasonable values of fault since a high value will never be reached, thanks to the preventive maintenance.

6.1 DEMAGNETIZATION OF THE TORQUE MOTOR

In this paragraph, the demagnetization of the torque motor will be analysed. This fault is simulated varying the gain of the torque motor, multiplying it by the coefficient ($1-KGM$), with KGM sensibility factor of the torque motor that ranges from 0 (nominal condition) to 1 (completely demagnetized). KGM has been assumed reasonably from 0 to 0.4, so from its total capacity to 60%.

6.1.1 Response to a step input signal

Due to the operational range of the model, calibrated for high values of flow rate, a step command of 0.1 m amplitude is imposed. Below, behaviours of current absorbed by the torque motor (Cor), spool position (XS), differential pressure across the servovalve ($P12$), position and velocity of the jack (XJ and DXJ) are reported.

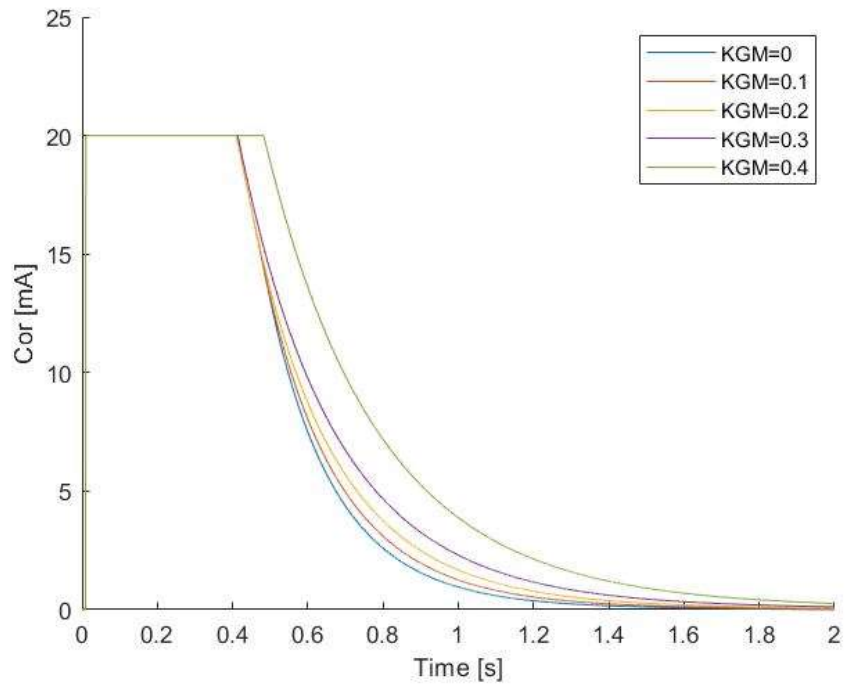


Figure 6.1: Cor response to a step input signal.

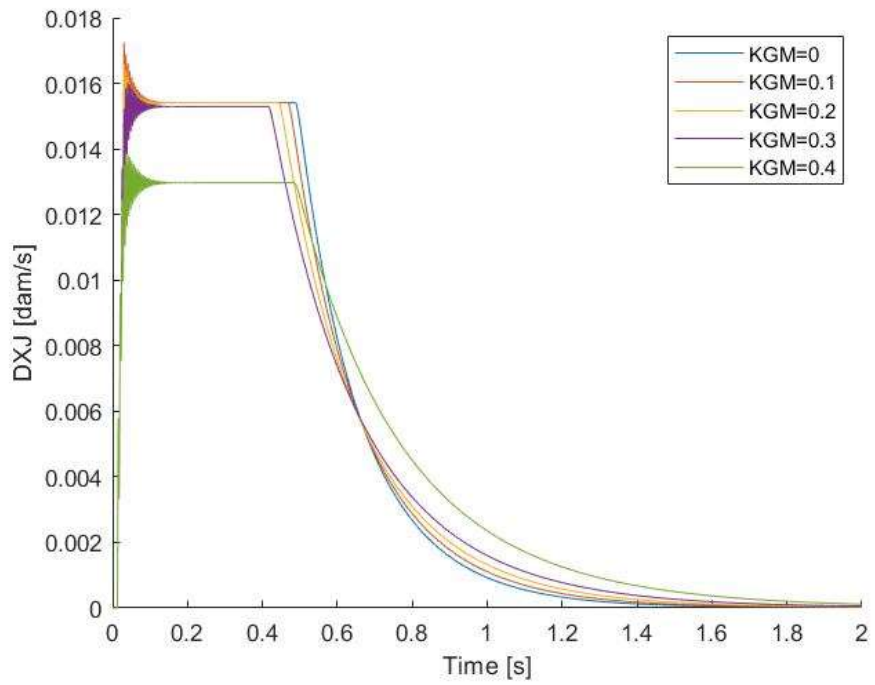


Figure 6.2: DXJ response to a step input signal.

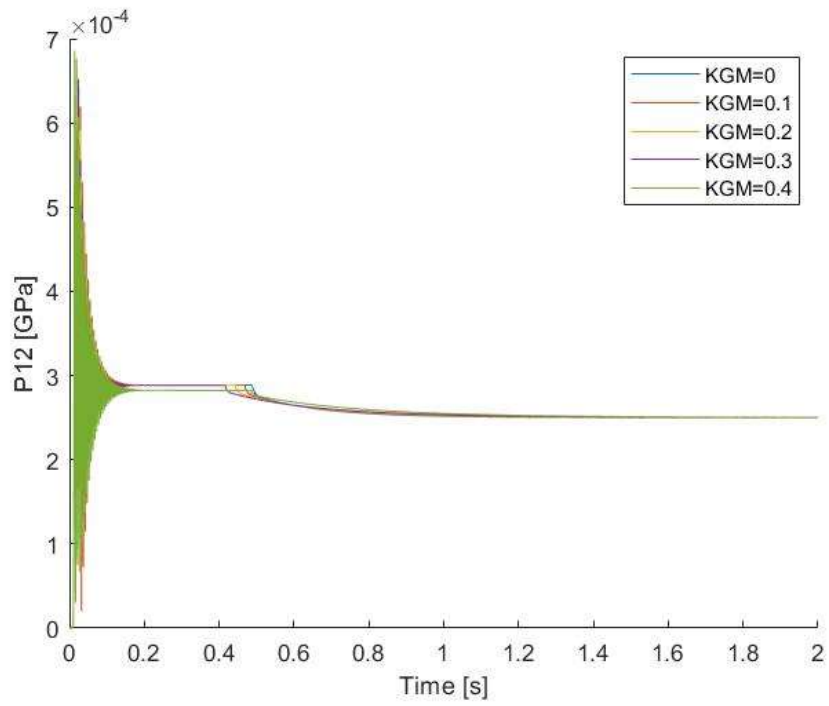


Figure 6.3: P12 response to a step input signal.

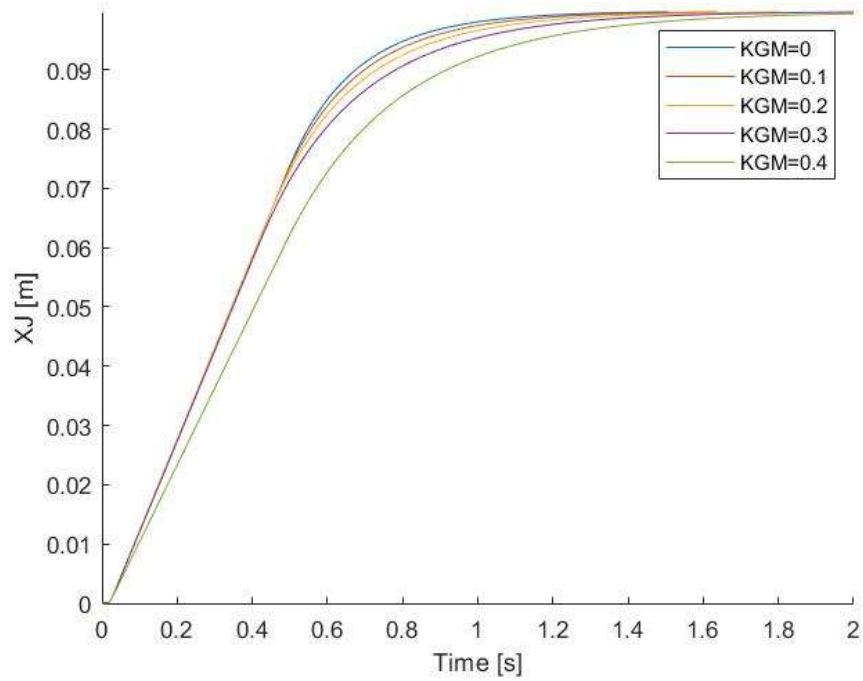


Figure 6.4: XJ response to a step input signal.

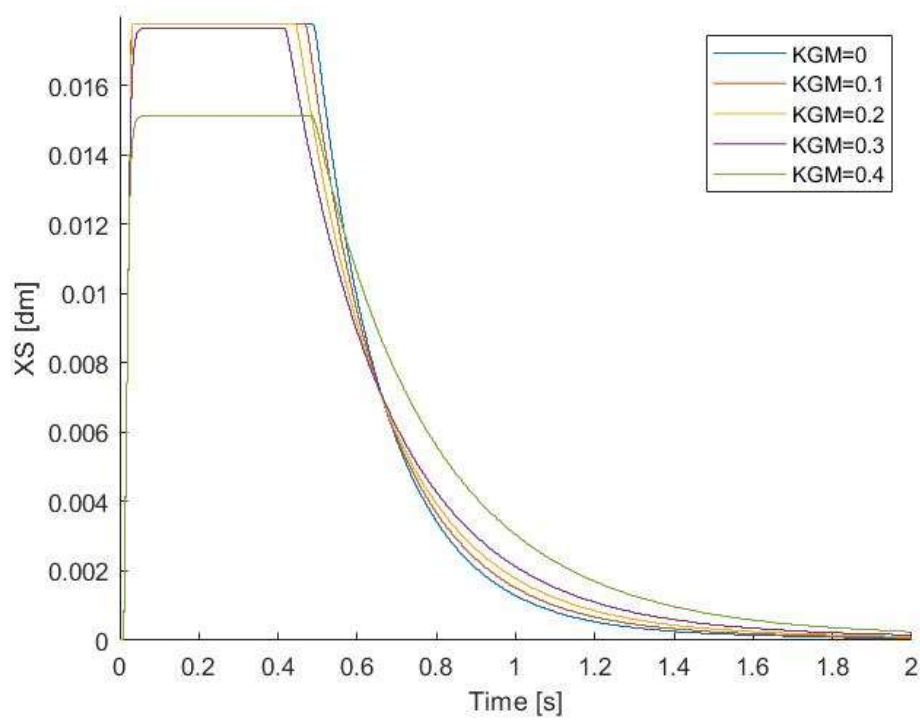


Figure 6.5: XS response to a step input signal.

It is possible to observe that a higher value of demagnetization leads to a slower system, as it can be seen from DXJ , XJ and XS diagrams; on the other hand, the servovalve will consume more current, presenting a delay during the transient of both $PI2$ and Cor . Even if a trend can be identified in all the quantities, it is not so relevant for the prognostic purpose.

6.1.2 Response to a ramp input signal

Below, responses to a ramp signal input, with slope of 0.1 m/s, of the analysed physical quantities are reported.

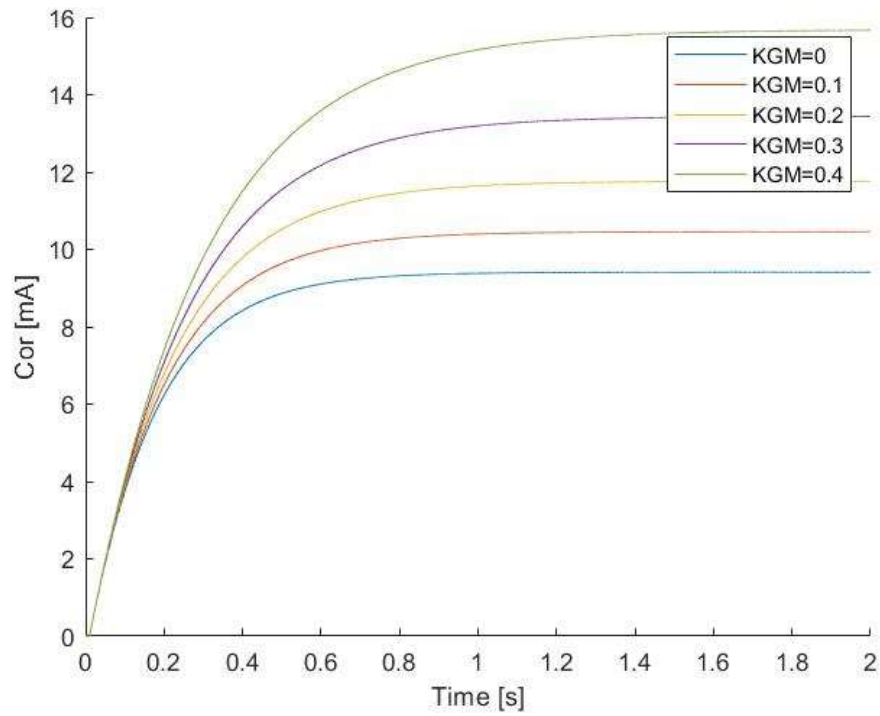


Figure 6.6: Cor response to a ramp input signal.

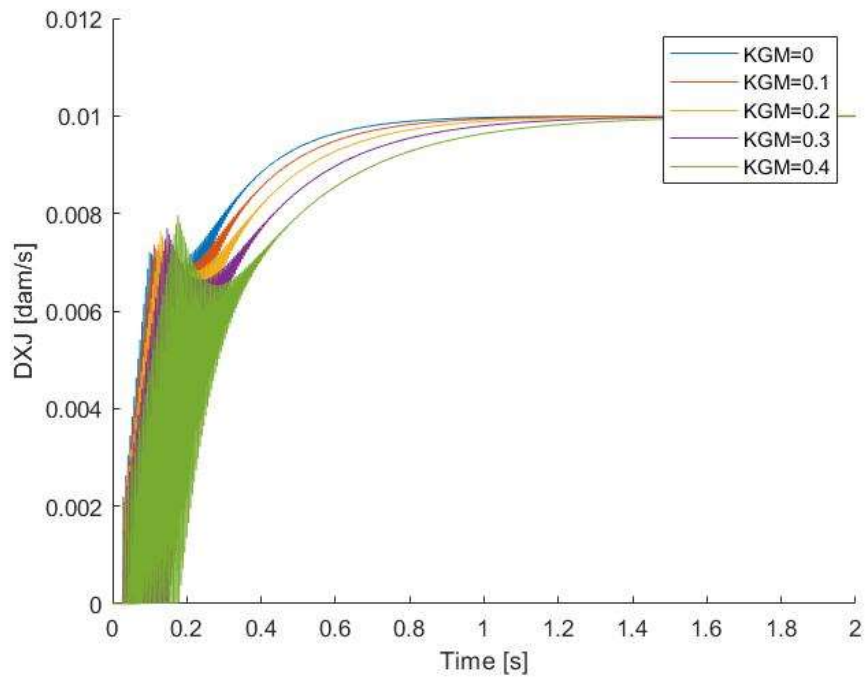


Figure 6.7: DXJ response to a ramp input signal.

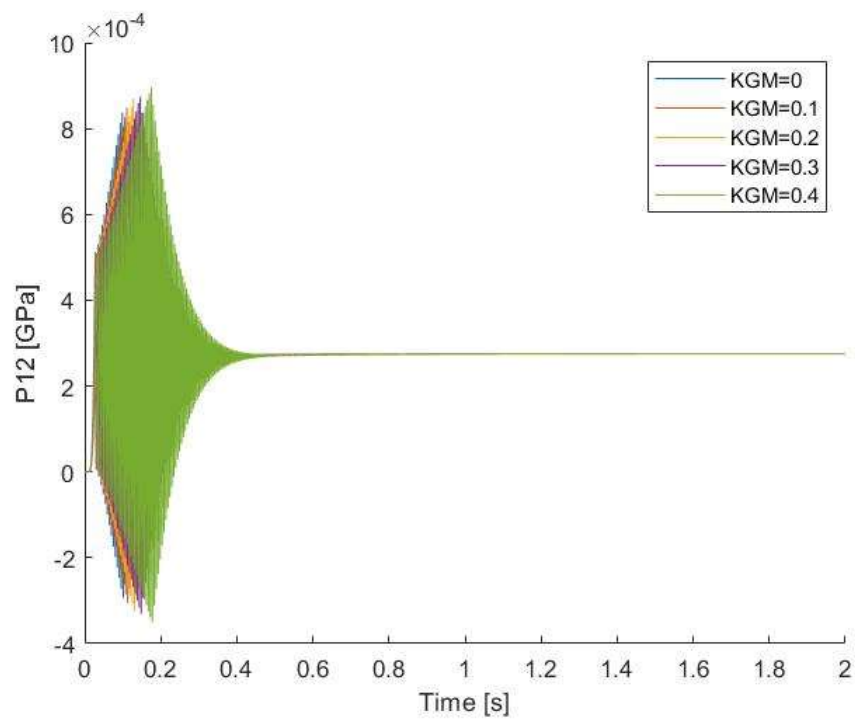


Figure 6.8: P12 response to a ramp input signal.

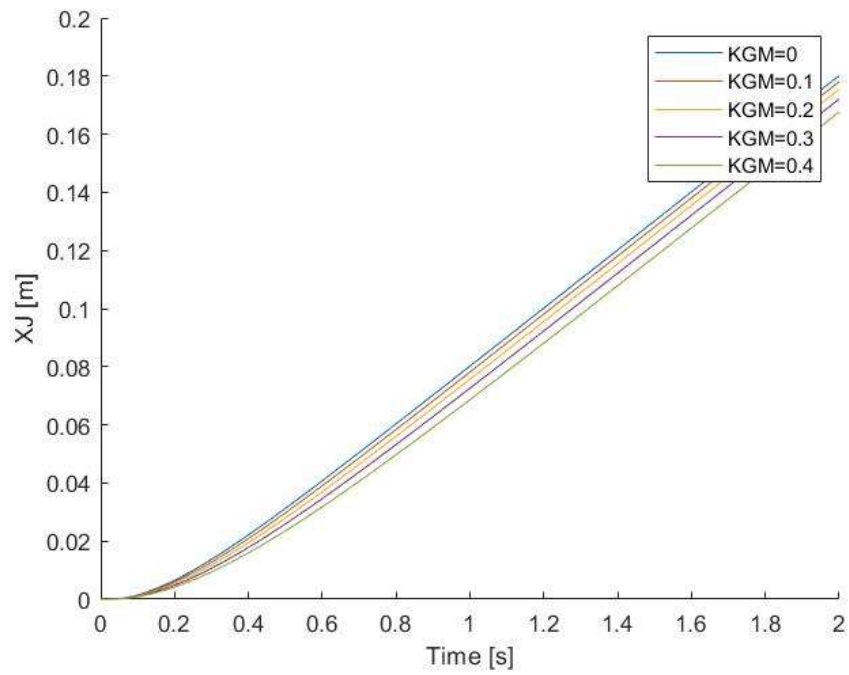


Figure 6.9: X_J response to a ramp input signal.

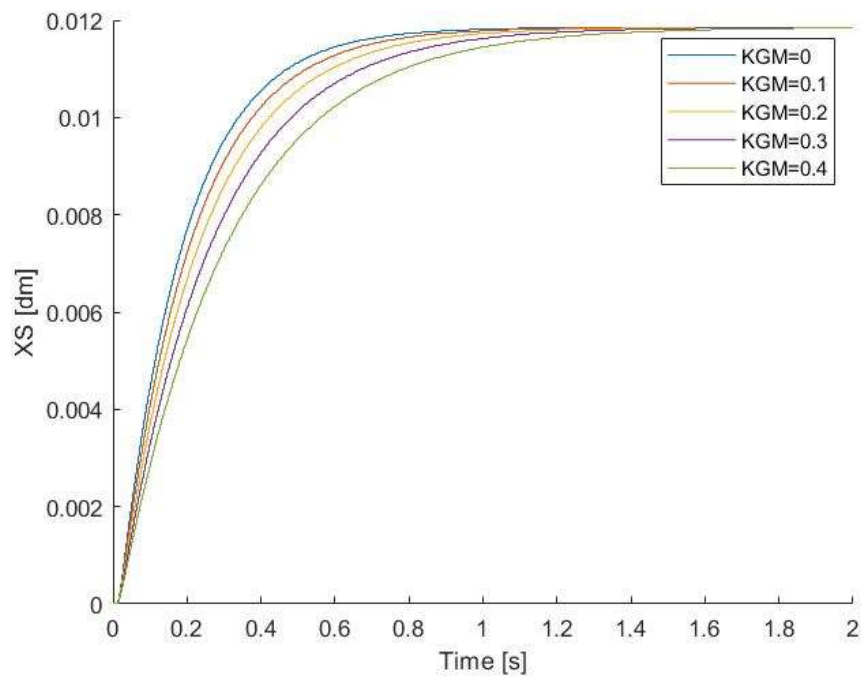


Figure 6.10: X_S response to a ramp input signal.

For higher values of KGM , it is possible to observe that the error between the ramp command and the jack position increases. XS and DXJ graphs show the same decrease in terms of system velocity, while $P12$ shows only a little higher oscillation respect to the increasing demagnetization. Finally, the current Cor shows how the demagnetization leads to a higher consumption of current that is visibly increasing with the KGM value.

6.1.3 Response to a sine input signal

Below, responses to a sine signal input, with amplitude of 0.2 m and frequency of 5 Hz, of the analysed physical quantities are reported.

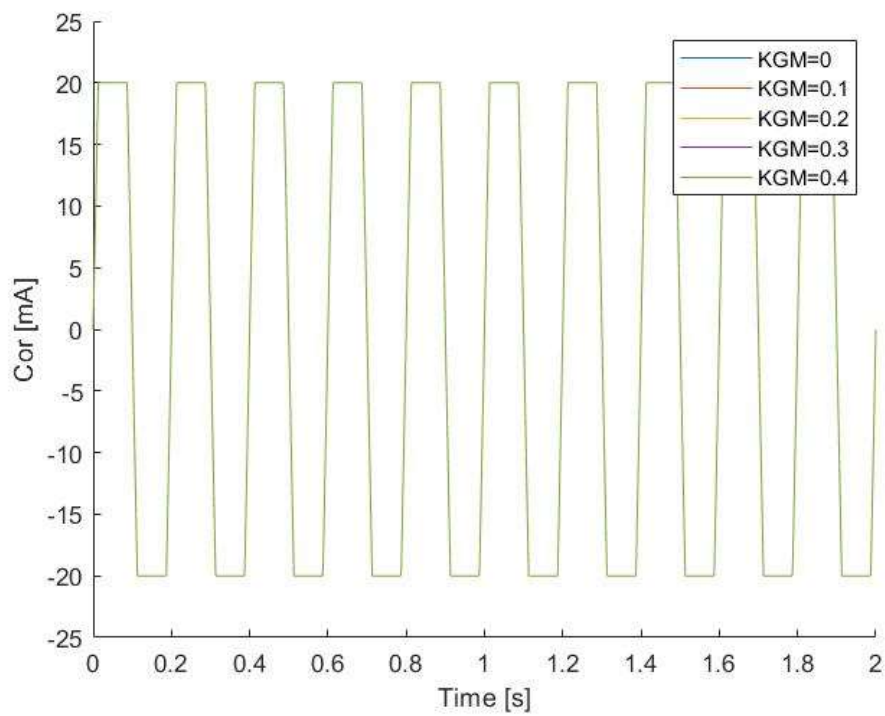


Figure 6.11: Cor response to a sine input signal.

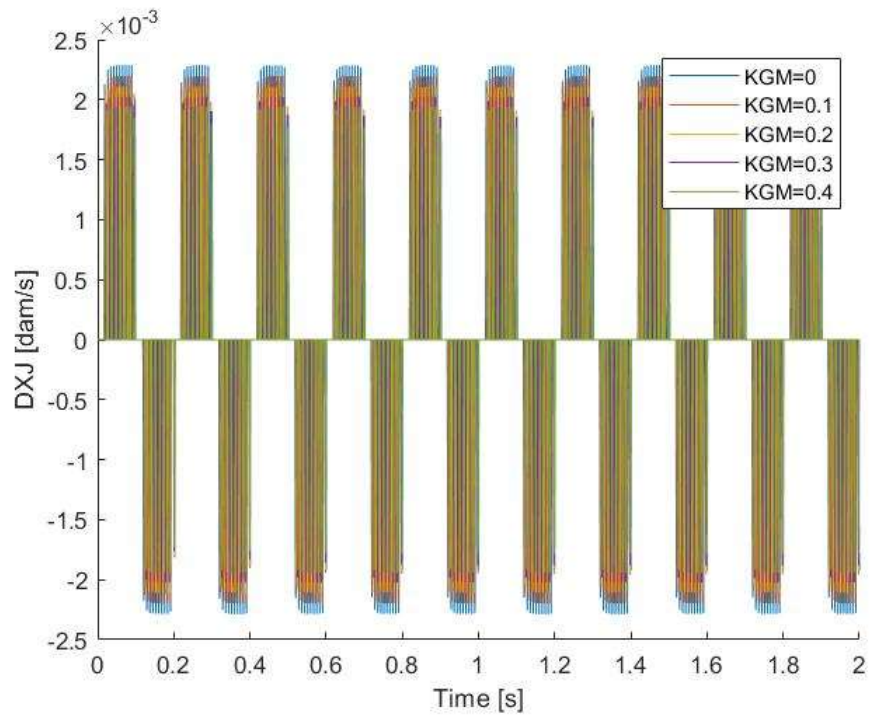


Figure 6.12: DXJ response to a sine input signal.

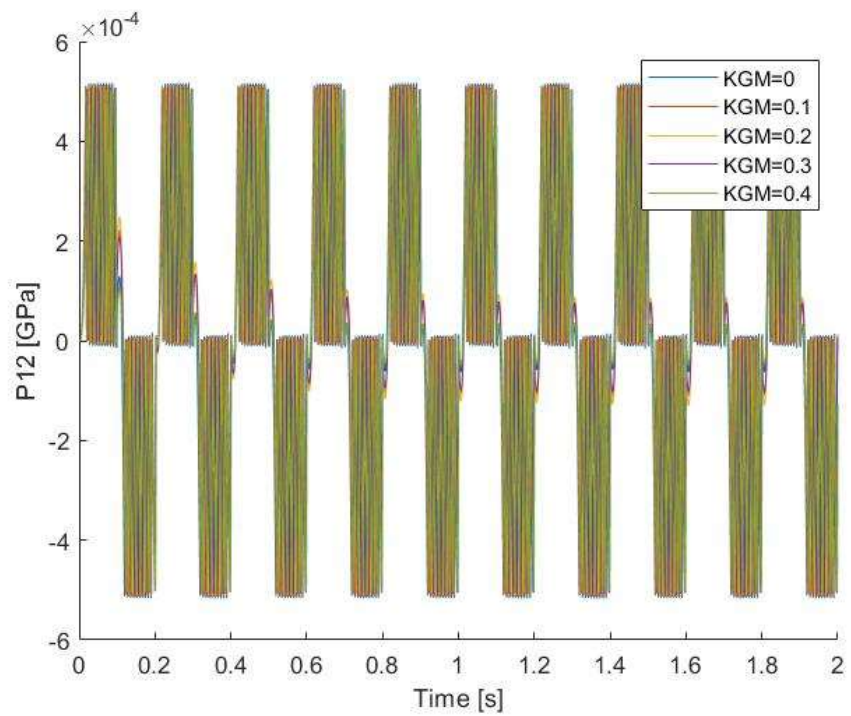


Figure 6.13: P12 response to a sine input signal.

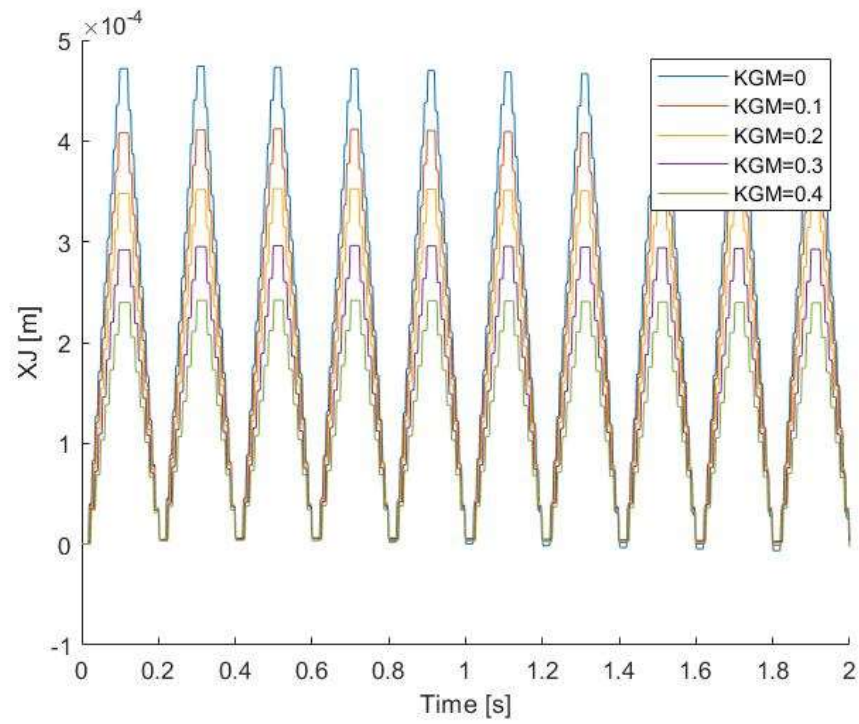


Figure 6.14: XJ response to a sine input signal.

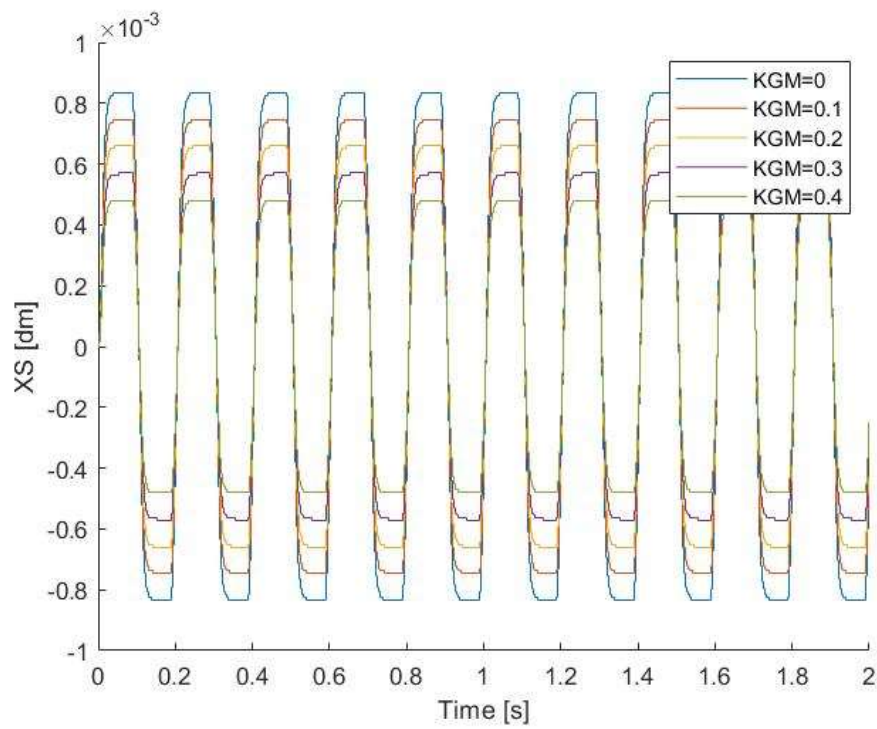


Figure 6.15: XS response to a sine input signal.

The sine input signal does not show a visible trend on *Cor*, *DXJ* and *PI2* graphs while it shows how, almost with the same current, the degraded system has a lower amplitude respect to *XS* and *XJ* displacements.

6.1.4 Prognostic parameter for *KGM* failure

The previous study shows how the ramp signal is the most suitable for the identification of this failure; in particular, the current absorbed by the torque motor shows a marked trend and its steady state can be assumed as the characteristic quantity for the identification. It is also an easy-to-read quantity, since an ammeter can be installed upstream of the torque motor. Not having a real system, the estimation of the absorbed current has been conducted with the High-Fidelity model in Simulink ambient.

The table reported below shows the steady state values of the absorbed current for different values of *KGM*:

KGM	Cor [mA]
0	
0.1	
0.2	
0.3	
0.4	

6.2 INCREASING STATIC FRICTION ON THE JACK

In this paragraph, increasing static friction on the jack will be analysed. This fault is simulated varying the static friction from its nominal value of 200 N to a reasonable value of 1000 N. Since the ratio between static and dynamic friction is fixed and equal to 2, it is possible to obtain the correspondent dynamic friction force, having a total overview of the friction condition of the component.

As the previous fault, several simulations have been executed for different entities of the fault and different type of input signals, plotting the same quantities used before.

6.2.1 Response to a step input signal

A step command with amplitude of 0.1 m is imposed. Below, behaviours of current absorbed by the torque motor (*Cor*), spool position (*XS*), differential pressure across the servovalve (*PI2*), position and velocity of the jack (*XJ* and *DXJ*) are reported.

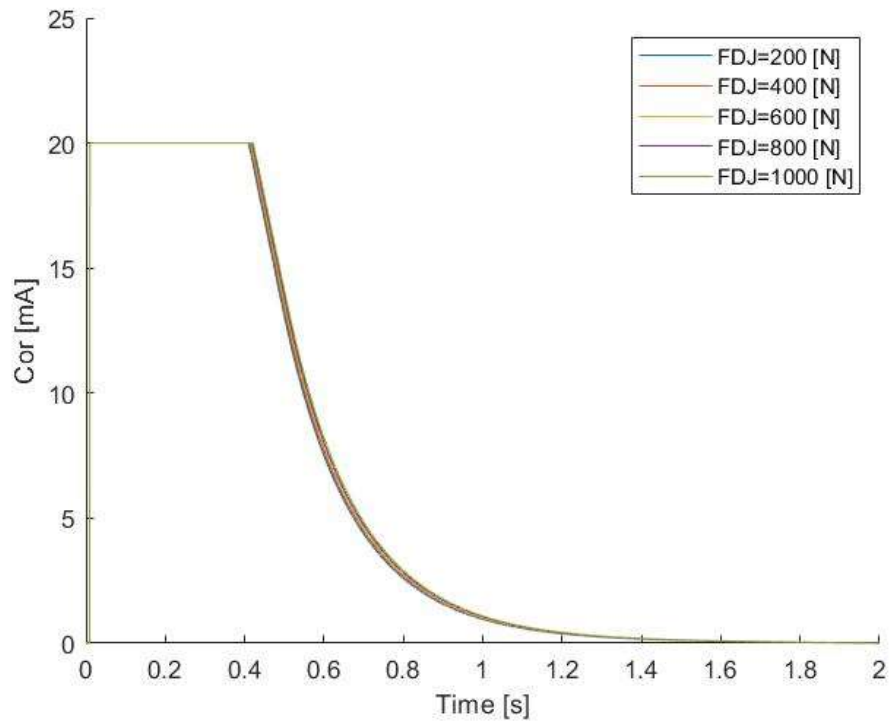


Figure 6.16: : Cor response to a step input signal.

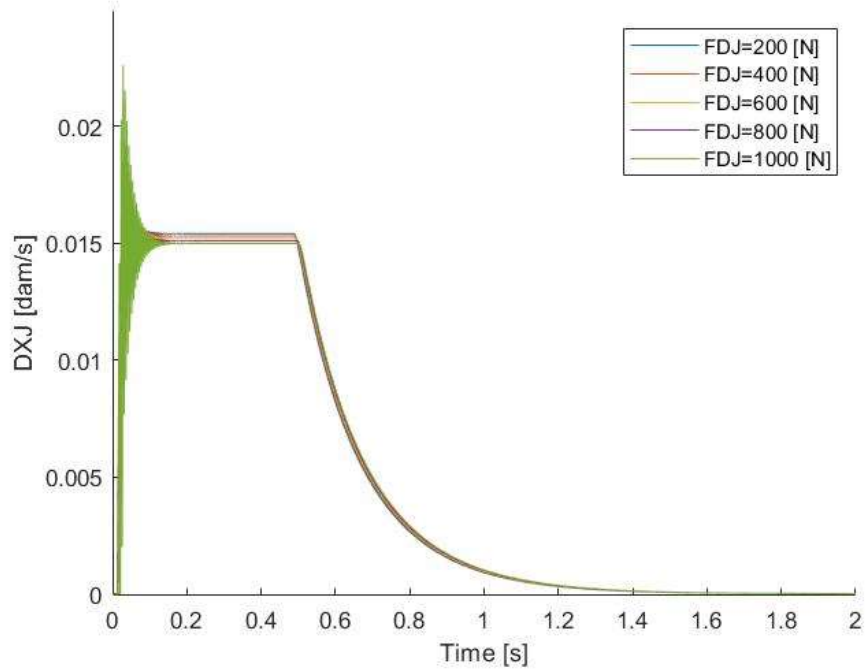


Figure 6.17: DXJ response to a step input signal.

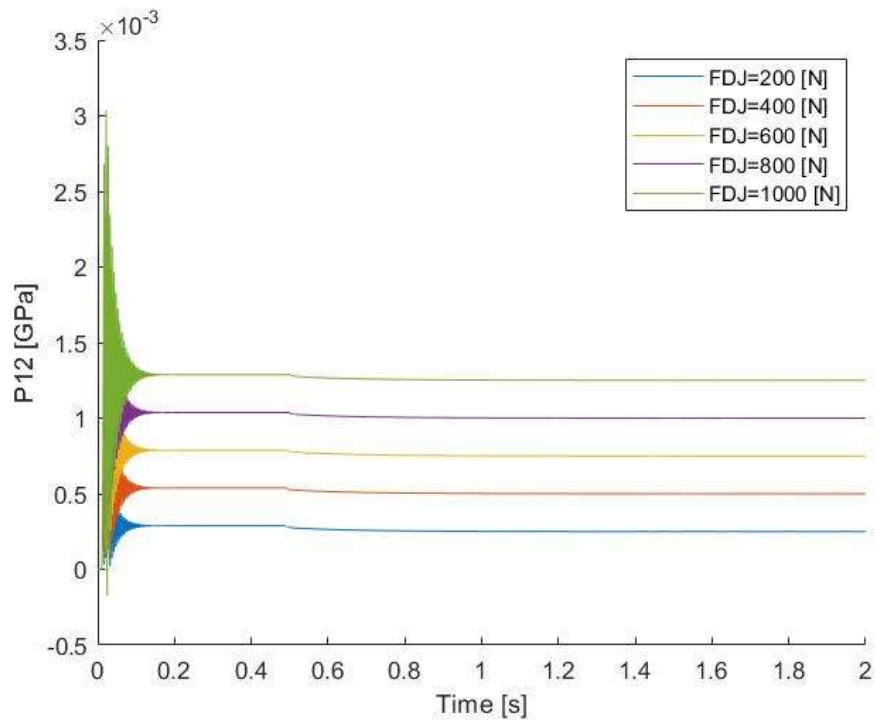


Figure 6.18: P12 response to a step input signal.

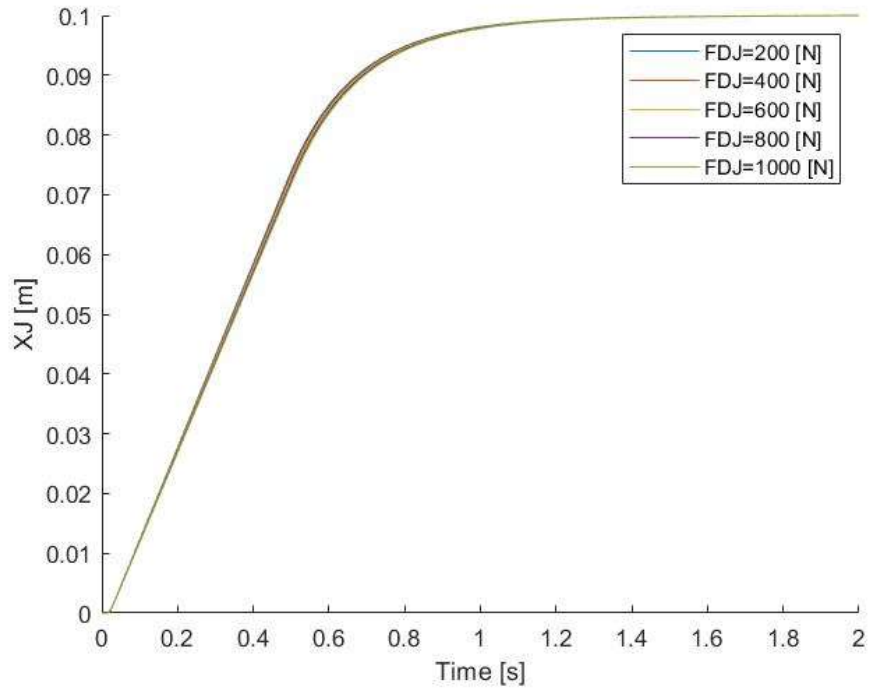


Figure 6.19: XJ response to a step input signal.

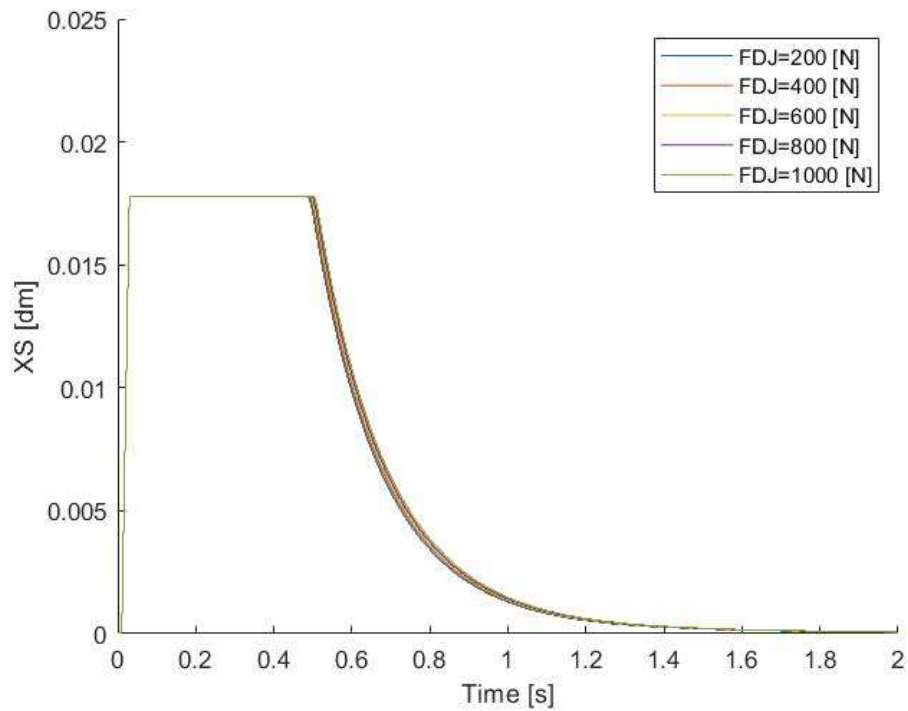


Figure 6.20: *XS response to a step input signal.*

It can be observed that all the quantities shown above do not show an appreciable trend respect to the increasing friction, except for the differential pressure $P12$, where, after an oscillating transient, a visible increase in the steady state value is present: this is due to the fact that the jack needs a higher force to overcome frictional forces.

6.2.2 Response to a ramp input signal

Below, responses to a ramp signal input, with a slope of 0.1 m/s, of the analysed physical quantities are reported.

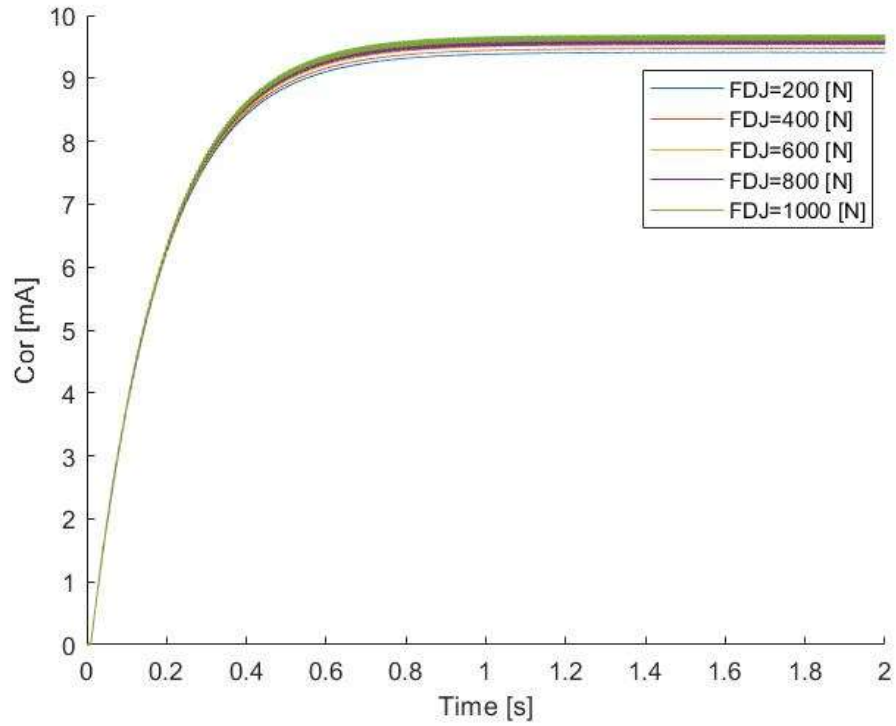


Figure 6.6: Cor response to a ramp input signal.

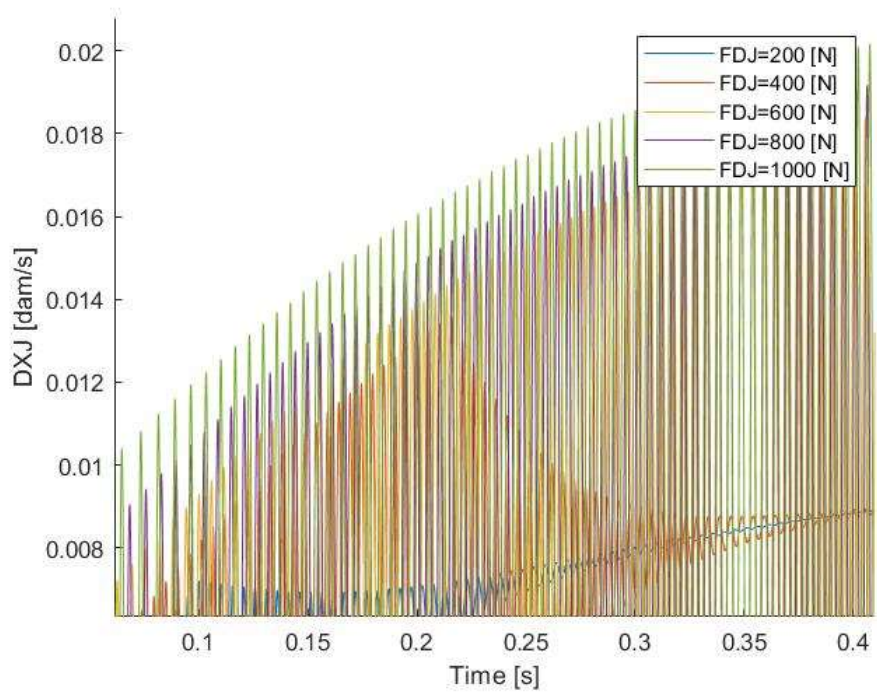


Figure 6.7: detail of DXJ response to a ramp input signal.

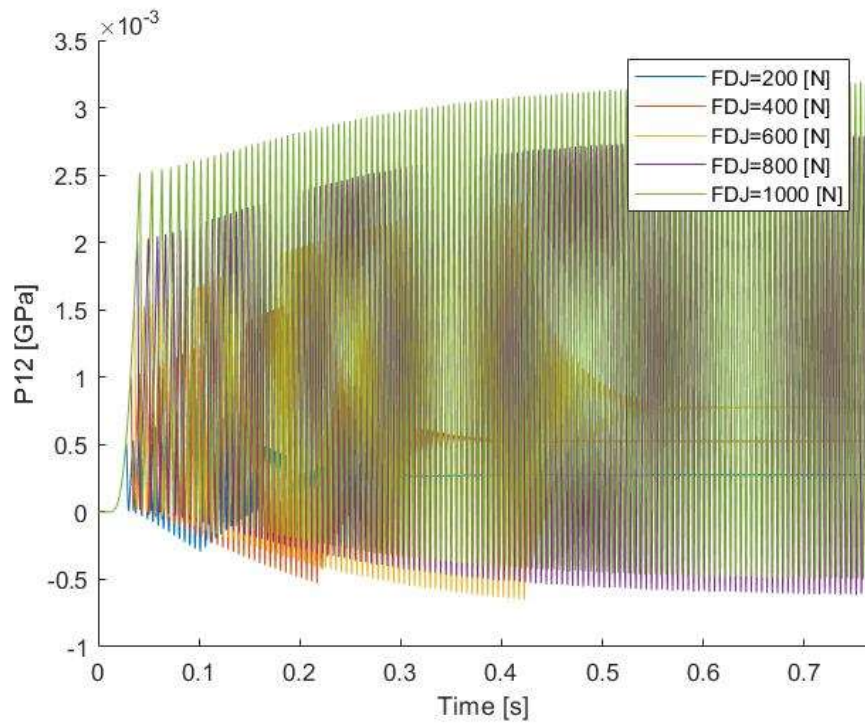


Figure 6.8: detail of P12 response to a ramp input signal.

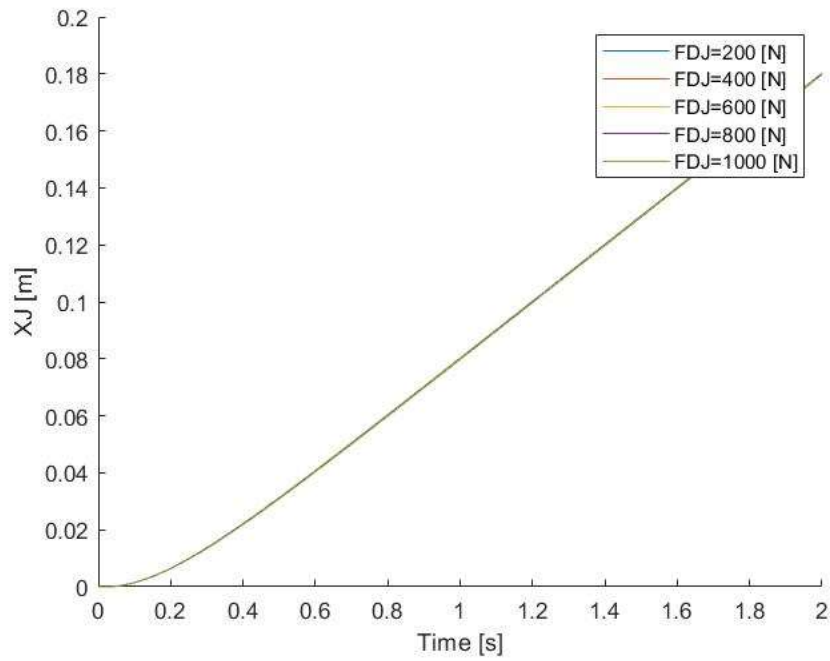


Figure 6.9: X_J response to a ramp input signal.

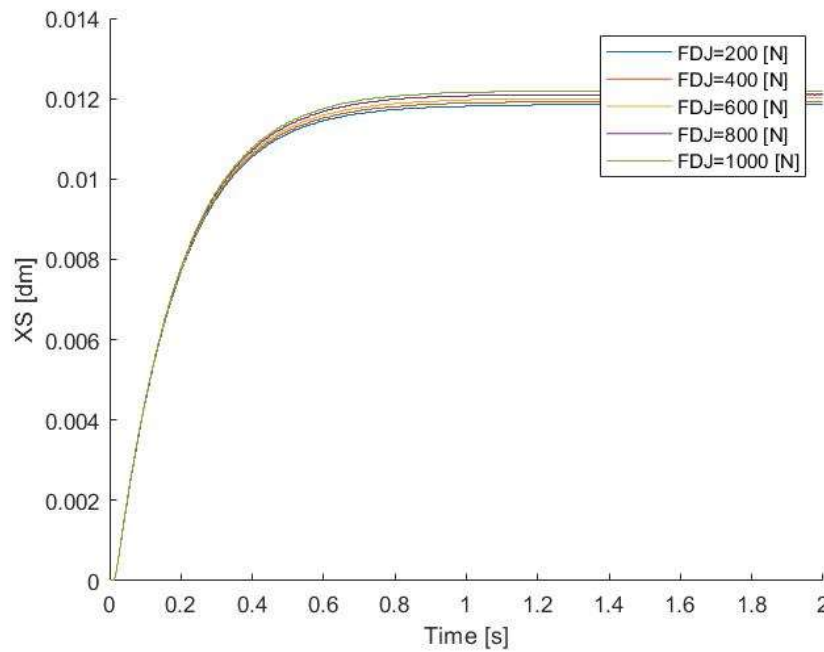


Figure 6.10: X_S response to a ramp input signal.

As it can be seen, no physical quantity can be useful as prognostic parameter.

6.2.3 Response to a sine input signal

Below, responses to a sine signal input, with amplitude of 0.2 m and frequency of 5 Hz, of the analysed physical quantities are reported.

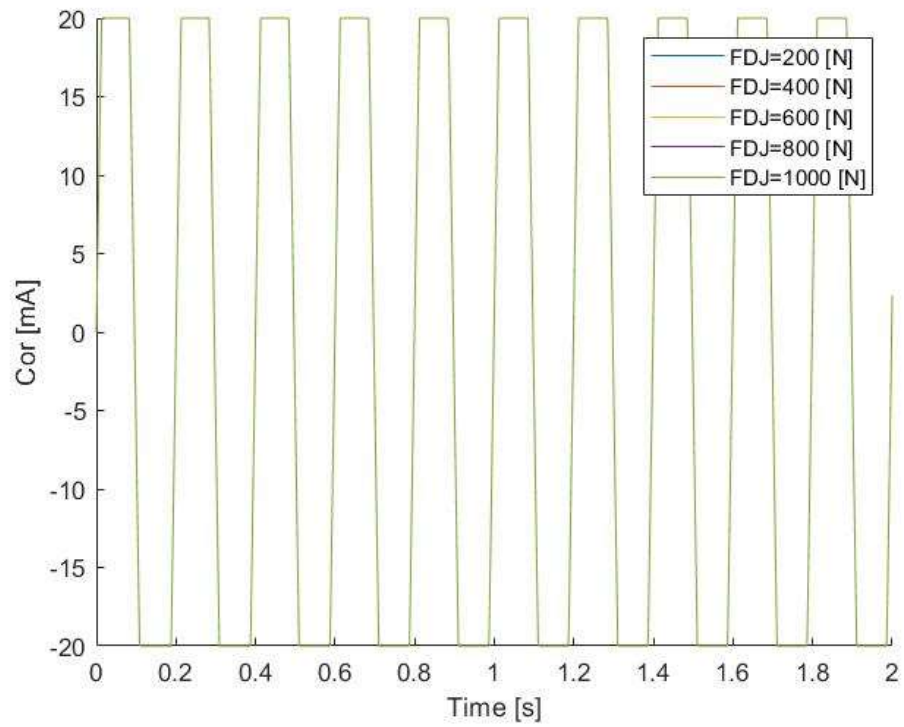


Figure 6.11: Cor response to a sine input signal.

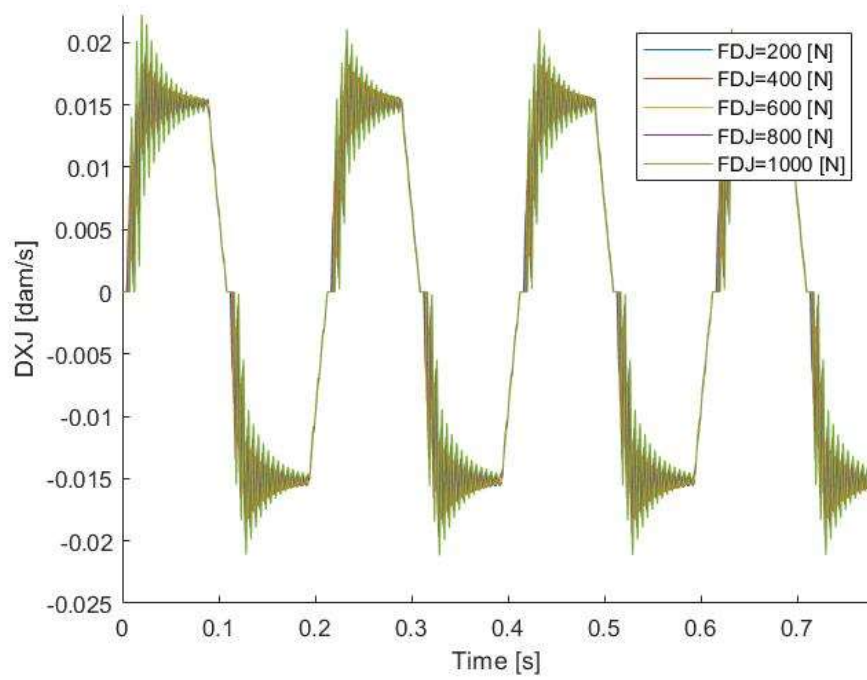


Figure 6.12: DXJ response to a sine input signal.

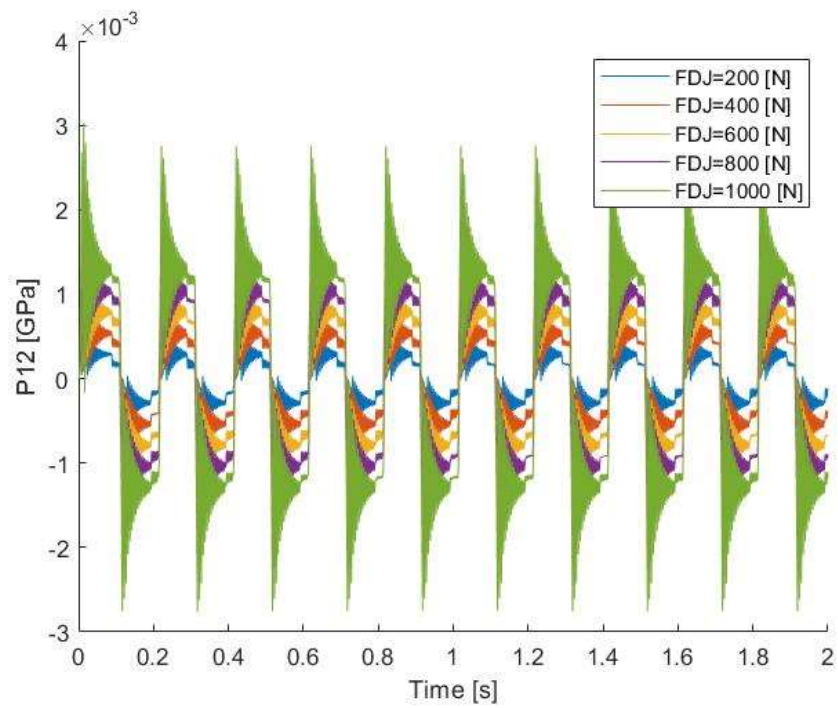


Figure 6.13: P12 response to a sine input signal.

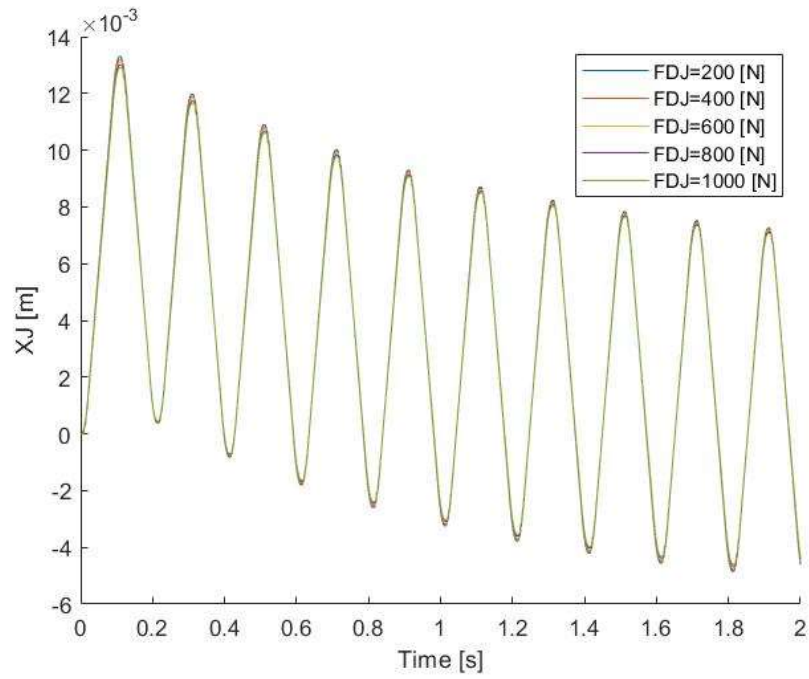


Figure 6.14: X_J response to a sine input signal.

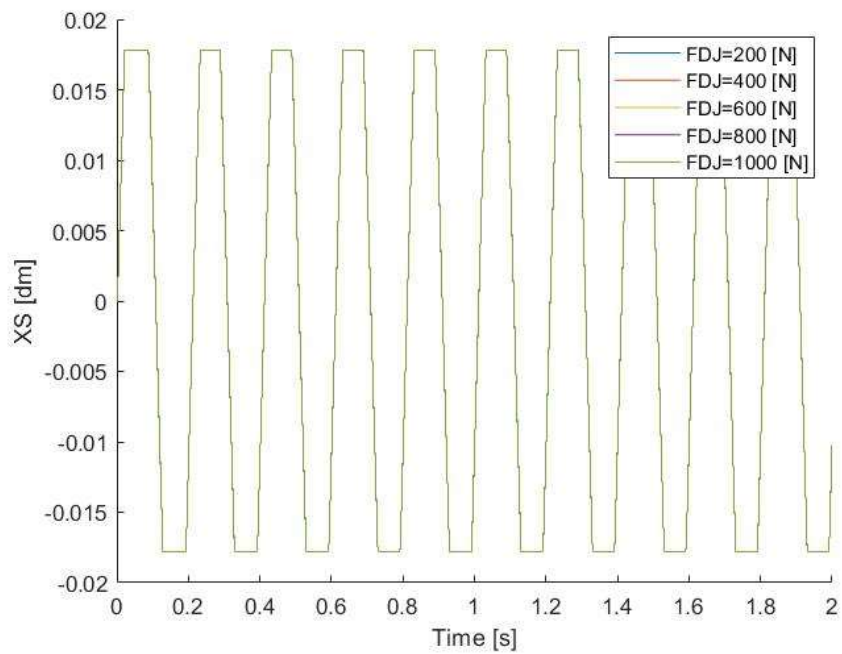


Figure 6.15: X_S response to a sine input signal.

Also in this case, a marked variation on the quantities is not present, making the sine input signal not effective for the diagnostic procedure.

6.2.4 Prognostic parameter for *KGM* failure

The previous study shows how the step signal is the most suitable for the identification of this failure; in particular, the differential pressure across the two chambers of the jack shows a marked trend and its steady state can be assumed as the characteristic quantity for the identification. It can be measured through a pressure-meter that can be easily installed in the system.

The table reported below shows the steady state values of the pressure *P12* for different values of *FDJ*:

FDJ [N]	P12 []
200	
400	
600	
800	
1000	

6.3 FAULT COMBINATION ANALYSIS

In the previous analysis, considered faults have been simulated one by one. In the reality, all faults can appear simultaneously and they can influence each other. Moreover, it must also consider the external factors that can lead to a premature wear of the components, such as an increment of the temperature that can compromise the oil properties. For these reasons, the final analysis must consider both faults simultaneously.

The two quantities considered for the diagnostic procedure are the ramp response of the current absorbed by the torque motor and the step response of the pressure across the two chambers of the jack so, the command used in this paragraph is composed of the following sequence:

- Ramp signal with slope equal to 0.1 m/s for the identification of the steady state current, starting from 0 to 2 seconds;
- Step signal with amplitude -0.2 m, that leads the signal again to 0 m to avoid saturation in the second useful part of the input signal;
- Step signal with amplitude 0.1 m, applied at 4 seconds and maintained until the finish of the simulations at 6 seconds.

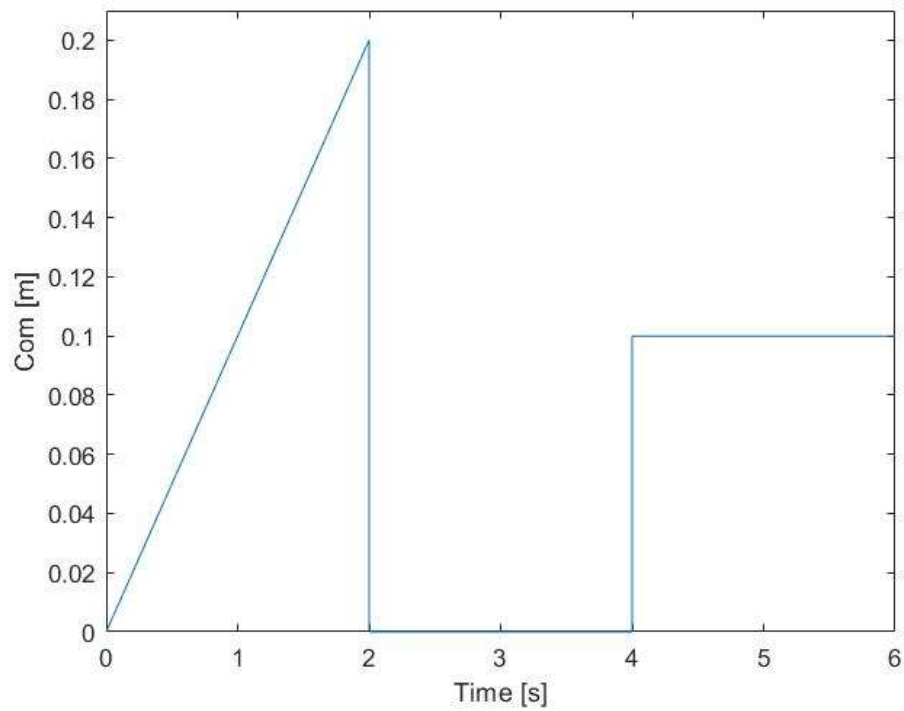


Figure 6.16: Input signal used.

Steady state values of *Cor* (ramp response) and *P12* (step response) are reported in the table below (values of *Cor* for *FDJ* > 600 have been obtained through a mean value, since it presents a little oscillation):

KGM	FDJ [N]	Cor [mA]	P12 [MPa]
0	200	9.4089	250.972
0	400	9.4726	501.076
0	600	9.5324	751.027
0	800	9.6221	1001.011
0	1000	9.6944	1251.038
0.1	200	10.4586	251.259
0.1	400	10.5258	501.294
0.1	600	10.5934	751.163
0.1	800	10.6862	1001.361
0.1	1000	10.7662	1251.460
0.2	200	11.7648	251.625
0.2	400	11.8406	501.718
0.2	600	11.9156	751.816
0.2	800	12.0198	1001.920
0.2	1000	12.1045	1251.821

0.3	200	13.4388	252.216
0.3	400	13.5283	502.112
70.3	600	13.6169	752.319
0.3	800	13.7141	1002.392
0.3	1000	13.8309	1252.352
0.4	200	15.6703	253.348
0.4	400	15.7684	503.585
0.4	600	15.8739	753.395
0.4	800	16.0122	1003.799
0.4	1000	16.1249	1253.851

As it can be seen, each fault does not influence in a significant way the quantity chosen for the other, making these parameters very effective for the fault identification.

7 OPTIMIZATION ALGORITHMS

Nowadays, it happens often, in different scientific fields, that is necessary to find a way to minimize or maximize a variable that bonds two or more complex systems. In this thesis, it is necessary to compare the High-Fidelity system, used as reference, and the Low-Fidelity model, in order to have a complete procedure for the diagnostic and prognostic of the electro-hydraulic actuation system. To do this, it is fundamental to set a comparative method that, through simulations and iteratively, can calculate a scalar value that represents the degree of match of the models, receiving as input the HF. This is the aim of the objective function.

The identification of the most useful objective function for the considered system is the most important problem for the optimization algorithms. It represents the conjunction between the physic properties of the system and the mathematical aspect of the algorithm: choosing the wrong objective function, it can compromise the reliability of the results. Once the objective function is defined, it is used by the optimization algorithm in order to identify the faults that affects the system, minimizing its own value. The results of the optimization process correspond to the real conditions of the system.

There are several algorithms that can accomplish this task, but different aspects must be considered in order to choose the proper one for the considered problem: robustness, that is the reliability of the method in reaching the absolute minimum or maximum of the objective function, accuracy, that is the capability to calculate its exact value and the velocity of convergence, that indicates how much time the algorithm needs to reach the correct value.

There are three different classes of optimization algorithms: enumerative, deterministic and heuristic.

The enumerative method consists in searching the optimal solution in all points of the domain without any specification, but with a trial-and-error procedure. It is not so much demanding in terms of computational effort but is very time consuming.

The deterministic method, instead, calculates the value of the objective function in specific points, starting from a fixed one. The algorithm, successively, tests the points in the neighbourhood of the reference and it calculates the gradient of the fitness function in these directions. This can be a very useful algorithm for objective functions that do not present local minima or maxima or discontinuities. However, it is not recommended for problems with too many variables since the process can be very demanding in terms of computational effort in calculating the gradient of the objective function.

Finally, heuristic methods can be very useful in finding solutions that are impossible or very demanding to be found. These algorithms do not guarantee an exactly optimal solution, but they can be used to find an acceptable solution in a reasonable time. In this thesis, the genetic algorithm will be used.

7.1 GENETIC ALGORITHM

Genetic algorithms are powerful instruments to solve optimization problems. They are heuristic methods that take inspiration from genetics and natural selection principle of Darwin.

Genetic algorithms use a set of solutions that evolve in intervals, called generations, where the evolution is guided by the research of the optimal solution through the “goodness” of the individual or generation: through the objective function it is possible to compare best individuals and use them to create the successive generation. According to this theory, in fact, each individual has its own characteristics and properties that can be observed: this is the phenotype. These characteristics are determined by genetic setup, not visible, called genotype, that are the fundamental unit of chromosomes.

The base structure of a genetic algorithm has a cyclic functioning, where every cycle represents a generation and at each step all operations to generate a new population are made. At the first step, an initial population is created, while the successive steps are repeated at each generation: best individuals are chosen in base of their fitness function value, while the successive steps create the new generation through the operations of crossover and mutation, which combine or modify the characteristics of individuals.

The structure of the algorithm is shown below.

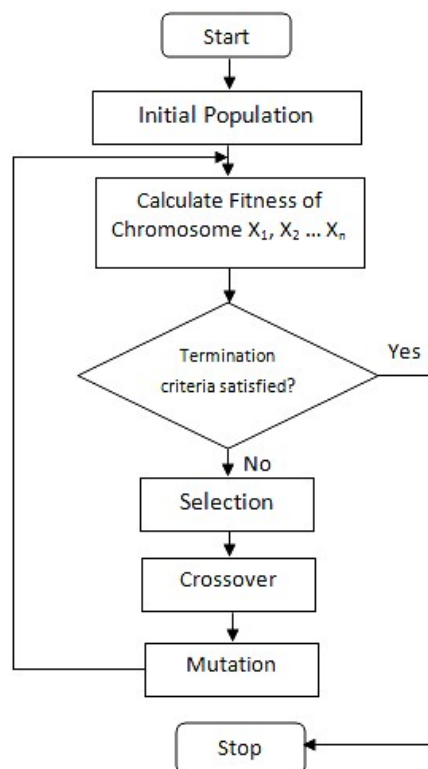


Figure 7.1: Basic scheme of a genetic algorithm (Singh, 2013, p. 57).

The first step of the problem consists in the definition of the fitness function. It represents the objective function that the algorithm must minimize and indicates how much an individual is far from the optimal solution; it represents the external ambient for the biological individuals where they can survive or not. However, the objective function can have local and global minimum, so, if the initial population is concentrated in the local minimum, the algorithm will converge to this point. For this reason, it is important to have a sufficient high number of individuals covering most of the domain to explore all the possible solutions, but, at the same time, this number must not be very high to not make the algorithm very time consuming. There are several options to obtain an initial population in MATLAB: the default option creates a random initial population that satisfies the bounds, if present, and well-dispersed in the domain; as alternative, it is possible to specify totally or partially the initial population to have interesting individuals, already in the first population. If it is wanted to specify only a part of the initial population, the algorithm calls the function *CreationFcn* to fill the remaining individuals.

Once the initial population is defined, the fitness value of each individual is calculated and a sub-population is chosen to generate new solutions. There are different criteria for the selection: the default option is set on the *rank scaling function*. It consists in sorting the raw scores of each individual and scaling them respect to their position. It results a conservative method, since also less fit individuals have a chance to be chosen for the reproduction, so important genetic portions can be used, but, at the same time, the convergence of the algorithm is slower.

Another widely used technique is the *proportional selection* that selects the best individuals in base of a probability, proportional to the fitness function value: at first the total fitness function value of the population is calculated as:

$$F_{max} = \sum_{i=1}^n f(x_i)$$

$$F_{min} = \sum_{i=1}^n \frac{1}{f(x_i)}$$

Where x_i represents the i th individual. The first one is used for the research of the maximum of the fitness function, while the second for the minimum. With this value, it is possible to obtain the probability of selection of each individual according to

$$p_i = \frac{f(x_i)}{F_{max}} \quad p_i = \frac{1}{F_{max}} \frac{1}{f(x_i)}$$

The results can be represented as a wheel divided into segments, where each segment is proportional to the probability associated at each individual. The scheme is reported below.

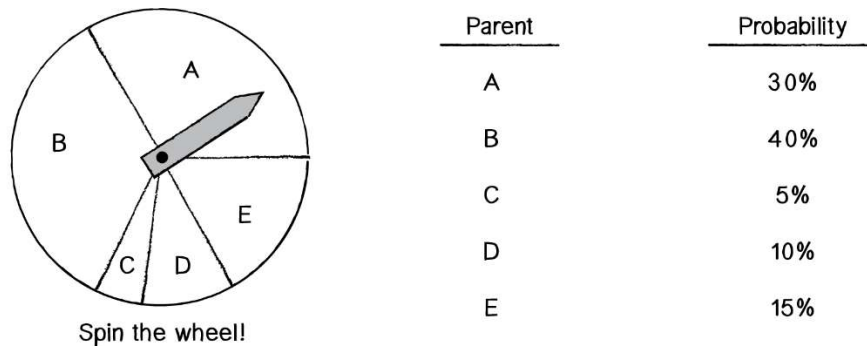


Figure 7.2: Proportional selection scheme.

At this point, the wheel is spun k times to choose the individuals for the reproduction.

The new generation $P(n+1)$ is obtained from the previous one $P(n)$ through several steps:

- 1) Selection for reproduction, the selected best individuals are introduced into an intermediate population $P1$ and after into the mating pool, as already described above;
- 2) Crossover: the crossover operator is applied to the individuals in the mating pool to obtain a new population $P2$;
- 3) Mutation, the mutation operator is applied to the individuals $P2$ to obtain another population $P3$;
- 4) Selection for replacement and survival, the new generation $P(n+1)$ will contain mostly individual from $P3$, but it can contain also individuals from $P(t)$ that have not be chosen for reproduction or the best ones.

New chromosomes are generated from the parents that transmit their genetic heritage, in this way new solutions are similar to the parents, otherwise the convergence of the algorithm would not be guaranteed. Crossover considers these aspects, recombining genetic material of two or more chromosomes and it is described exactly as the exchange of homologue genetic material.



Figure 7.3: Crossover in genetics and binary single point crossover (Simi, 2007, p. 11).

There are several crossover options: scattered, single point, two points, arithmetic, intermediate, heuristic.

Scattered function creates a random binary vector, where a bit from the first parent corresponds to 1 and a bit from the second one corresponds to 0. For example, if the parents are defined as

P1=[12345678]

P2=[abcdefgh]

And the reproduction vector is

Reproduction=[10101010]

The new child will be

Child=[1b3d5f7h]

Single point function chooses an integer number i between 1 and $n-1$ number of bits, dividing the genes from the parents into two parts: the first part composed by genes with index less or equal to i and the second by genes with index greater than i . The resulting child will have the first part from the first parents and the second part from the second. For example, if the parents are

P1=[12345678]

P2=[abcdefgh]

And the crossover point is 3, the resulting child is

Child=[123defgh]

Two points crossover works similarly, but it chooses two integer numbers, obtaining three portions of genes; the resulting child will have for example the middle portion of genetic code from the second parent and the complementary part from the first one.

The options illustrated so far work on binary codification, while the remaining ones work on real numbers.

Arithmetic crossover creates children that are the weighted arithmetic mean of two parents.

Intermediate crossover creates children by taking a weighted average of the parents; it is possible to specify the parameter *ratio* of the formula

$$\text{Child} = p1 + \text{rand} * \text{ratio} * (p1 - p2)$$

Finally, *heuristic crossover* returns a child that lies on the line containing the two parents, a small distance away from the parent with the better fitness value and farther from the parent with the worse fitness value. It is possible to specify the same parameter *ratio*, as the *intermediate crossover*, of the formula

$$\text{Child} = p2 + \text{ratio} * (p1 - p2)$$

About the last operator, mutation, it introduces little changes in the genetic heritage to create new chromosomes. The effect of this operator is to modify the chromosomes of an individual, in order to explore new areas of the domain of the solutions still not explored: this is made to also avoid the convergence in a local minimum. However, an excessive use of the mutation leads to an instability of the algorithm that can not converge anymore and for this reason, it is applied with a very small probability, that oscillates in [0.001,0.01]. The optimization tool has several options: gaussian, uniform and adaptive feasible function. *Gaussian mutation* adds a random number taken from a Gaussian distribution with mean 0 to each entry of the parent vector. *Uniform mutation* is a two-step process: first, the algorithm selects a fraction of the vector entries of an individual for mutation, where each entry has a probability *rate* of being mutated, while in the second one, each selected entry is replaced by a random number selected uniformly from a specified range. *Adaptive feasible function* randomly generates directions that are adaptive with respect to the last successful or unsuccessful generation, satisfying bounds and linear constraints.

7.2 PROGNOSTIC ANALYSIS THROUGH GENETIC ALGORITHM

In the following paragraph, setting and details of genetic algorithm used for the prognostic analysis will be illustrated.

At first, the genetic algorithm has been tested on single faults, respectively the demagnetization of the torque motor and the increasing static friction on the jack. The first one is the demagnetization of the torque motor.

As pointed in the previous paragraph, the physical quantity useful for the identification of this fault is the response of the current absorbed by the torque motor to a ramp of slope 0.1 m/s as input. In this perspective, differences between High-Fidelity and Low-Fidelity models current responses have been analysed for different values of *KGM*, obtaining the sequent responses.

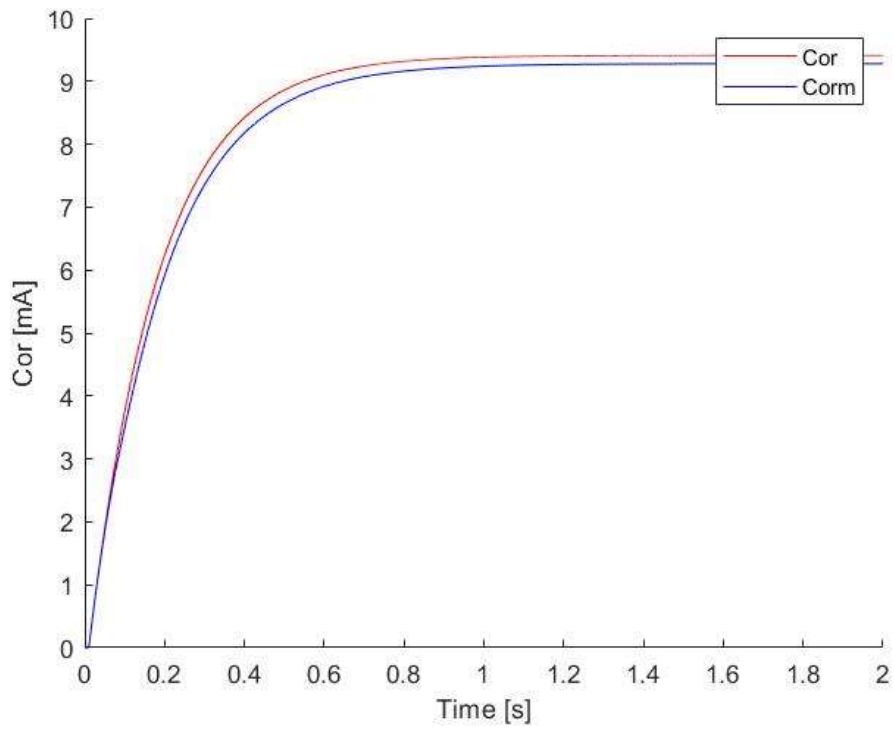


Figure 7.4: HF and LF Cor responses for $KGM=0$.

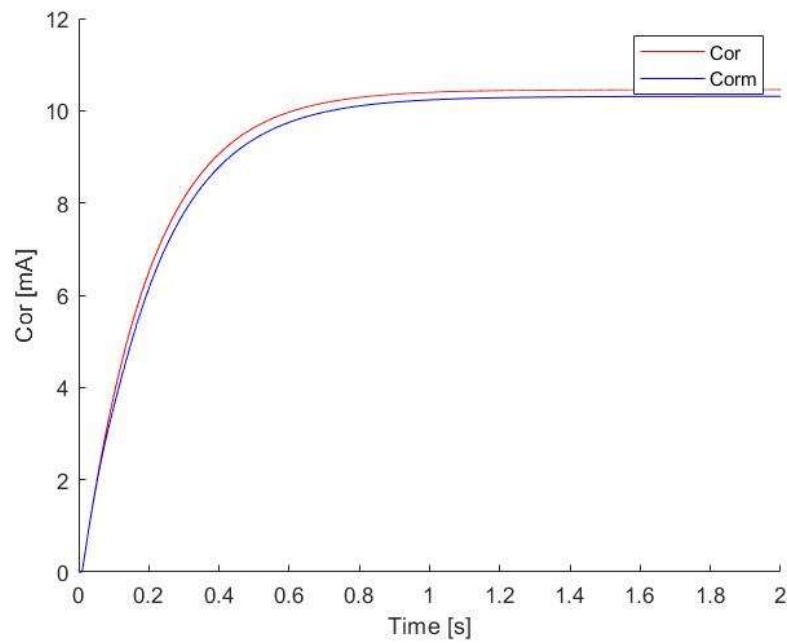


Figure 7.5: HF and LF Cor responses for $KGM=0.1$

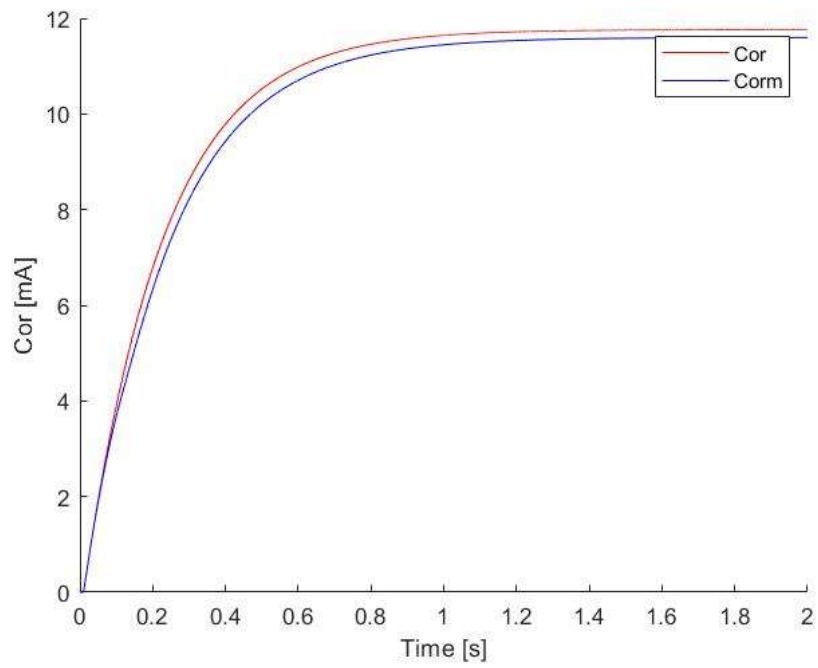


Figure 7.6: HF and LF Cor responses for $KGM=0.2$

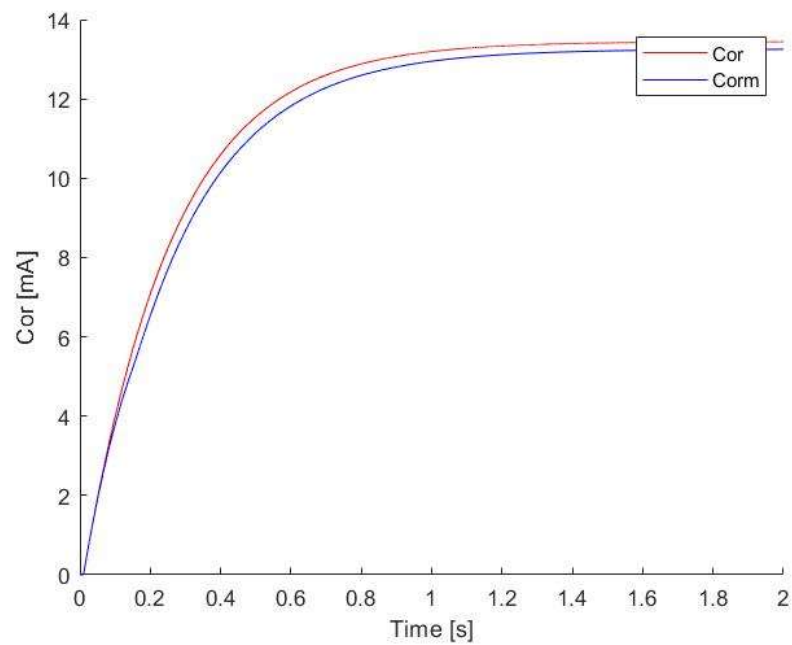


Figure 7.7: HF and LF Cor responses for $KGM=0.3$.

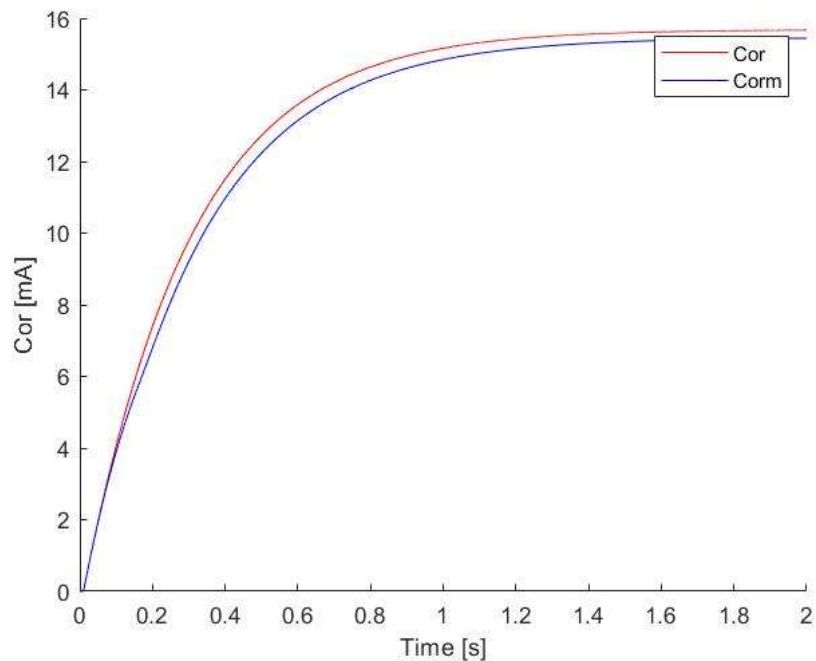


Figure 7.8: HF and LF Cor responses for KGM=0.4

As it can be noticed, a difference of 0.15 mA between the two responses can be noticed in all the simulations. For this reason, the objective function adopted for the prognostic analysis has been chosen as the absolute value of the difference between the steady state of the High-Fidelity current and the steady state of the current in the Low-Fidelity model evaluated at the same time interval; an additional value of 0.15 mA is subtracted from the current difference to have a better correspondence. In Figure 7.9, code of the function used by the genetic algorithm is shown, where the variable *fitness* corresponds to the objective function.

```
function [fitness]=simulate(vars)
    global KGMm Corrente
    KGMm=vars;
    sim LF.slx
    Correntem=Corm.data(190001)
    fitness=abs(Corrente-Correntem-0.15)
end
```

Figure 7.9: Code of the objective function.

Below the results of this preliminary analysis are reported.

KGM	KGMm	Err % KGM
0	0,0187	-
0.1	0,0997	0,3
0.2	0,2009	0,45
0.3	0,3022	0,7333333
0.4	0,4058	1,45

The results approximate very well the values of KGM , with a percentual error lower than 1% in all cases, except for the last one where the error is 1,45%.

After the demagnetization of the torque motor, the second fault analysed is the increasing static friction on the jack. As already said before, the characteristic quantity of this fault is the pressure across the chambers of the jack, in response to a step of amplitude 0.1 m. In this perspective, differences between High-Fidelity and Low-Fidelity pressure responses have been analysed for different values of FDJ in both models, obtaining the sequent responses.

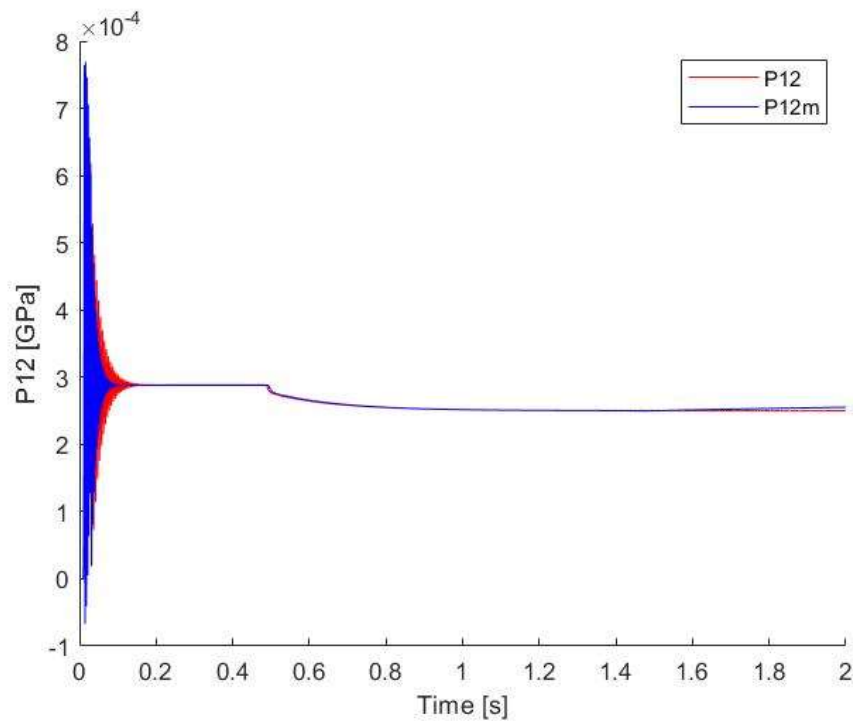


Figure 7.10: HF and LF P12 responses for $FDJ=200\text{ N}$

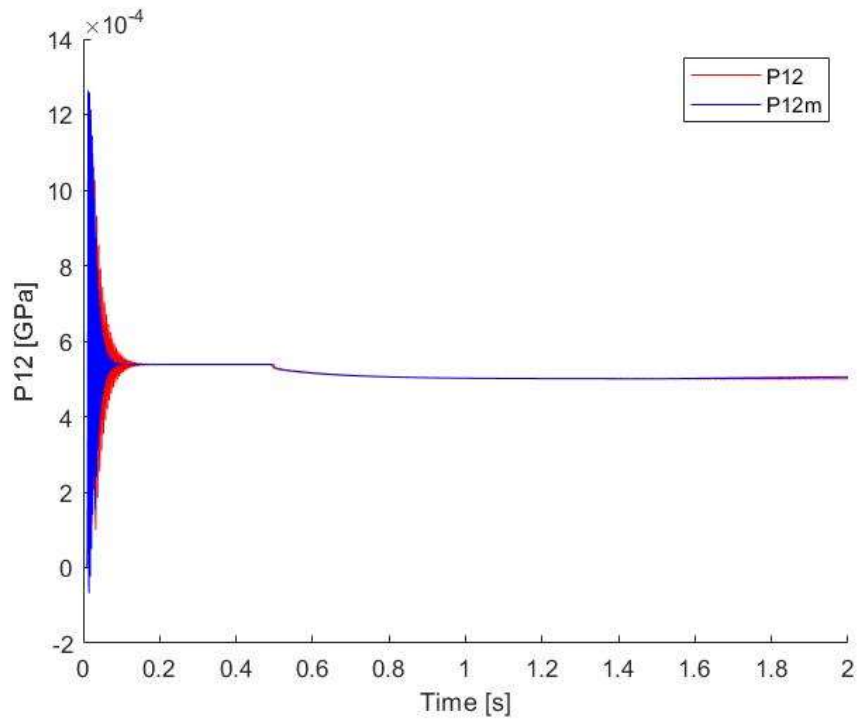


Figure 7.11: HF and LF P12 responses for FDJ=400 N

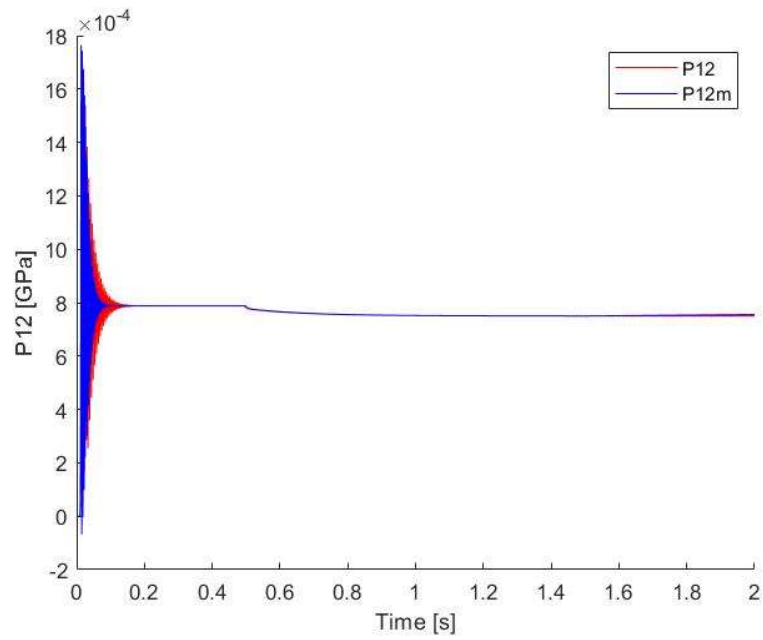


Figure 7.12: HF and LF P12 responses for FDJ=600 N

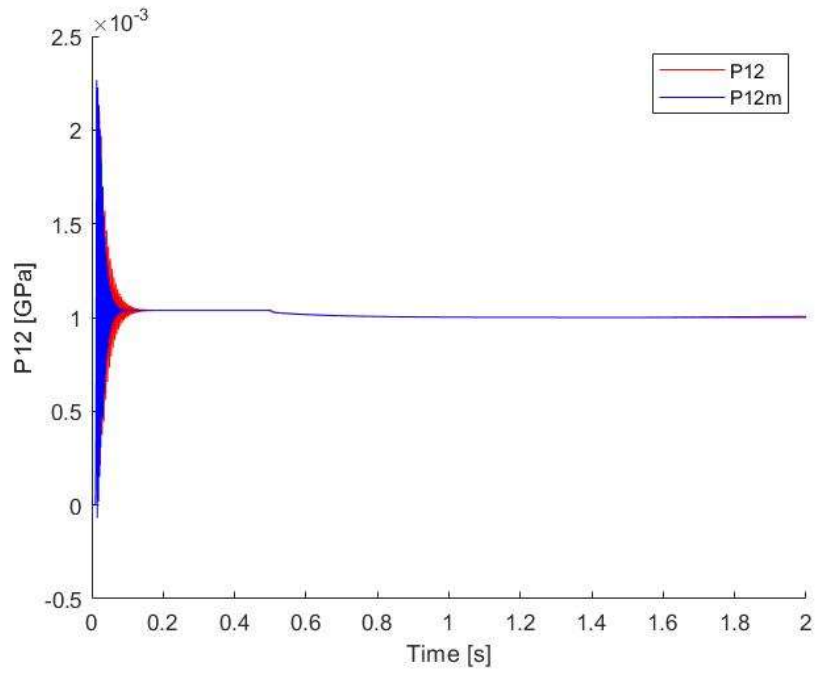


Figure 7.13: HF and LF P12 responses for $FDJ=800\text{ N}$

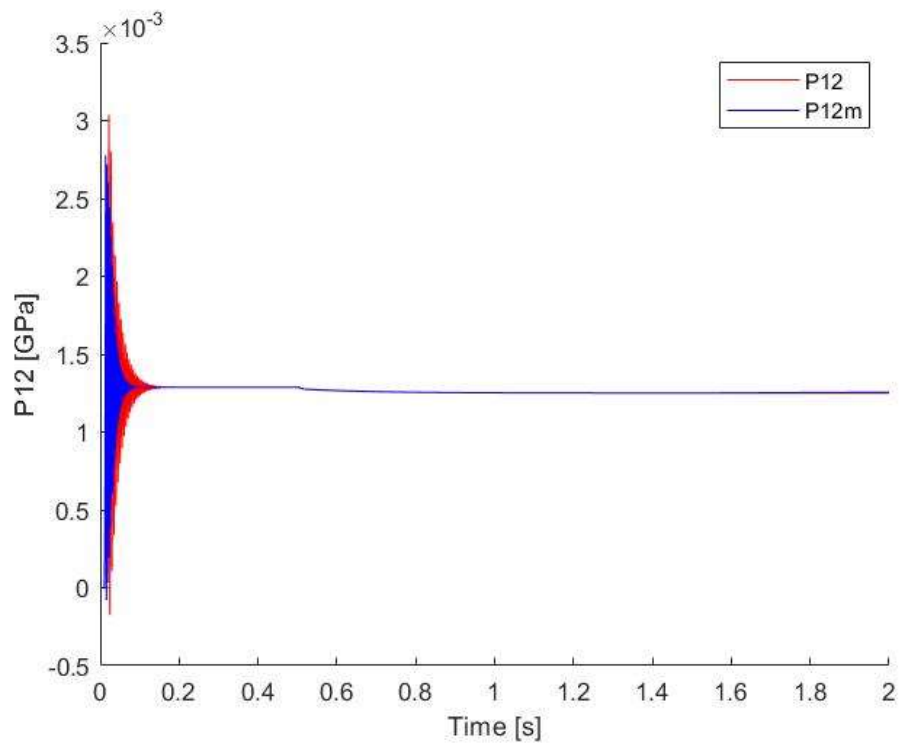


Figure 7.14: HF and LF P12 responses for $FDJ=1000\text{ N}$

As it can be seen by the figures above, there is a good correspondence between the two responses for all the values of static friction, making the quantity $PI2$ a good characteristic for the identification of the friction increase. In this way, the objective function can be defined as the absolute value of the difference between the mean value of the High-Fidelity pressure, evaluated in the neighbourhood of 1.1 seconds after the new input thanks to the great correspondence between the two models, and the mean value of the pressure in the Low-Fidelity model evaluated in the same time interval. In Figure 7.15, code of the function used by the genetic algorithm is shown, where the variable *fitness* corresponds to the objective function.

```
function [fitness]=simulate(vars)
    global FDJm Pressione
    FDJm=vars
    sim LF.slx
    Pressionem=movmean(PI2m.data(5.1e5), [1000 1000]);
    fitness=abs(Pressionem-Pressione)
end
```

Figure 7.15: Code of the objective function.

Below the results of this second preliminary analysis are reported.

FDJ	FDJm	Err % KGM
200	200,0129	0,00645
400	400,0169	0,004225
600	600,019	0,0031667
800	800,0244	0,00305
1000	1000	0

The results approximate very well the values of FDJ , with a percentual error lower than 0.006% in all cases.

Finally, after the validation of the algorithm for each fault, a complete procedure for the estimation of both faults simultaneously has been implemented. The new objective function will be the union of the objective functions used previously: it will be, in fact, the sum of the two different parameters that identify the faults.

A minimal modification has been applied to the first part of the objective function, about the monitoring of the current absorbed by the torque motor: Low-Fidelity model, in fact, can not perfectly remark the behaviour of the High-Fidelity model.

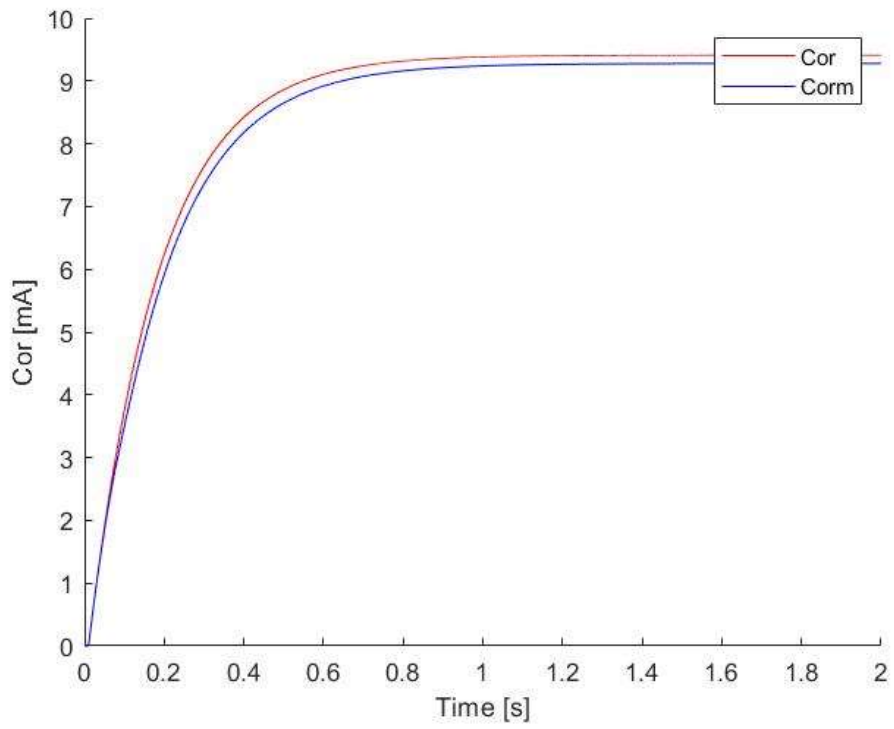


Figure 7.16: Cor and Corm ramp responses with FDJ=200 N.

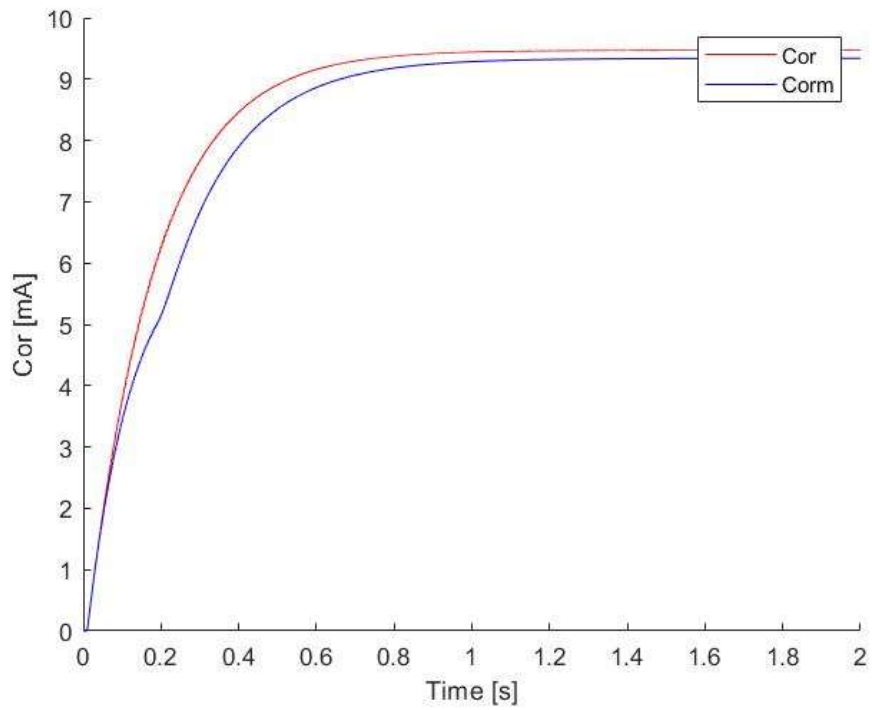


Figure 7.17: Cor and Corm ramp responses with FDJ=400 N.

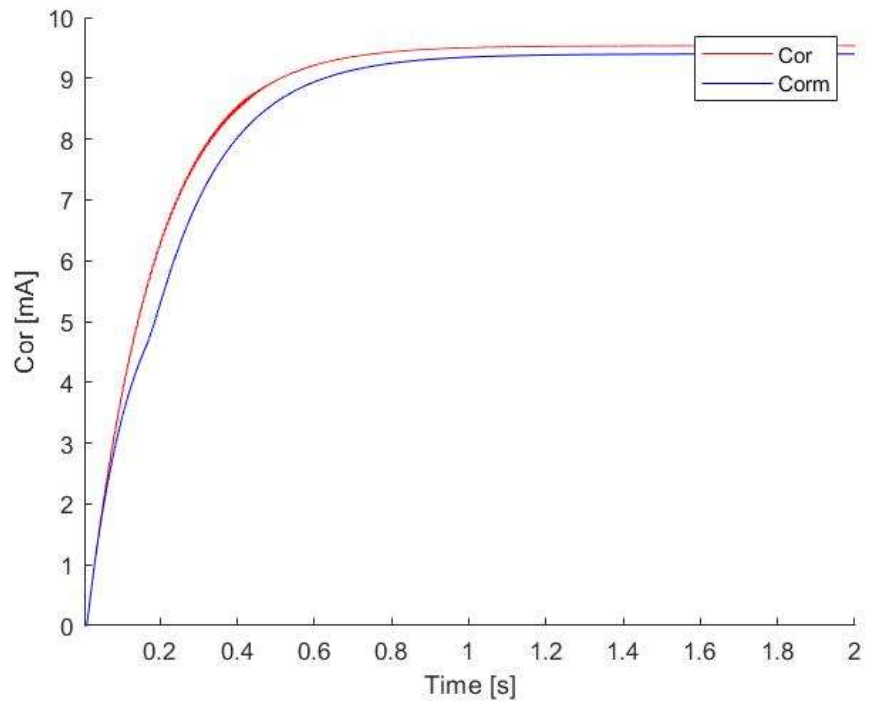


Figure 7.18: Cor and Corm ramp responses with FDJ=600 N.

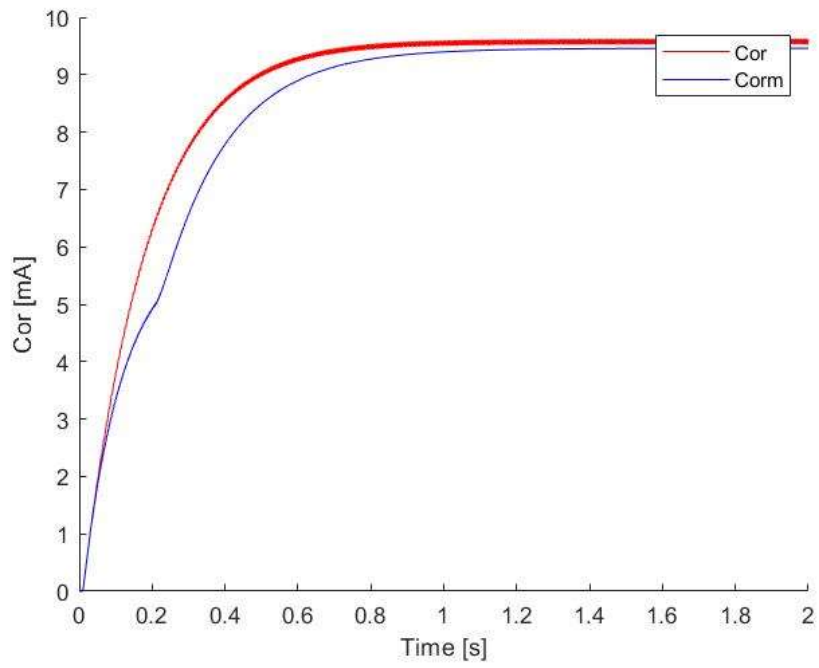


Figure 7.19: Cor and Corm ramp responses with FDJ=800 N.

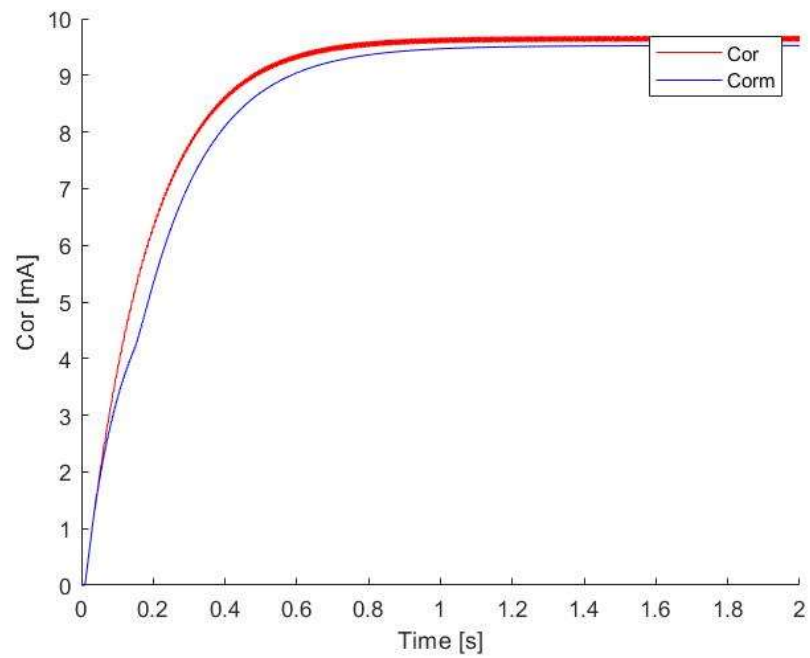


Figure 7.20: Cor and Corm ramp responses with FDJ=1000 N.

Since the steady state value of the current has been chosen as diagnostic parameter, transient has been ignored. About the steady state value, as it can be seen from the figures above, the current of the High-Fidelity presents an oscillation for $FDJ > 600 N$ during the entire simulation period. For this reason, the objective has been modified in a way this oscillation can not influence the individuation of the steady state, so adding the mean of the values in the last 0.01 seconds.

In conclusion, the new objective function has been chosen as the absolute value of the difference between the steady state of the currents Cor summed to the absolute value of the difference between the pressures $P12$. To have an objective function that gives the same weight to both faults, the singular objective functions have been modulated to the same order of magnitude. The final objective function is shown below.

```
function [fitness]=simulate(vars)
    global FDJm Pressione KGMm Corrente
    KGMm=vars(1)
    FDJm=vars(2)
    sim LF.slx
    Pressionem=movmean(P12m.data(5.1e5),[1000 1000]);
    Correntem=movmean(Corm.data(190001),[10000 0]);
    fitness=abs(Pressione-Pressionem)/1e4+abs(Corrente-Correntem-0.15)*10;
end
```

Figure 7.16: Code of the final objective function.

It is interesting, also, to take a look at the settings of the algorithm.

```
options = optimoptions('ga', 'PopulationSize',40,'PlotFcns',...
    {@gaplotbestf,@gaplotbestindiv,@gaplotgenealogy,@gaplotstopping},...
    'Generations',10,'PlotInterval',1,'MutationFcn',...
    {@mutationadaptfeasible},'FitnessScalingFcn',@fitscalingprop,...
    'HybridFcn',{@fmincon []});

[X,fitness]=ga(f, nvar, [], [], [], [], lb,ub, [], options)
```

Figure 7.17: Genetic algorithm options.

The algorithm outputs are the optimized variables and the relative value of the fitness function, while it receives several inputs:

- f represents the function that the algorithm calls at every simulation and it calculates the fitness function of the individual of every generation;

- *nvar* is the number of variables that have to be optimized, in this case equal to 2;
- *lb* represents the lower bound of the optimization variables, in this case a vector where the first value is 0 (nominal condition of the torque motor) and the second one is equal to 200 [N] (nominal condition of the static friction on the jack);
- *ub* represents the upper bound of the optimization variables, in this case a vector where the first value is 1 (complete demagnetization of the torque motor) and the second one is equal to 2000 [N] (maximum value of the static friction on the jack);
- *options* contains all the detailed settings of the algorithm, in particular a population of 40 has been chosen, to have a large number of combinations that can spaces in a great part of the domain, while a number of 10 generations is sufficient to let the algorithm converge. *Mutationadaptfeasible* and *fitscalingprop* are respectively the options for the mutation of the individuals and the method the method to choose the parents of the next generation. The final option is *fmincon*: thanks to this option of the hybrid functions, once the genetic algorithm finishes its task, another optimizer is run to refine the results.

This procedure has been applied to a wide range of combinations of faults, in order to test the robustness and the reliability of the algorithm. Even if ranges of the variables have been considered in their totality, realistic values have been chosen for the fault variables, in particular *KGM* has been simulated from 0 to 0.4, while the friction from 200 N to 1000 N. The obtained results are shown below.

Case	KGM	FDJ [N]	KGMm	FDJm [N]	Err_%_KGM	Err_%_FDJ
1	0	200	0	200.0017	-	0.00085
2	0	400	0,0002	403.2076	-	0.8019
3	0	600	0	600.0125	-	0.0020833
4	0	800	0	800.0113	-	0.0014125
5	0	1000	0	1000	-	0
6	0.1	200	0.0997	200.0076	0.3	0.0038
7	0.1	400	0.1024	399.9534	2.4	0.01165
8	0.1	600	0.1023	599.9788	2.3	0.0035333
9	0.1	800	0.0953	800.0377	4.7	0.0047125
10	0.1	1000	0.1	1000	0	0
11	0.2	200	0.2011	200.0030	0.55	0.0015
12	0.2	400	0.2037	400.1682	1.85	0.04205
13	0.2	600	0.2019	599.9800	0.95	0.0033333
14	0.2	800	0.2016	800.0123	0.8	0.0015375
15	0.2	1000	0.2	1000	0	0
16	0.3	200	0.3022	199.9796	0.73	0.01202
17	0.3	400	0.3026	394.0467	0.87	1.488325
18	0.3	600	0.3025	600.1320	0.83	0.022
19	0.3	800	0.3036	799.9437	1.2	0.0070375
20	0.3	1000	0.3	1000.1	0	0.01

21	0.4	200	0.4027	201.0354	0.675	0.5177
22	0.4	400	0.3998	400.9092	0.05	0.2273
23	0.4	600	0.4041	610.4446	1.025	1.7407667
24	0.4	800	0.4031	799.9047	0.775	0.0119125
25	0.4	1000	0.4021	999.9511	0.525	0.00489

The percentage errors have been calculated as follow:

$$err_ \% = \frac{|value\ to\ be\ found - value\ found|}{value\ to\ be\ found} * 100$$

Looking at the table reported above, it can be observed that the results of the genetic algorithm are mostly acceptable: in particular, it provides better results for the static friction *FDJ*, where the error maximum value is equal to 1.74% for the case 23; also in case 19 the error results equal to 1.49%, while in the other cases the values found are always under 1%, with case 5, 10 and 16 that have error equal to 0 (this can be explained as an approximation in the display of the results). For the demagnetization of the torque motor *KGM*, instead, the maximum value is higher than the previous one and equal to 4.7%, but acceptable; cases 7, 8, 12, 19 and 23 shows an error equal respectively to 2.4%, 2.3%, 1.85%, 1.2% and 1.025%, while the remaining are always under 1%. The greater errors on *KGM* respect to *FDJ* could be explained by referring to the values to be found: they are coefficients included between 0 and 1, so a an imprecision on the second or third significant digit can lead to a non-negligible error.

To test the robustness of the genetic algorithm, two more conditions have been simulated. In the first case, a disturbance has been added to the current absorbed by the torque motor; in particular, a band-limited white noise with a power of $5 * 10^{-6}$ W has been added before the output of the sub-block *Offset Current*. Below the results of this condition are reported.

Case	KGM	FDJ [N]	KGMm	FDJm [N]	Err % KGM	Err % FDJ
1	0	200	0,00553	202,2831	-	1,14155
2	0	400	0,0071	408,8124	-	2,2031
3	0	600	0,0055	603,2838	-	0,5473
4	0	800	0,0029	802,2355	-	0,2794375
5	0	1000	0	1002,2	-	0,22
6	0.1	200	0,1051	201,3833	5,1	0,69165
7	0.1	400	0,1039	401,4297	3,9	0,357425
8	0.1	600	0,1047	600,8366	4,7	0,1394333
9	0.1	800	0,1051	801,3042	5,1	0,163025
10	0.1	1000	0,1	1001,3	0	0,13
11	0.2	200	0,205	200,6825	2,5	0,34125
12	0.2	400	0,2046	384,0253	2,3	3,993675
13	0.2	600	0,2062	600,7393	3,1	0,1232167
14	0.2	800	0,2081	800,6676	4,05	0,08345
15	0.2	1000	0,2	1000,7	0	0,07

16	0.3	200	0,305	200,5101	1,66666667	0,25505
17	0.3	400	0,3045	397,5125	1,5	0,621875
18	0.3	600	0,3053	600,5438	1,76666667	0,0906333
19	0.3	800	0,3083	800,4509	2,76666667	0,0563625
20	0.3	1000	0,3	1000,6	0	0,06
21	0.4	200	0,4036	198,8702	0,9	0,5649
22	0.4	400	0,3934	411,5263	1,65	2,881575
23	0.4	600	0,4061	600,7341	1,525	0,12235
24	0.4	800	0,4061	800,6385	1,525	0,0798125
25	0.4	1000	0,4	1000,8	0	0,08

Respect to the previous case where no noise was simulated, the current disturbance influences the results, especially the error in the evaluation of *KGMm*: in these simulations, in fact, from 4.7% to 5.1%, but in general all cases show an increment of about 2-3%. About the error in the evaluation of *FDJm*, no visible variations are present, except for case 12 that shows an error of 3.99% (this can be an outlier of the genetic algorithm).

In the second case, a clearance of 30 micron has been introduced in the sleeve of the valve, in this way the flow rate losses because of the leakage are increased. The results obtained from the genetic algorithm are shown below.

Case	KGM	FDJ [N]	KGMm	FDJm [N]	Err % KGM	Err % FDJ
1	0	200	0	200,062	-	0,031
2	0	400	0	396,5122	-	0,87195
3	0	600	0,0004	620,3062	-	3,3843667
4	0	800	0	800,0702	-	0,008775
5	0	1000	0	1000,1	-	0,01
6	0.1	200	0,0994	200,0601	0,6	0,03005
7	0.1	400	0,0964	396,0623	3,6	0,984425
8	0.1	600	0,1023	600,0622	2,3	0,0103667
9	0.1	800	0,096	800,0864	4	0,0108
10	0.1	1000	0,1	1000,1	0	0,01
11	0.2	200	0,2009	200,0432	0,45	0,0216
12	0.2	400	0,1982	398,4136	0,9	0,3966
13	0.2	600	0,1997	598,5198	0,15	0,2467
14	0.2	800	0,2028	800,0416	1,4	0,0052
15	0.2	1000	0,2006	999,9904	0,3	0,00096
16	0.3	200	0,302	200,0102	0,66666667	0,0051
17	0.3	400	0,2944	402,829	1,86666667	0,70725
18	0.3	600	0,3141	602,921	4,7	0,4868333
19	0.3	800	0,3038	799,7181	1,26666667	0,0352375
20	0.3	1000	0,3	1000	0	0
21	0.4	200	0,4002	197,6048	0,05	1,1976

22	0.4	400	0,4037	404,3952	0,925	1,0988
23	0.4	600	0,4021	600,9824	0,525	0,1637333
24	0.4	800	0,4013	800,0246	0,325	0,003075
25	0.4	1000	0,4027	1000,1	0,675	0,01

In these simulations, a decrease in the error in the evaluation of KGM can be noticed: this is because of the clearance that influences the current absorbed by the torque motor, decreasing the difference between High-Fidelity and Low-Fidelity currents (it must be considered that the clearance is not present in the Low-Fidelity model and the value of 0,15 mA subtracted in the objective function is the minimal difference between them). About the evaluation of FDJ , an increasing error is present respect to the previous cases, as expected.

8 CONCLUSIONS AND FUTURE WORKS

The principal aim of this thesis was to model, in a satisfying way, the fluid-dynamic part of the flapper-nozzle valve.

The resultant model accomplishes very well this task, but its functioning range is limited at high values of the flow rate. This can be due to its mathematical formulation that can be calibrated on lower or higher values of the flow rate, but not on both; also, the approximation of time constants, that is not so precise for lower values, can influence this behaviour.

It could be interesting to start from the approach used in this thesis, reproducing the response of the High-Fidelity model for every input, with a different mathematical formulation.

To solve this problem in a different way, look-at-tables that reproduce in a more precise way the characteristic curves of flow rate and pressure and the time constant map could be implemented. Using a totally different approach, this task could be also carried out by a neural network, even if more demanding from a computational point of view.

The successive step has been the development of the optimization algorithm for diagnostic and prognostic purpose. Firstly, it was necessary to study how the analysed faults, the demagnetization of the torque motor and the increasing static friction on the jack, influence the behaviour of the system. Two different quantities have been identified for the faults: the steady state value of the current response to a ramp and the steady state value of the differential pressure response to a step. It can be observed as these two quantities identify very well the presence of each fault; since one fault does not influence the parameter of the other, they are very useful in the formulation of the objective function of the genetic algorithm. The results obtained in this way are more precise for the static friction *FDJ* than for the demagnetization *KGM*, under 2% for the first, but anyway under 5% for the second, making the algorithm adapt for this analysis.

It could be interesting studying the effects of other faults, in particular the ones present in the servovalve, and try to expand this procedure. Moreover, the genetic algorithm results can be refined more, trying to combine aspects of other algorithms, such the best aspects of the first compensate the bad ones of the second; for example, a deterministic algorithm, that can converge to a local minimum, can provide a good initial population for the genetic algorithm that can converge to the total minimum. Alternatively, it could be possible to use another optimization algorithm as *Particle Swarm Optimization*, *Grey Wolf Optimization* or *Dragonfly Algorithm*.

In conclusion, the results of this thesis meet the initial purposes and it represents a possible way to detect and predict the state of fault in the electro-hydraulic actuator, even from their initial appearance.

REFERENCES

- Borello, L., Dalla Vedova, M. D. L., Jacazio, G., & Sorli, M. (2009). A prognostic model for electrohydraulic servovalves. In *Annual Conference of the Prognostics and Health Management Society* (pp. 1-12).
- Borghetto, M. (2016). Study of Optimization algorithms for the prognostic of electro-hydraulic servomechanisms for aeronautical applications. *Tesi di Laurea Magistrale*
- Dalla Vedova, M. D. L., Maggiore, P., & Pace, L. (2014). Proposal of prognostic parametric method applied to an electrohydraulic servomechanism affected by multiple failures. *WSEAS Transactions on Environment and Development*, 10, 478-490.
- Dalla Vedova, M., D., L. (2007). Modelli Numerici Semplificati delle Caratteristiche Fluidodinamiche di Servovalvola. *Tesi di dottorato, Cap. 5*.
- Dalla Vedova, M., D., L. (2007). Modellizzazione di Servomeccanismi Elettroidraulici. *Tesi di dottorato, Cap.*
- Dalla Vedova, M., D., L. (2007). Modello Numerico Particolareggiato delle Caratteristiche Fluidodinamiche di Valvola. *Tesi di dottorato, Cap. 4*.
- Dalla Vedova, M., D., L., & Maggiore, P. (2020). Advanced numerical modeling for systems engineering: theory and applications. *Politecnico di Torino, Scuola di Dottorato*.
- Dalla Vedova, M., Jacazio, G., Maggiore, P., & Sorli, M. (2010). Identification of precursors of servovalves failures for implementation of an effective prognostics. In *Proceedings of the 4th International Conference on Recent Advances in Aerospace Actuation Systems and Components* (pp. 111-126).
- Fu, J., Maré, J. C., & Fu, Y. (2017). Modelling and simulation of flight control electromechanical actuators with special focus on model architecting, multidisciplinary effects and power flows. *Chinese Journal of Aeronautics*, 30(1), 47-65.
- Maggiore., P. (2020). Comandi di volo. ATA 27. *Politecnico di Torino, Corso di "Sistemi di bordo aerospaziali"*.
- Riva, D. (2019). Modellazione ed analisi di un servocomando SCAS per elicotteri modificato. *Politecnico di Torino, Tesi di laurea magistrale*.
- Romano, A. (2011) Modelli per la Prognostica delle Avarie Multiple di Comandi di volo Primari. *Tesi di Laurea Magistrale*.
- Singh, S., Chand, A., & Lal, S. P. (2013, September). Improving spam detection using neural networks trained by memetic algorithm. In *2013 Fifth International Conference on Computational Intelligence, Modelling and Simulation* (pp. 55-60). IEEE.
- Simi, A. (2007). Implementazione di algoritmi genetici multiobiettivo distribuiti in ambiente Matlab®.

Urata E., (2000) *Study of magnetic circuits for servovalve torque motors*. Bath workshop on power transmission and motion control, pp. 269-282.

Urata E., (2001) *Study on Leakage Flux from Servovalve Torque Motors*". The Seventh Scandinavian Intl. Conf. on Fluid Power, Vol.1, pp. 51-66, Linköping, Sweden.

Urata E., (2002) *Influence of fringing on servovalve torque-motor characteristic*, Proc. Fifth JFPS Intl. Symp. On Fluid Power, Vol.3, pp.769-774, Nara.

Urata E., (2003) *Static Stability of Torque Motors*, The Eighth Scandinavian Intl. Conf. on Fluid Power, Vol.2, pp.871-885, Tampere, Finland.

Urata E., (2004) *Influence of eddy current on torque-motor dynamics*, 4th IFK, Workshop March 24, pp. 71-82, Dresden, Germany.

Urata, E. (2004). One-degree-of-freedom Model for Torque-motor Dynamics. *International Journal of Fluid Power*, 5(2), 35-42. 7

Urata, E. (2007). Influence of unequal air-gap thickness in servo valve torque motors. *Proceedings of the Institution of Mechanical Engineers, Part C: Journal of Mechanical Engineering Science*, 221(11), 1287-1297.

FIGURES INDEX

Figure 2.1: Primary and secondary fight commands.	8
Figure 2.2: Hydro-mechanical actuator scheme.	9
Figure 2.3: Electro-mechanical actuator control scheme.....	10
Figure 2.4: Electro-hydrostatic actuator control scheme.	11
Figure 3.1: Section of a flapper-nozzle valve.	13
Figure 3.2: Scheme of the torque motor and the first stage of the flapper-nozzle valve.	14
Figure 3.3: Scheme of the first and second stage of the flapper-nozzle valve.....	15
Figure 3.4: Characteristic curves of a valve, pressure-displacement (a), flow rate- displacement (b).....	16
Figure 3.5: Flow rate and pressure gains definition.....	17
Figure 3.6: Different lapp conditions in a valve.	18
Figure 3.7: Schemes of the response of the three lapp conditions.	18
Figure 3.8: Graphical interpretation of threshold.....	19
Figure 3.9: Typical hysteresis scheme of electric motors.....	20
Figure 3.10: Friction force behaviour.	22
Figure 3.11: Graphical description of the Coulomb friction model.....	23
Figure 3.12: Graphical representation of the Karnopp model.	24
Figure 3.13: Simulink Karnopp model.	24
Figure 3.14: Graphical representation of Borello friction model.....	25
Figure 3.15: Simulink of Borello friction model.	26
Figure 4.1: Simulink representation of the High-Fidelity model.....	29
Figure 4.2: Sub-system of the input block.	30
Figure 4.3: Scheme of the PID controller.	30
Figure 4.4: Different types of offset current model.	32
Figure 4.5: Third order electromechanical model of the servovalve.	33
Figure 4.6: Calculation of the gain GM.	33
Figure 4.7: Magnet circuit of the torque motor.....	34
Figure 4.8: Second order dynamical model of the first stage of the servovalve.....	36
Figure 4.9: First order dynamic model of the second stage of the servovalve.....	37
Figure 4.10: 4/3-way directional control valve scheme.....	39
Figure 4.11: Section of passing section of the fluid when $XS > 0$ for zero-lapping valve.	41
Figure 4.12: Simulink model of the subsystem “Fluid dynamic model”.....	43
Figure 4.13: Scheme of the subsystem CRH, relative to the passing area S_2	44
Figure 4.14: Pipe capacity model.....	46
Figure 4.15: Complete fluid dynamic model.	46
Figure 4.16: Characteristic curves P12-XS.....	47
Figure 4.17: Characteristic curves QJ-XS.	47
Figure 4.18: Model of the jack.....	48
Figure 4.19: Low-Fidelity model.....	49
Figure 4.20: Electromechanical model of the servovalve.....	49
Figure 5.1: Simulink linearized fluid-dynamic model.....	53

Figure 5.2: Characteristic curves P12-XS of the first linearized model.	53
Figure 5.3: Leakage loop representation.....	55
Figure 5.4: Simulink evolved fluid-dynamic model.	56
Figure 5.5: Characteristic curves P12-XS of the evolved fluid-dynamic model.	57
Figure 5.6: Control scheme relative to P12 dissipation.	59
Figure 5.7: Simulink model of the new fluid-dynamic model (first version).	60
Figure 5.8: Comparison of the High-Fidelity and Low-Fidelity models characteristic curves P12-XS.	60
Figure 5.9 Comparison of the High-Fidelity and Low-Fidelity models characteristic curves QJ-XS.	61
Figure 5.10: Time constants map of the HF model.	62
Figure 5.11: Approximation of the bell-shaped behaviour of time constants at QJ=0.	63
Figure 5.12: Approximation of tau from the High-Fidelity model.	64
Figure 5.13: New developed fluid-dynamic model.	64
Figure 5.14: Time response of HF and LF models for step with amplitude of 0.1 m.	65
Figure 5.15: Time response of HF and LF models for ramp with slope of 0.1 m/s.	65
Figure 5.16: Time response of HF and LF models for sine with semi amplitude of 0.1 m.	66
Figure 6.1: Cor response to a step input signal.....	69
Figure 6.2: DXJ response to a step input signal.....	69
Figure 6.3: P12 response to a step input signal.....	70
Figure 6.4: XJ response to a step input signal.	70
Figure 6.5: XS response to a step input signal.....	71
Figure 6.6: Cor response to a ramp input signal.	82
Figure 6.7: detail of DXJ response to a ramp input signal.....	83
Figure 6.8: detail of P12 response to a ramp input signal.....	83
Figure 6.9: XJ response to a ramp input signal.....	84
Figure 6.10: XS response to a ramp input signal.	84
Figure 6.11: Cor response to a sine input signal.....	85
Figure 6.12: DXJ response to a sine input signal.....	86
Figure 6.13: P12 response to a sine input signal.....	86
Figure 6.14: XJ response to a sine input signal.	87
Figure 6.15:XS response to a sine input signal.....	87
Figure 6.16: Input signal used.....	89
Figure 7.1: Basic scheme of a genetic algorithm.	93
Figure 7.2: Proportional selection scheme.....	95
Figure 7.3: Crossover in genetics and binary single point crossover.....	95
Figure 7.4: HF and LF Cor responses for KGM=0.....	98
Figure 7.5: HF and LF Cor responses for KGM=0.1.....	98
Figure 7.6: HF and LF Cor responses for KGM=0.2.....	99
Figure 7.7: HF and LF Cor responses for KGM=0.3.....	99
Figure 7.8: HF and LF Cor responses for KGM=0.4.....	100
Figure 7.9: Code of the objective function.	100
Figure 7.10: HF and LF P12 responses for FDJ=200 N.....	101
Figure 7.11: HF and LF P12 responses for FDJ=400 N.....	102
Figure 7.12: HF and LF P12 responses for FDJ=600 N.....	102

Figure 7.13: HF and LF P12 responses for FDJ=800 N	103
Figure 7.14: HF and LF P12 responses for FDJ=1000 N	103
Figure 7.15: Code of the objective function.	104
Figure 7.16: Code of the final objective function.	108
Figure 7.17: Genetic algorithm options.	108